SPring-8
Research Frontiers

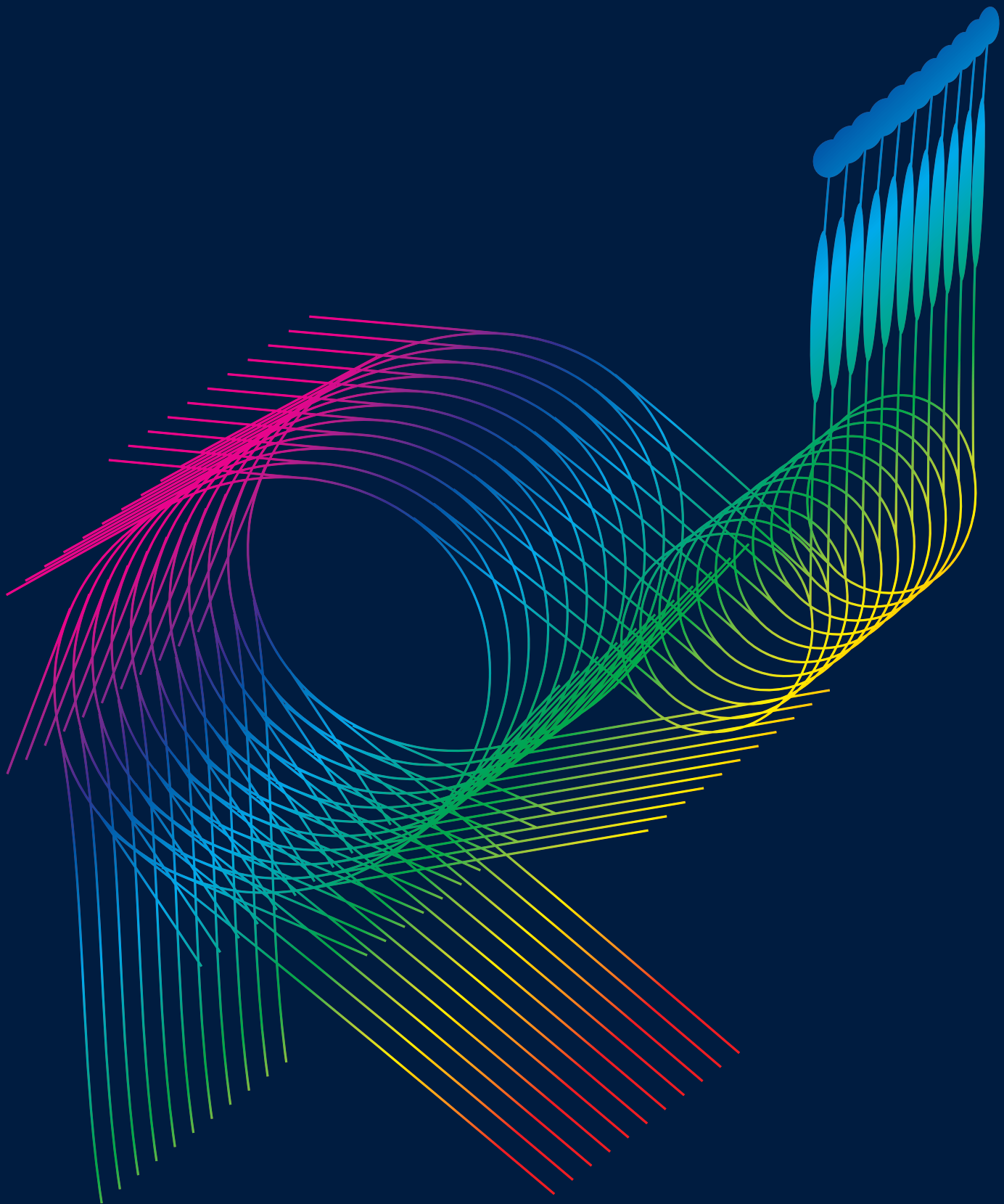

1999／2000

Contents

Preface

This volume is the third issue of the SPring-8 Research Frontiers and presents the results of the most impressive experiments carried out at the SPring-8 facility from September 1999 to June 2000. This corresponds to the users period of 1999B (from Sep. 29 to Dec. 24, 1999) and 2000A (from Jan. 19 to June 16, 2000). Beam time of 430 shifts (174 shifts in 1999B and 256 shifts in 2000A) were dedicated to more than 770 user experiments. These were performed by over 6000 users via 24 beamlines (17 public, 4 JAERI/RIKEN and 4 contract beamlines).

Reflecting the high performance of the storage ring and development of high performance instrumentation and experimental technology relating to the outstanding physical characteristics of synchrotron radiation, research activities at SPring-8 have increased both in their breadth and significance leading to a number of important findings.

The experiments covered in this report are classified by topic into six groups: Life Science, Diffraction and Scattering, XAFS, Spectroscopy, Instrumentation and Techniques, and Industrial Applications. A total of 753 experiments were pursued resulting from 1054 proposals. These experiments are separated by topic as follows with the number of proposals given in parenthesis: 150 (176) in Life Science, 216 (360) in Diffraction & Scattering, 86 (155) in XAFS, 61 (87) in Spectroscopy, 59 (77) in Instrumentation & Techniques, and 181 (199) in Industrial Applications. The above number does not include experiments pursued mainly by the in-house staff of SPring-8.

Six experiments in the field of Life Science are presented in this volume. An undulator beamline for the structural analysis of macro-molecular assemblies became operational during this period. Furthermore, data collection for MAD phasing is now a nearly routine procedure of all beamlines used in the study of structural biology. Many outstanding results have been obtained through use of these beamlines. In addition to structural analysis, time-resolved X-ray diffraction was studied at the small-angle X-ray scattering station of BL45XU. Additionally, a high-resolution X-ray CT (computer tomography) imaging technique has been developed with potential use in medical applications.

In this volume seven reports are selected from the Diffraction and Scattering group. In addition to the existing beamlines, two new beamlines, BL02B2 and BL04B2, became operational in 1999. It should be emphasized that four out of the seven studies in this group were performed using newly developed beamlines. Reflecting its high performance in hardware as well as the newly developed method of MEM/Rietveld analysis, many outstanding results were produced at BL02B2 in a very short time. Through use of beamline BL04B2 it is possible to obtain an accurate structure factor up to high scattering Q of 35 A^{-1}.

Five experiments are selected from the XAFS group. XAFS analysis has become the standard method of clarifying the relationship between the function and the atomic and/or electronic structure of materials in order to develop more useful materials. Development of the XAFS method continues using a number of specific features of SPring-8, such as high brilliance, polarization and microbeam, and pursuing in situ experiments under extreme conditions.

Spectroscopic studies at SPring-8 cover Compton scattering, magnetic X-ray scattering, magnetic circular dichroism, spectroscopy of atoms and molecules, photoemission spectroscopy of solids, and infrared spectroscopy. Although SPring-8 is the world's most advanced radiation source in the hard X-ray region, it also provides a highly brilliant and very stable soft X-ray beam, and is one of the most powerful tools available in photoemission spectroscopy. Three experiments from the Spectroscopy group are presented in this volume.

Three experiments are presented from the Instrumentation and Techniques group. The development of microbeam optics has been pursued preferentially at SPring-8 and submicron spatial resolutions have been realized by using various types of focusing lenses. A new type of sagittal focusing bender was developed for the standard monochromator of SPring-8 bending magnet beamline.

A new section entitled "Industrial Applications" is added in this issue of SPring-8 Research Frontiers. Industrial application of synchrotron radiation is one of the major aims of the SPring-8 project and the coordinator system has recently been introduced in JASRI to promote the industrial applications in SPring-8. It should be noted that 24% of all the experiments in 1999B and 2000A periods were performed in conjunction with industry.

In 2000, a 27 m-long undulator was installed in the storage ring and the world's most brilliant X-ray was successfully extracted. As the initial ring had no long straight sections for the long undulators, it was converted to the new ring with long magnet-free spaces before installing the long undulator. During the summer shut down time in 2000, the initial lattice structure (phase-I optics) of the storage ring was changed to the new lattice structure (Phase-II optics) that has four long magnet-free straight sections by rearranging the focusing magnets. Remodeling of the lattice structure and beam commissioning was successfully completed in the middle of September. The beam performance achieved by the Phase-II optics is almost nearly identical to that of the phase-I optics. Works performed toward the improvement of the accelerator performance and development of insertion devices and detectors are also presented in this issue along with the status reports of the facility in 2000.

H. Kamitsubo

Hiromichi Kamitsubo
Director
SPring-8 / JASRI

SPring-8 Research Frontiers describes the remarkable scientific achievements made at all beamlines (BL's) at SPring-8: public BL's including R & D BL's, contract BL's, JAERI/RIKEN BL's and an accelerator diagnosis beamline. Developments in the accelerators and beamlines themselves are also reported. This third volume "1999/2000" covers advances made during the research period spanning from the second half of 1999 to the first half of 2000.

To properly classify all the synchrotron radiation research fields within this volume, we have added a new field, "Industrial Applications" to the former five categories. Highlights in this field were selected from the viewpoint of impacts on industrial development.

We have invited six specialists from the Proposal Review Committee to be the Editing Coordinators for their respective research fields:

Life Science: *Professor Isao Tanaka* (Hokkaido University)
Diffraction & Scattering: *Professor Makoto Sakata* (Nagoya University)
XAFS: *Professor Masaharu Nomura* (High Energy Accelerator Research Organization)
Spectroscopy: *Professor Atsushi Fujimori* (The University of Tokyo)
Instrumentation & Techniques: *Professor Tsuneaki Miyahara* (Tokyo Metropolitan University)
Industrial Applications: *Professor Junji Matsui* (Himeji Institute of Technology)

We would like to express our most sincere appreciation to these Editing Coordinators for their efforts in preparing the introductory overviews and providing comments on each research field. We would also like to express our gratitude to the users and facility members of SPring-8 for contributing their reports.

The **SPring-8 Research Frontiers** publication will be sent on request. Its full text is also available by accessing SPring-8's Web site (http://www.spring8.or.jp/).

Scientific Frontiers

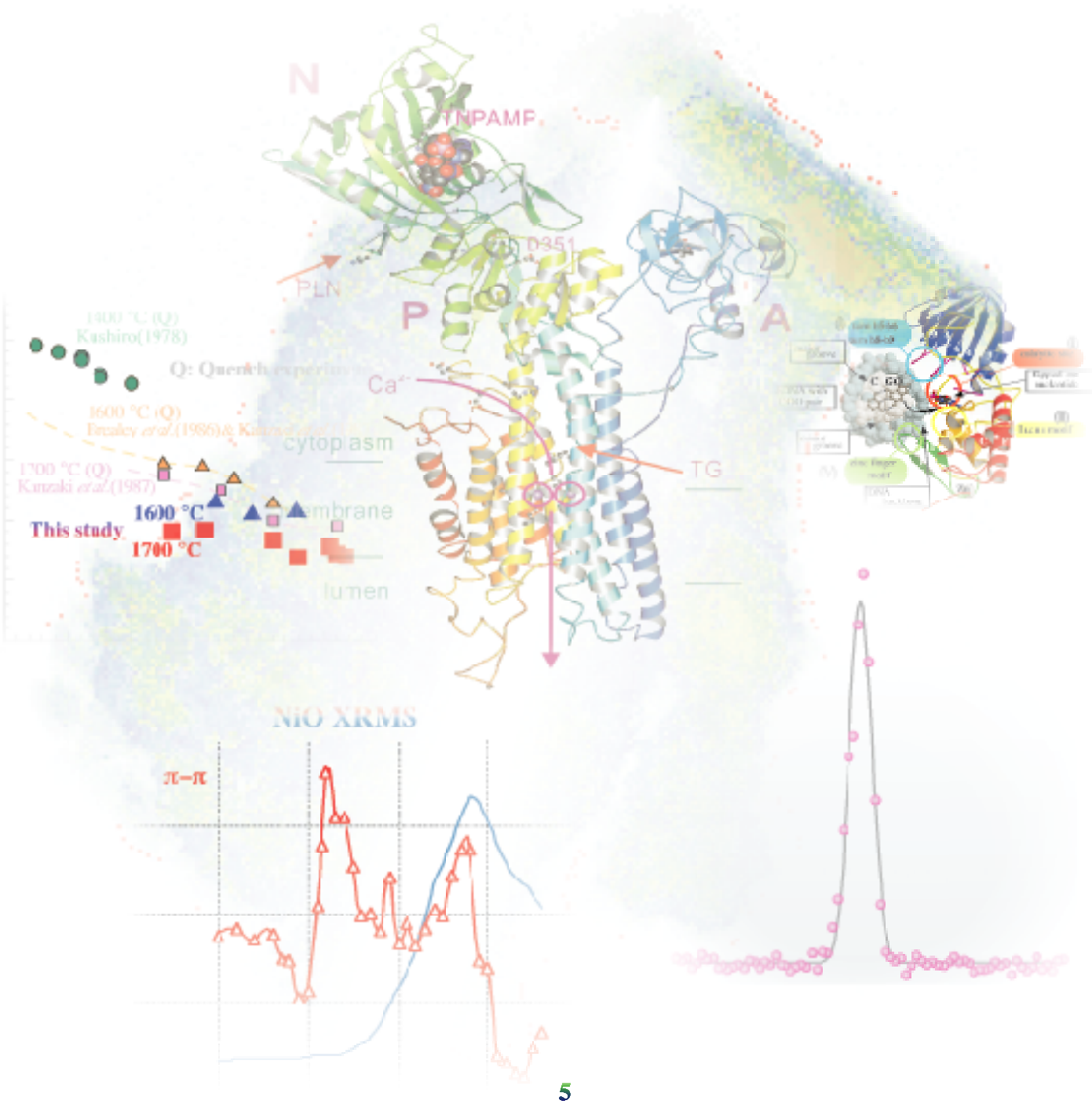

LIFE SCIENCE

An undulator beamline, BL44XU, designed for the structural analysis of biological macromolecular assemblies, is now operational. This beamline allows for the collection of data from crystals with unit cells as large as 1500 Å. Other beamlines in the Life Science field have been improved in many ways and particularly user-friendly; data collection for MAD phasing is now becoming a routine. Six of the many outstanding finding resulted by using these beamlines are herein presented.

The atomic model of rhodopsin, one of the G-protein coupled receptors (GPCR), was determined using synchrotron radiation at SPring-8. GPCR protein genes are present at a count of more than 1000 in the human genome. The structural analysis of rhodopsin will provide a molecular basis for understanding the recognition of the target molecules by GPCR. The extracellular ligand-binding region of the metabotropic glutamate receptor (mGluR1), a key membrane receptor involved in the modulation of excitatory synaptic transmission in the central nervous system, was analyzed by the MAD method using beamlines BL45XU and BL24XU. The structure of the MutM protein, one of the DNA repair enzymes, was determined at 1.9 Å resolution by MAD phasing of the intrinsic Zn^{2+} ion at beamline BL45XU. The structure of Ca^{2+}-ATPase of the sarcoplasmic reticulum was determined at 2.6 Å resolution. Very thin crystals, typically less than 20 μm, were used for the structural analysis. The collection of data from such thin crystals was made possible by utilizing the brilliant X-rays at beamlines BL44B2 and BL41XU. Time-resolved X-ray diffraction studies of the purple membrane have been carried out at the SAXS station of BL45XU, allowing to study the structural transition from the M intermediate to the N intermediate of bacteriorhodopsin. An X-ray tomographic technique was used to study the morphology of human lung at high resolution. The synchrotron radiation computed tomography experiments were conducted at BL20B2 using a phosphor X-ray detector and a cooled CCD camera.

Isao Tanaka

ATOMIC STRUCTURE OF BOVINE RHODOPSIN: A SEVEN TRANSMEMBRANE RECEPTOR

Seven transmembrane (7TM) receptor is a major protein family. The interest in 7TM receptor is growing not only due to its biological significance but also because of its practical importance in the post-genomic era. It could be a potential target for developing therapeutics for diverse ailments, such as general pain, allergy, circulation disorder, CNS (central neural system) disorder and AIDS. In vertebrates, the 7TM receptor family is believed to contain at least 600 members, wherein 370 odorant receptors have been identified in the human genome. 7TM receptors bind a variety of ligand classes: retinals, bio-organic amines, odorants, amino acids and their derivatives, peptides, proteins, nucleic acids and their derivatives, lipids and their derivatives, and glycoproteins. Many of these 7TM receptors are primary cellular acceptors of environmental stimuli for many processes, such as vision, odorant sensing, neuro-transmission, hormone regulations and chemotaxis.

In cellular signal transduction, the molecular mechanism of the 7TM receptor is commonly triggered via the activation of a limited number of GTP-biding proteins. For this reason, the 7TM receptor is often called as G-protein coupled receptor (GPCR). The molecular structure of the 7TM receptor is similar in its seven transmembrane helix bundle; furthermore its dominant sub-family, rhodopsin family members, shares highly conserved residues in amino-acid sequences. Thus, most of the 7TM receptors are thought to be activated via a common mechanism. To elucidate the molecular mechanism of the 7TM receptor, the experimental atomic model of a visual pigment, rhodopsin in the retina, recently has been determined using synchrotron X-ray crystallography at beamline **BL45XU** by the MAD method, while low-resolution models had been previously obtained using electron diffraction methods for frog or bovine rhodopsin [Schertler *et al.*].

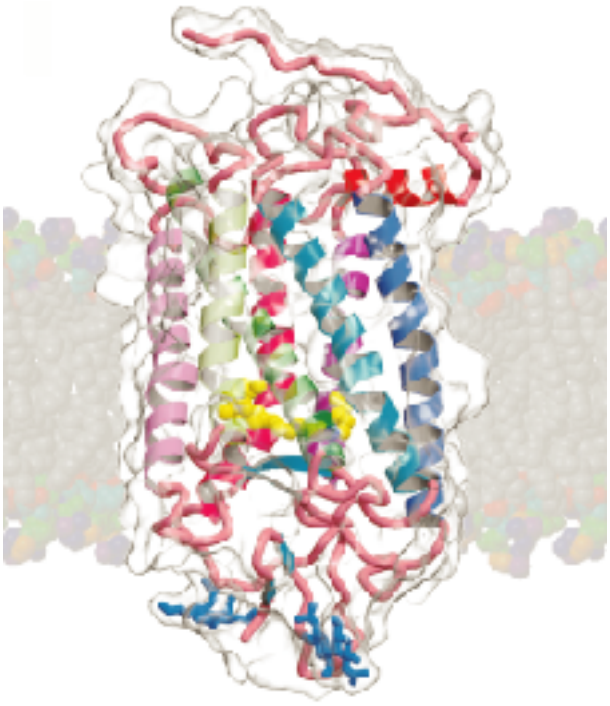

Fig. 1. Structure of bovine rhodopsin. Cartoon model of bovine rhodopsin structure with transparent molecular surface accompanied with putative lipid bi-layer model. Seven trans-membrane helices are colored in rainbow from α-helix I to VII with additional short helix VIII in red. Bound 11-cis-retinal shows ball model in yellow. Four short β-strands of N-terminal domain are in sky-blue. All loops are in pink wire with blue colored sugars.

The first structure of the 7TM receptor determined for bovine rhodopsin which preserved 11-*cis*-retinal, a vitamin A derivative, revealed several interesting features with the common 7TM bundle in an inactive state (Figs. 1 and 2) [1]. Additional amphiphilic short helix VIII is located directly adjacent to the 7th TM helix on the putative membrane surface (Fig. 3). The helices VII and VIII nearly form a right angle, supported by the aromatic ring stacking of the conservative Tyr^{306} and Phe^{313} (Fig. 4D) [2]. The N-terminal domain folds compactly in a two-layered structure (Fig. 3). The two layers are composed of an N-terminal region and the long loop between helices IV and V with an S-S bridge of the conserved Cys^{187} and Cys^{110} at the end of helix III (Fig. 4A).

Fig. 3. Stereo view of rhodopsin cartoon model.

Conversely, cytoplasmic loops almost open to form the putative interface with the G-protein, transducin [3]. Most of the highly conserved amino-acid residues among rhodopsin family members form non-covalent bonds to support the inactive form. The GPCR motif of Glu^{134}-Arg^{135}-Tyr^{136} interacts with Glu^{247} and Thr^{251} of helix VI at the cytoplasmic end of helix III (Fig. 4B). Asn^{55}, Asp^{83}, Asn^{78} and Trp^{161} are shown to constitute hydrogen-bond networks (Fig. 4C) [4]. Many parts of the seven transmembrane helices are irregular, due to many existing α-helix-destructive Gly and Pro residues

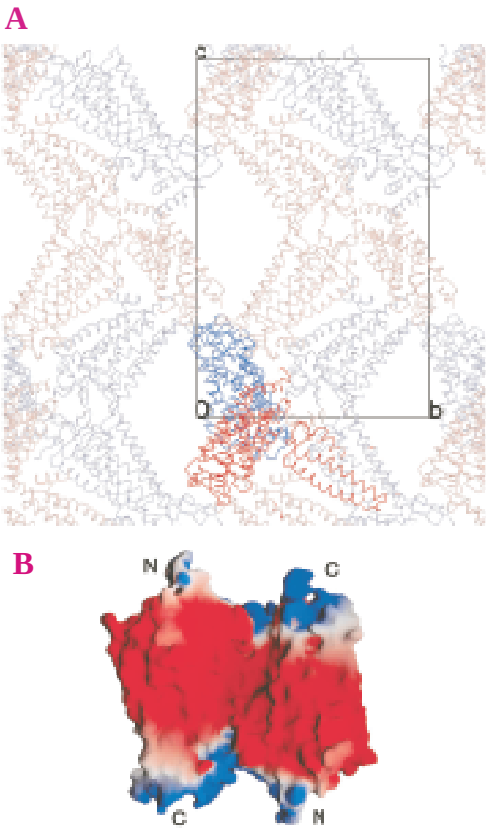

*Fig. 2. Crystal packing of bovine rhodopsin. **A)** Projection image of crystal packing onto **b**-**c** plane. Unit cell is indicated by square with the origin (**0**) and lattice (**b** and **c**). **B)** Dimer in a crystallographic asymmetric unit with water accessible surface colored by electrostatic potential, positive in blue and negative in red. Labels of **N** and **C** indicate the direction of **N**-and **C**-termini, respectively. Each molecule in the dimer packs in up side down artificially.*

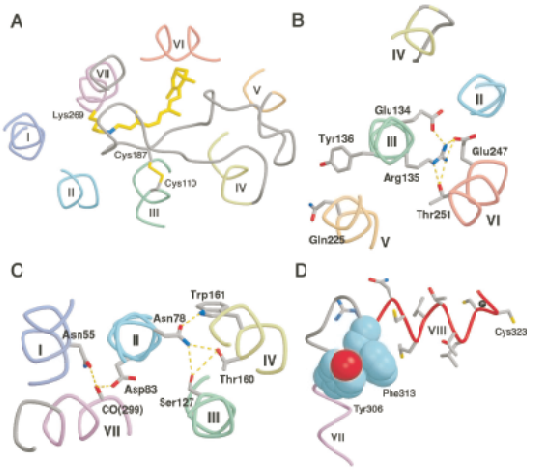

Fig. 4. Structure of highly conserved residues among 7TM receptors.

contained in the 7TM helices (Fig. 3). In fact, α-helices II, VI and VII are clearly kinked, and, in helix VII, several residues around Lys^{296} that binds 11-*cis*-retinal via the Schiff base form a 3_{10} helix. These bent-helices form a spacious cavity that is larger than which is needed to accommodate the bound retinal, while the cytoplasmic side of the helices is tightly bundled (Fig. 3 and Fig. 4A) [6]. The configuration of the reverse agonist, 11-*cis*-retinal, is bow-shaped in 6s-*cis*, 12s-*trans,* and *anti*-C=N of the Schiff base with a direct salt bridge of Asp^{113} (Fig. 5).

The atomic structure of inactive rhodopsin consistently reinforces experimental results obtained to this point, including visual diseases, yielding many clues for further study of the molecular mechanism of 7TM receptor activation, as well as the molecular basis of color vision. Further studies on the activated form of rhodopsin will elucidate novel features of the molecular basis of the 7TM receptor, while the structure of the inactive form is well-suited to the design of antagonists.

Masashi Miyano

SPring-8 / RIKEN

E-mail: miyano@spring8.or.jp

References

[1] J. Bockaert and J. P. Pin, EMBO J. **18** (1999) 1723.
[2] V. M. Unger *et al.*, Nature **389** (1997) 203.
[3] T. Okada *et al.*, J. Struct. Biol. **130** (2000) 73.
[4] Krzysztof Palczewski, Takashi Kumasaka, Tetsuya Hori, Craig A. Behnke, Hiroyuki Motoshima, Brian A. Fox, Isolde Le Trong, David C. Teller, Tetsuji Okada, Ronald E. Stenkamp, Masaki Yamamoto and Masashi Miyano, Science **289** (2000) 739.

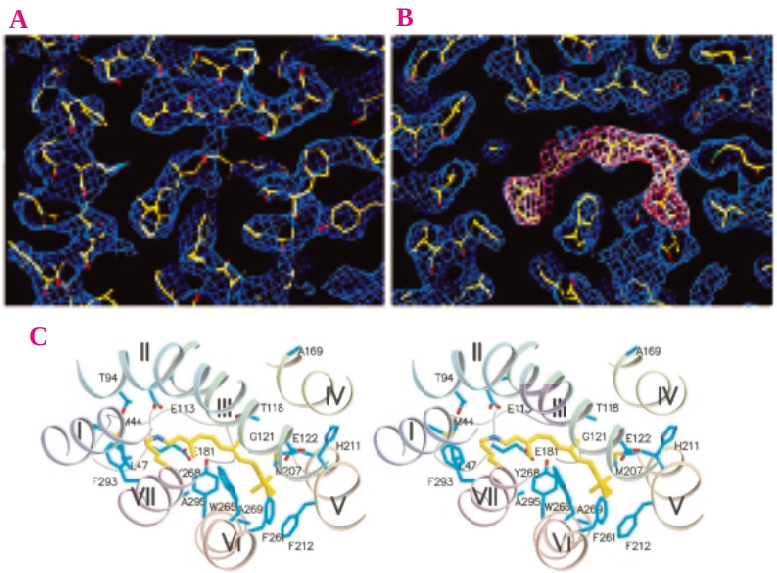

Fig. 5. Closed up structure of bound retinal vicinity.
***A)** Experimental electron density map with the current model at 3.3 Å.*
***B)** 2FoFc and omit FoFc map calculated using model phasing at 2.8 Å.*
***C)** Cartoon model of retinal vicinity in stereo.*

CRYSTALLOGRAPHIC STUDY OF THE METABOTROPIC GLUTAMATE RECEPTOR

The metabotropic glutamate receptor (mGluR) is a key membrane receptor involved in the modulation of excitatory synaptic transmission in the central nervous system. The mGluR plays a crucial role in learning, memory, and some mental disorders, and is therefore a major target for drug-design. To elucidate the mechanism in which ligand-binding triggers the activation of the receptor, we have analyzed the extracellular ligand-binding region of mGluR1 (m1-LBR) using X-ray crystallography [1].

Three different crystal structures of m1-LBR have been determined in a complex with glutamate and in two non-ligand forms. The diffraction data was collected at two beamlines, **BL45XU** (complex form) and **BL24XU** (free forms). For phase determination, we applied the multi-wavelength anomalous diffraction (MAD) method using the facilities at BL45XU. The crystal structures of all the three forms exhibit disulfide-linked homodimers, where “active” and “resting” conformations are modulated through the novel dimeric interface by a packed alpha-helical structure (Fig. 1). The interprotomer disulfide bridge [2] most likely functions as an interprotomer linker which increases the effective concentration of a dimeric form of mGluR1 on the cellular surface. Each protomer consists of two domains: designated as LB1 and LB2. Glutamate is bound in an interdomain crevice (Fig. 2). The differing interdomain arrangements provide an “open” or “closed” conformation of the bi-lobed protomer.

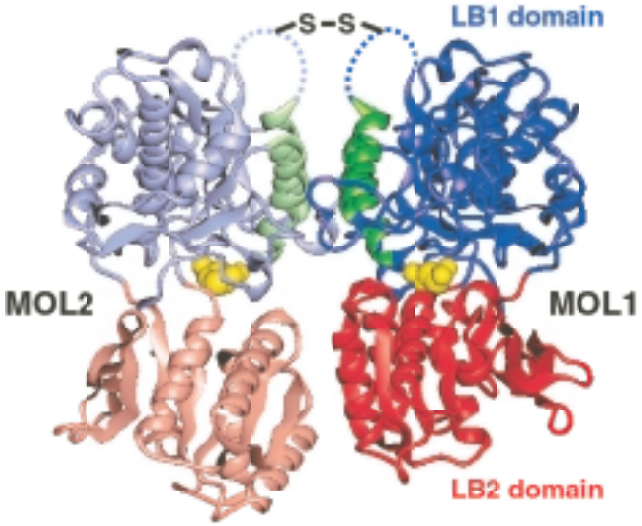

*Fig. 1. Crystal structure of m1-LBR dimer in the glutamate complex form. The MOL1 and MOL2 molecules in the dimer are distinguished by dark and light coloring, respectively. Bound glutamate molecules are shown as yellow space-filling models. Disordered regions with a potential interprotomer disulfide bridge are indicated by dotted lines. Helices **B** and **C**, constituting the dimer interface, are colored green.*

These structures imply that glutamate binding stabilizes both the “active” dimer and “closed” protomer in dynamic equilibrium. The movements of the four domains within the dimer are likely to affect the separation of the transmembrane and intracellular regions, and thereby glutamates with a small molecular size activate the receptor (Fig. 3). This scheme for initial receptor activation could be applied generally to G-protein-coupled neurotransmitter receptors which possess extracellular ligand binding sites.

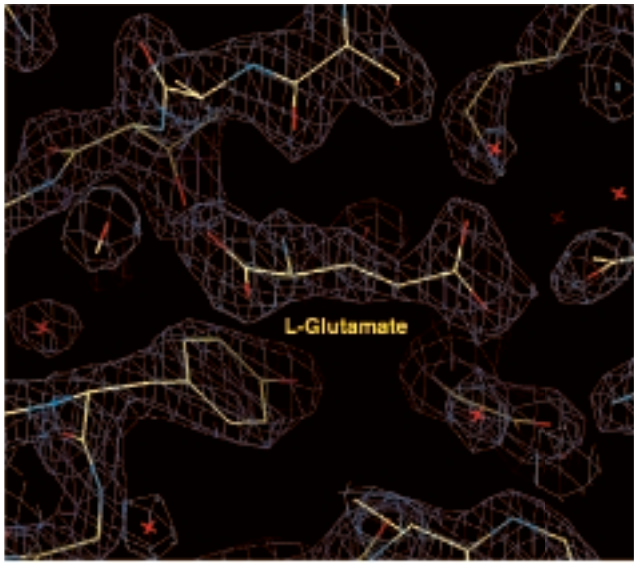

Fig. 2. Final 2Fo-Fc electron density map around the glutamate binding site at 2.2 Å resolution.

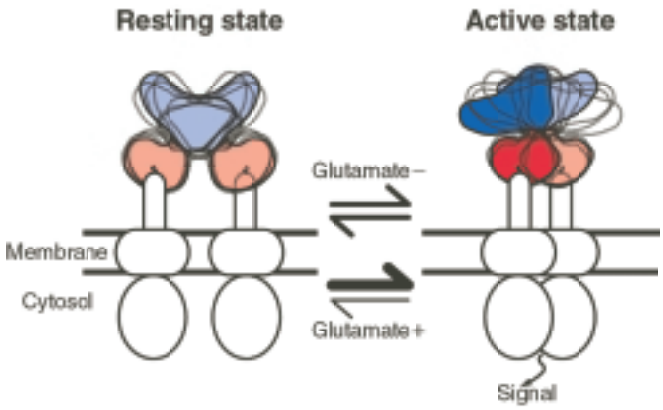

Fig. 3. Potential activation mechanism of mGluR1. The two observed conformations of m1-LBR are represented by solid lines with colors. Open and closed conformations are distinguished by light and dark coloring, respectively. Other unidentified conformations of m1-LBR are indicated by dotted lines. Remaining regions not determined in this study are shown schematically.

Naoki Kunishima[a,b], Hisato Jingami[b] and Kosuke Morikawa[b]

(a) SPring-8 / RIKEN
(b) Biomolecular Engineering Research Institute

E-mail: morikawa@beri.co.jp

References

[1] N. Kunishima, Y. Shimada, Y. Tsuji, T. Sato, M. Yamamoto, T. Kumasaka, S. Nakanishi, H. Jingami and K. Morikawa, Nature **407** (2000) 971.

[2] Y. Tsuji *et al*., J. Biol. Chem. **275** (2000) 28144.

CRYSTAL STRUCTURE OF A REPAIR ENZYME OF OXIDATIVELY-DAMAGED-DNA, MutM (Fpg), FROM AN EXTREME THERMOPHILE, *Thermus thermophilus* HB8

In aerobic organisms, cellular DNA is easily damaged by activated oxygen species resulting from aerobic energy metabolism or oxidative stress. Highly reactive oxygen accelerates the spontaneous mutation rate and therefore has been implicated as a causative agent for aging or the pathogenesis of disease, including cancer. One of the most common products of oxidative DNA damage is the 8-oxoguanine (GO) lesion. GO can pair with cytosine (C) as well as adenine (A), causing conversion from guanine (G) to thymine (T). To prevent mutation, the MutM protein removes GO bases from GO:C pairs in DNA. The *mutM* (*fpg*) gene encoding the MutM protein is highly conserved across a wide range of aerobic bacteria. These enzymes (*Mr*= 30 kDa) possess the invariant N-terminal sequence Pro-Glu-Leu-Pro-Glu-Val-, two strictly conserved lysine residues (Lys52 and Lys147), and a zinc finger motif (-Cys-X2-Cys-X16-Cys-X2-Cys-) at the C-terminus.

We determined the structure of the MutM enzyme derived from an extremely thermophilic bacterium, *Thermus thermophilus* HB8 at 1.9 Å resolution using MAD phasing of the intrinsic Zn^{2+} ion of the zinc finger at beamline **BL45XU** [1-4]. The crystal structure of MutM comprises two distinct domains and a new fold connected by a flexible hinge (Fig. 1). Two molecules are detected in an asymmetric unit within the crystal. The overall conformations of the two independent molecules

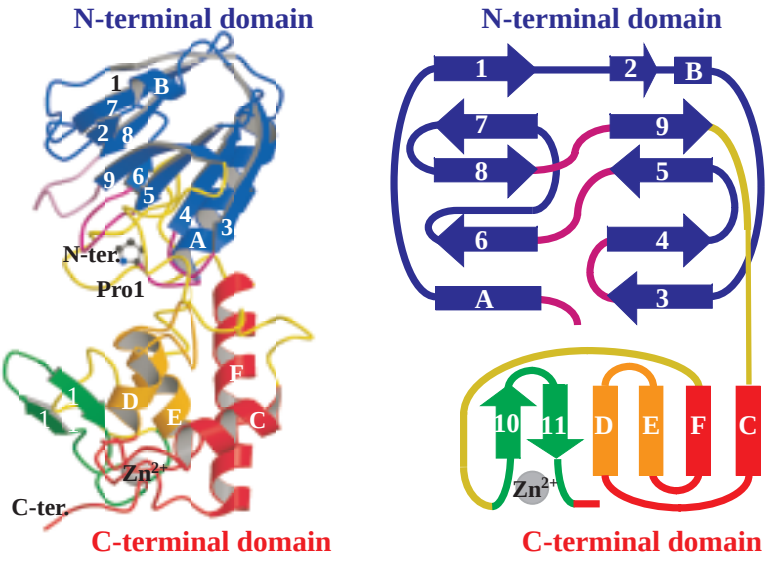

Fig. 1. Overall structure of MutM. The MutM molecule consists of an N-terminal domain (blue), a C-terminal domain (red, orange and green) and two long loops (yellow). The N-terminal domain consists of a two-layered β-sandwich with two alpha helices. The C-terminal domain consists of four α-helix bundles (red and orange) and a β-hairpin loop of the zinc finger motif (green).

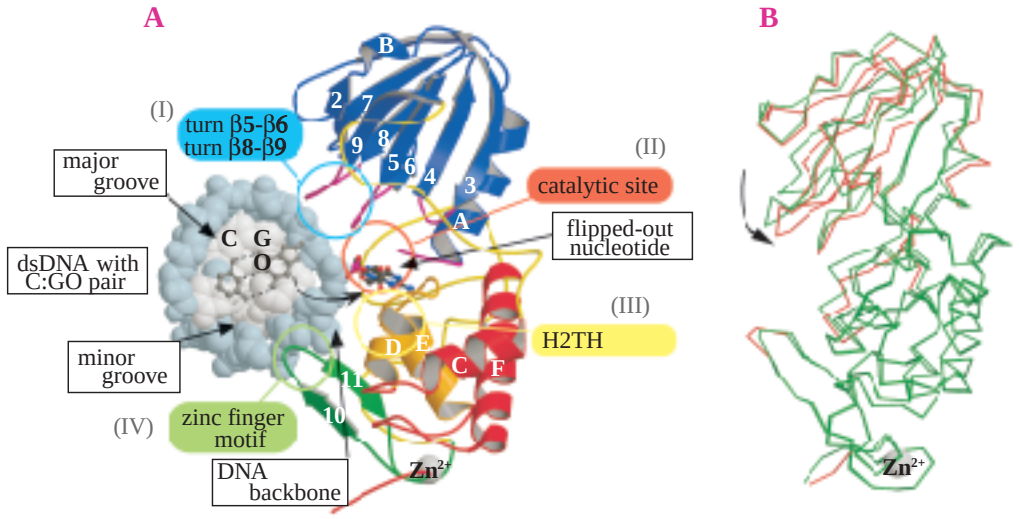

Fig. 2. ***(A)*** *The model of the MutM - DNA complex between the flipped-out DNA and MutM in the closed form was obtained by molecular dynamic calculation. The kinked DNA is drawn as a CPK model with backbones colored in steel blue and with bases in steel gray. C and GO bases and their sugar residues before and after flipping out are shown by ball-and-stick models. All the four conserved regions (I-IV) are in the large cleft of the MutM molecule. The N-terminal domain has access to the major groove of DNA and the zinc finger motif of the C-terminal domain to the minor groove. The H2TH motif of the C-terminal domain is situated near the active site, and may interact with the damaged base of the DNA backbone.* ***(B)*** *There are two conformers in an asymmetric unit. The conformations of the two long loops in the inter-domain cleft differ between the two conformers. These two long loops would work as a hinge in domain movement.*

indicate the existence of significant hinge movement, whereas the individual domains of the two molecules in the asymmetric unit are substantially similar (Fig. 2B). A large, electrostatically positive cleft lined by highly conserved residues exists between the domains.

Based on previous biochemical experiments and the three-dimensional structure, we constructed a structural model of the dsDNA-MutM complex (Figs. 2A and 3) and propose a new reaction mechanism for MutM (Fig. 4). The locations of the putative catalytic residues and the two DNA-binding

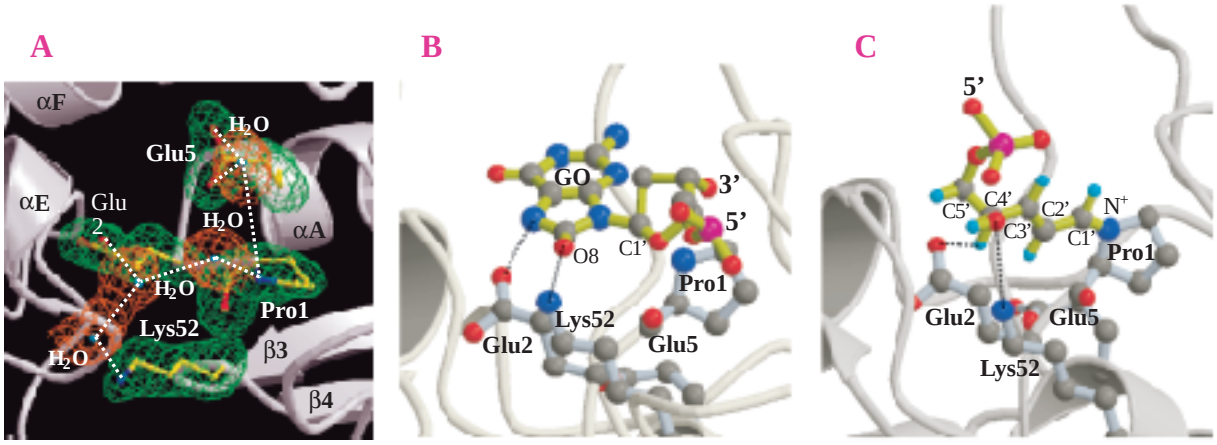

Fig. 3. Architecture of the active site of MutM. ***(A)*** *The nucleophile Pro1 of MutM is surrounded by the invariant charged residues Glu2, Glu5 and Lys52, accompanied by several bound water molecules.* ***(B)*** *Model of docking of the flipped-out GO nucleotide to MutM active site bases on the dsDNA complex.* ***(C)*** *The putative reaction intermediate adduct with Pro1 after β-elimination, which is well defined due to its conjugated double bond and can fit to the active site; the hydroxyl group at C4' of the opened deoxyribose reaches to the carboxylic acid of Glu2, which is a good candidate for proton acceptor.*

motifs (the zinc finger and the helix-two turns-helix motifs) suggest that the oxidized base is flipped-out from double-stranded DNA and excised by a catalytic mechanism in a manner similar to that of bifunctional base-excision-repair enzymes. This model detailing the formation of a dsDNA-MutM complex accounts for the multiple enzymatic activities assigned to MutM. The DNA glycosylase excises various damaged bases from DNA by forming a covalent Schiff base intermediate, which is formed at the damaged site by the nucleophilic attack of the Pro1 secondary amino group at the N-terminus of the deoxyribose C1' to produce an aldehydic abasic site. The AP lyase cleaves the 3'-phosphodiester bond at AP sites through β-elimination. In addition, an alternative AP lyase cleaves the 5'-phosphodiester bond through δ-elimination. These reaction mechanisms also explain the different N-glycosylase/AP-lyase activities among MutM, *E. coli* endonuclease III and T4 endonuclease V. To confirm the detailed mechanism of the MutM N-glycosylase/AP-lyase reactions, mutational analyses of the active-site residues are currently undertaken.

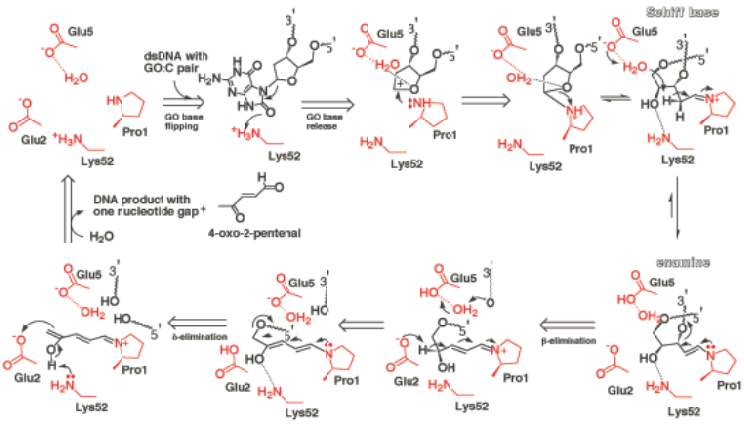

Fig. 4. Schematic representation of the reaction mechanism of MutM N-glycosylase/AP-lyase. We propose that the invariant amino acid residues (Glu2, Glu5, and Lys52) are in the vicinity of the primary catalytic residue Pro1. In this highly electrostatically positive environment, Lys52 may act as a proton donor for depuration of the damaged base (Fig. 3B). After the C2' of deoxyribose forms a Schiff base with Pro1, Glu5 can withdraw the proton of C2' via a bound water molecule, leading to β-elimination. The resulting adduct intermediate (Fig. 3C) would deprotonate at C4' of the opened deoxyribose, leading to δ-elimination. Finally, the recapture of the proton by Lys52 would release the other product, 4-oxo-2-pentenal, to form the gapped dsDNA product. The residues that will contribute to each reaction step were deduced from the crystal structure and are shown in red.

Mitsuaki Sugahara[a*] and Seiki Kuramitsu[a,b]

(a) Osaka University
(b) SPring-8 / RIKEN

present address: SPring-8 / RIKEN

E-mail: sugah@spring8.or.jp

References

[1] T. Mikawa *et al.*, Nucleic Acids Res. **26** (1998) 903.
[2] M. Sugahara *et al.*, J. Biochem. **127** (2000) 9.
[3] M. Sugahara, T. Mikawa, T. Kumasaka, M. Yamamoto, R. Kato, K. Fukuyama, Y. Inoue and S. Kuramitsu, EMBO J. **19** (2000) 3857.
[4] M. Yamamoto *et al.*, J. Synchrotron Rad. **5** (1998) 222.

CRYSTAL STRUCTURE OF CALCIUM PUMP OF SARCOPLASMIC RETICULUM

Nature uses ion gradients across cell membranes very efficiently. When cell membrane excites, ions come into cytoplasm rapidly following the ion gradients. To restore the original resting state, the ions must be pumped back. P-type ATPase is a family of ion transporting ATPases that are responsible for establishing such ion gradients. They include Na^+K^+-ATPase, sarcoplasmic reticulum (SR) Ca^{2+}-ATPase and gastric H^+K^+-ATPase among others. The simplest and a best studied mammalian P-type ATPase is SR Ca^{2+}-ATPase. It consists of a single polypeptide of 110 kDa and transports up to 2 Ca^{2+} per ATP hydrolysis against concentration gradient. When muscle contracts, large amounts of Ca^{2+} stored in SR are released into muscle cells. To relax muscle cells, calcium ions have to be pumped back into SR against concentration gradient. Ca^{2+}-ATPase in SR membrane is responsible for this process. Compared to channels, which can transfer millions of ions per second, pumps work much more slowly. Ca^{2+}-ATPase can transfer only 60 Ca^{2+} per second. To make the relaxation process efficient, SR membrane is full of Ca^{2+}-ATPase (more than 60% of the proteins in SR membrane). Therefore, we can easily obtain sufficient amounts of Ca^{2+}-ATPase for crystallization experiments.

We have been working on this ATPase and determined its structure at 2.6 Å resolution by X-ray crystallography [1] with two calcium ions bound in the transmembrane domain consisting of 10 α-helices (Fig. 1). The crystals used were very thin, typically less than 20 μm. Nevertheless, X-rays available in **BL44B2** and **BL41XU** were powerful enough to collect full data sets from individual crystals very efficiently. In this state, the two calcium ions are located side by side surrounded

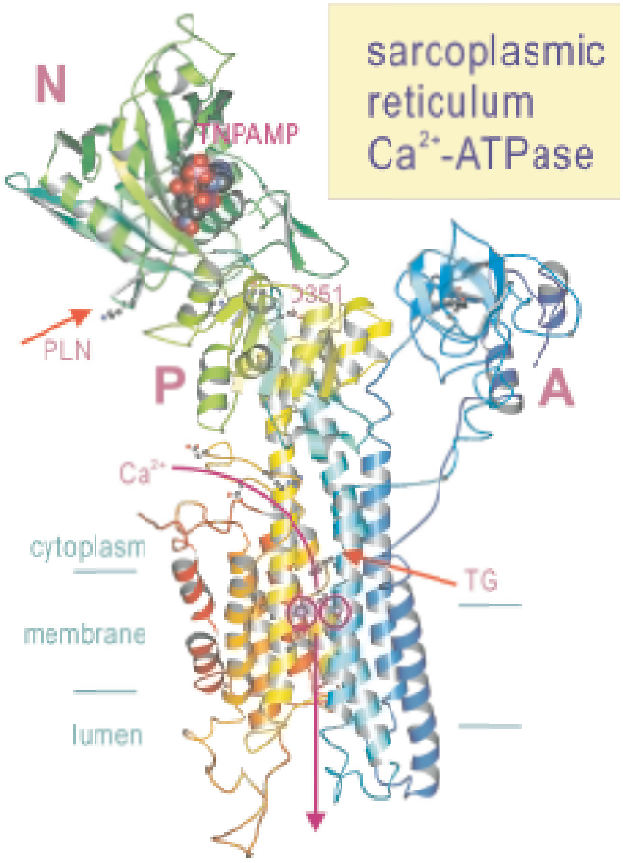

Fig. 1. Architecture of the sarcoplasmic reticulum Ca^{2+}-ATPase. Colour changes gradually from the N terminus (blue) to the C terminus (red). Two purple spheres in the membrane domain represent bound Ca^{2+} ions. Three cytoplasmic domains are well separated and labelled A, N and P. TNP-AMP (an analogue of ATP), in CPK model, is located on domain N and far distant (> 25 Å) from the phosphorylation site (D351), suggesting that domain N will approach domain P when phosphorylation occurs. The binding sites for thapsigargin (TG, a potent inhibitor) and phospholamban (PLN, a regulatory protein in cardiac muscle) are also marked.

by 4 transmembrane helices, two of which are unwound to realize efficient coordination geometry. The cytoplasmic region consists of 3 well-separated domains, with the phosphorylation site (D351) in the central catalytic domain (P) and the adenosine binding site on another domain (N). As a family of ATPases, P-type ATPase has been regarded as a peculiar one, because it lacks the P-loop commonly found in other ATPases and GTPases. The phosphorylation domain has the fold of L-2-haloacid dehalogenase, confirming the proposal by Aravind *et al*. [2]. Thus it is now established that P-type ATPase belongs to a much larger family including enzymes that appear to be totally unrelated to nucleotides.

The atomic model was then fitted to an 8 Å-resolution density map of the enzyme derived by electron microscopy of tubular crystals formed in the absence of Ca^{2+} and the presence of decavanadate [3]. In the tubular crystals the enzyme is considered to be in a state analogous to a phosphorylated (E2P) state. The density map was very well explained by large domain movements in the cytoplasmic region (Fig. 2). By comparing the two models, it has become clear that the enzyme has a mechanism that converts the movements of the cytoplasmic domains to those of the transmembrane helices. This seems to be the mechanism by which calcium ions are transported. Thus, ion transporting ATPases might work like mechanical pumps at the atomic scale.

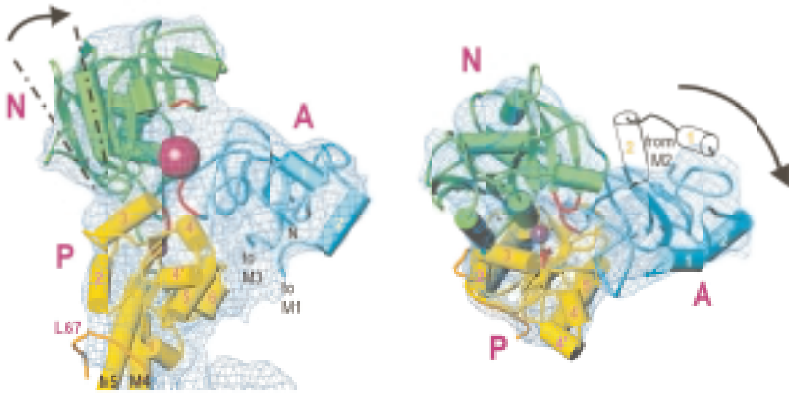

(a) **(b)**

*Fig. 2. Fitting the atomic model obtained for the Ca^{2+}-bound state (arrows and cylinders) to an 8 Å resolution map (blue net) obtained from tubular crystals [3] formed in the absence of Ca^{2+} and presence of decavanadate (large purple sphere in **a**). Overall orientation of the molecule in a is the same as in Fig 1. In **b**, it is viewed from the cytoplasmic side normal to the membrane. The black arrows show the direction of movements from the Ca^{2+}-bound to unbound state.*

Chikashi Toyoshima, Masayoshi Nakasako and Hiromi Nomura

The University of Tokyo

E-mail: ct@iam.u-tokyo.ac.jp

References

[1] C. Toyoshima, M. Nakasako, H. Nomura and H. Ogawa, Nature **405** (2000) 647.

[2] L. Aravind *et al.*, Trends Biochem. Sci. **23** (1998) 127.

[3] P. Zhang *et al.*, Nature **392** (1998) 835.

TIME-RESOLVED X-RAY DIFFRACTION EXPERIMENTS OF PURPLE MEMBRANE

Bacteriorhodopsin (BR) is a proton transporting membrane protein, driven by the energy of absorbed photons. During the first step of proton transport, the absorption of a photon by retinal, located inside BR, induces a conformational change in the molecule from an all-trans to a 13-cis configuration. A sequence of reactions follows to facilitate the transport of protons by BR. Several intermediate states have been characterized by difference spectra in the visible range as J, K, L, M, N, and O. Reprotonation of the retinal Schiff base is an integral reaction in BR proton pump function; the Schiff base receives a proton from D96 during the M-N transition in BR photocycle. Because the pK of D96, located within a hydrophobic microenvironment, is unusually increased, D96 has a protonated form in the unphotolyzed state. Upon the release of the proton, the pK of D96 is lowered by an additional reaction. Therefore, a critical event enabling the lowering of the D96 pK must occur at the M-N transition.

To study the structural transition from the M to the N intermediate, we performed time-resolved X-ray diffraction of purple membrane at the SAXS station of **BL45XU** (Fig. 1) [1]. Stacked purple membranes (two-dimensional crystals of BR) placed on a mylar sheet, relaxed at pH9 and excited at 10 °C by a xenon flash, immediately following the start of diffraction acquisitions. By exposing to X-rays, perpendicular to the membrane plane, stacked purple membranes diffract X-rays circularly in a manner similar to powder diffraction. Diffracted images were averaged circularly. To decompose the component in this reaction, the data were analyzed by singular value decomposition (SVD) (Fig. 2 and Fig.3). Three components are distinguishable from the SVD analysis. U spectra give either the diffraction profiles or the difference profiles of independent components; V spectra display the time course. U1 is similar to the original diffraction pattern of the purple membrane, except for its negative sign, which is influenced by the sign

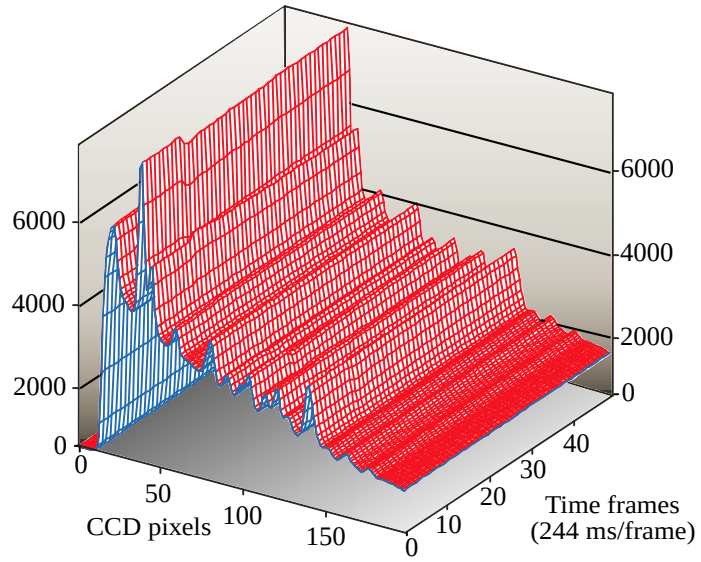

Fig. 1. Time-resolved X-ray diffraction pattern of purple membrane (pH9, 10 °C) before and after xenon flash lamp excitation. Bragg peaks of a magnitude as great as 7 Å are observed, utilizing a time resolution of 244 ms. BR was illuminated at the beginning of the 11th frame.

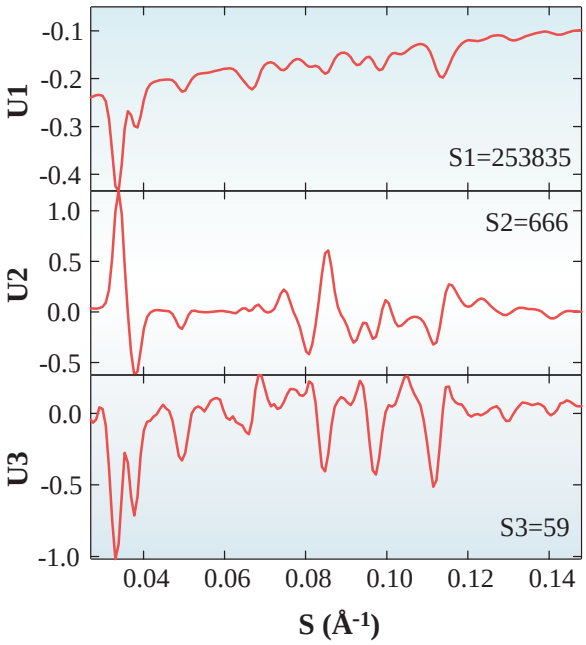

Fig. 2. The U spectra of wild-type BR (pH9, 10 ℃) obtained by SVD analysis for weighted diffraction data. This figure displays the three major components with the singular values. U spectra are either the diffraction profiles or the difference profiles of independent components.

respectively. Utilizing difference Fourier analysis, we examined the two difference diffraction profiles to identify the domains undergoing large conformational changes (Fig. 4). The projections, mapping onto the membrane plane of the two components, demonstrate changes characteristic to the M and N intermediates, respectively. The slow component contains changes near F and G helices; the positive peak on the outside of the F helix becomes higher than the positive peak of the G helix, a characteristic property of the N intermediate. The analysis of the fast component revealed that the positive peak on the outside of the F helix reaches a position as high as the positive peak of the G helix, indicating the F helix alters its structure in this manner during the M-N transition.

Although there is disagreement concerning structural changes during the M-N transition [2], our research reveals that BR changes its structure

of V1. V1 demonstrates little time dependence, indicating that U1 does not change throughout the photocycle. Thus, the first component is composed primarily of the time-independent, basic structure of BR. V2 and V3, however, change dramatically during the flash excitation at time 0, indicating that two unique intermediate conformations exist in the decay process of wild-type BR following flash excitation. As the M and N intermediates only were detected spectrophotometrically in this time period, the two intermediate conformations can be assigned as these intermediates. The three components, derived from the SVD analysis, were reconstituted from global fit analysis to create diffraction profiles of the three states. Absorption and FTIR measurements indicate that the reconstituted profiles are likely to correspond to the unphotolyzed state, the absorption difference between N and the unphotolyzed state and the difference between M and the unphotolyzed state,

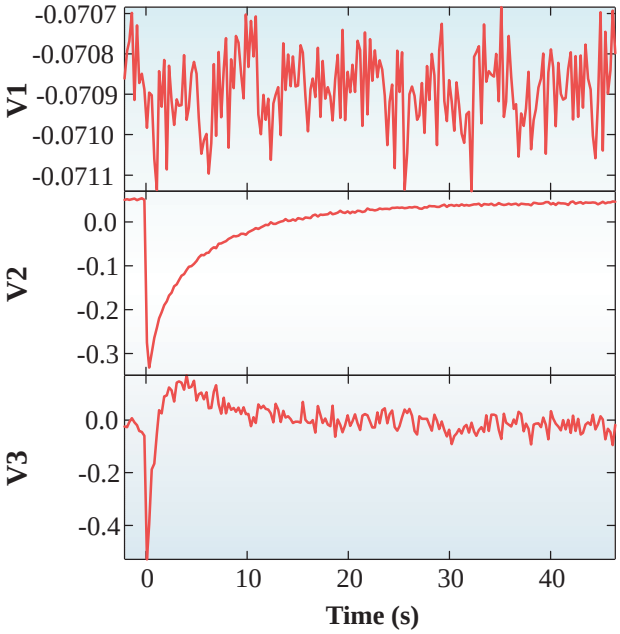

Fig. 3. V spectra of wild-type BR (pH9, 10 ℃) obtained by SVD analysis for weighted diffraction data. V spectra indicate the time course of the corresponding U spectra.

primarily in the M intermediate [3]. Our data demonstrates that global structural changes also occur during the M-N transition. The observed structural change at the F helix likely increases the accessibility of the Schiff base and D96 to the cytoplasmic surface, facilitating the proton transfer reactions beginning with the decay of the M state. We conclude that a large, two-step structural change is integral in the proton pumping activity of BR.

Toshihiko Oka

SPring-8 / RIKEN

E-mail: oka@spring8.or.jp

References

[1] T. Oka, N. Yagi, T. Fujisawa, H. Kamikubo, F. Tokunaga and M. Kataoka, Proc. Natl. Acad. Sci. - in press.

[2] S. Subramaniam *et al.*, J. Mol. Biol. **287** (1999) 145; H. Kamikubo *et al.*, Biochemistry **36** (1997) 12282.

[3] M. Nakasako *et al.*, FEBS Lett. **292** (1991) 73.

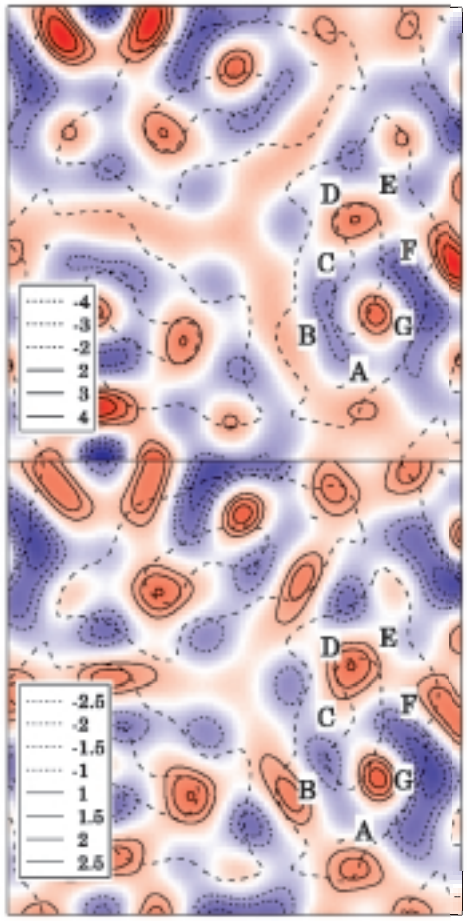

Fig. 4. Difference Fourier maps projected onto the membrane plane of purple membrane samples (pH9, 10 °C). ***(a)*** *Difference map of the N intermediate and the unphotolyzed state.* ***(b)*** *Difference map of the M intermediate and the unphotolyzed state. The dashed line indicates the outline of the BR trimer. Capital letters indicate the rough positions of the seven BR helices.*

HIGH RESOLUTION MICROTOMOGRAPHY OF HUMAN LUNG TISSUE SPECIMENS: OBSERVATION OF NORMAL ANATOMY AND THREE-DIMENSIONAL RECONSTRUCTION

To precisely understand lung function, it is necessary to accurately visualize detailed lung architecture. We used a novel X-ray tomographic technique [1] to study the morphology of human lung at a high resolution.

Postmortem lungs were inflated and chemically fixed by Heitzman's method. Lung samples were sectioned at a 15-mm thickness. Utilizing the present synchrotron radiation computed tomography (CT) system, the entire sample must be contained within the field to enable visualization of multiple viewing angles in a cylinder, 8 mm in diameter. We, therefore, reduced the sample size by carefully removing the edges of the block, yielding a column specimen containing the target site. During this process, we were careful to retain one terminal bronchiole to include the peripheral structure in the column specimen.

The CT images were obtained at **BL20B2** using a phosphor X-ray detector with a cooled CCD camera at an X-ray energy of 9 keV. Synchrotron radiation CT images effectively captured the alveolar wall, the air spaces, and small airways. Alveolar septa were visualized at an effective spatial resolution of approximately 24 μm, experimentally determined in the present synchrotron radiation CT system. Detailed correlation between the synchrotron radiation microtomography and histology can be achieved by precise spatial registration [2].

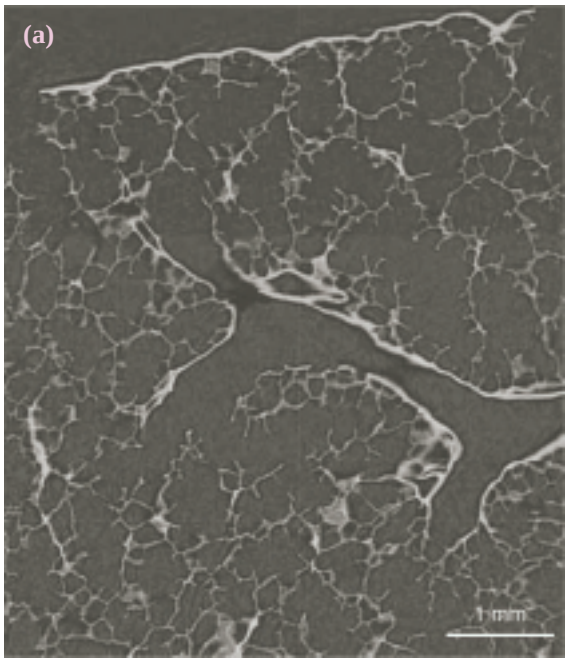

Fig. 1(a). Planar reformatted image.

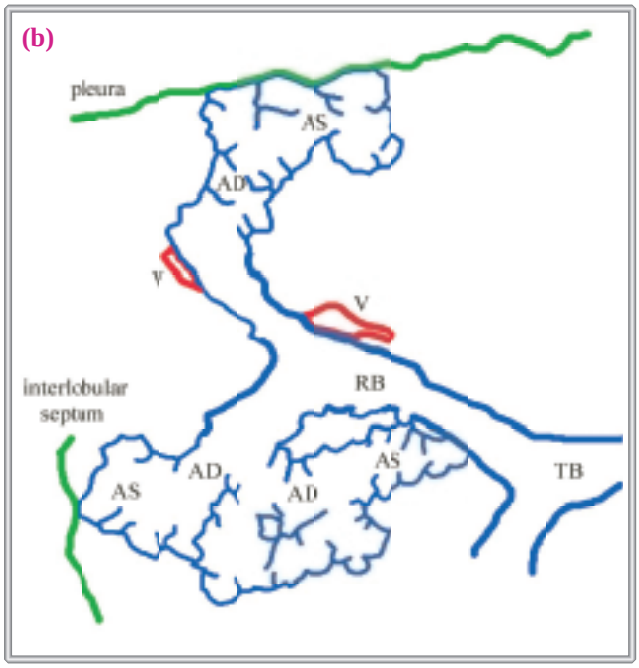

Fig. 1(b). TB = terminal bronchiole
RB = respiratory bronchiole
AD = alveolar duct
AS = alveolar sac
V = pulmonary vessel

Using the nearly-parallel, synchrotron radiation beam, comprehensive isotropic volumetric data can be obtained in multiple cross-sectional planes, throughout the full three-dimensional volume of the tissue. Serial analysis of these synchrotron radiation CT images allowed us to identify the terminal bronchiole, the respiratory bronchiole, the alveolar duct, and the alveolar sac. We reformatted the para-sagittal planar image from the three-dimensional isotropic volumetric data with a high resolution (Fig. 1a) to systematically confirm the structural sequence; the respiratory bronchiole originates from the terminal bronchiole (TB), sequentially branches off into alveolar ducts (AD) and terminates in the alveolar ducts abutting on either the pleura or the interlobular septum (Fig. 1b).

An alveolar duct, distal to the bronchiole-alveolar duct junction, communicates with all alveoli in the ventilatory unit defined in our studies. For each voxel within the air spaces, we calculated the distance to the nearest voxel on the boundary, assigning this value to the voxel as the density value. A subsequent volume rendering technique allowed interactive viewing of the segmented structure in the appropriate viewing perspective without hidden structures (Fig. 2). This three-dimensional imaging technique, possessing a high isotropic spatial resolution, offers a new mechanism to analyze the acinar geometry, necessary to accurately define the physiology of the human lung.

Three-dimensional, super-resolution imaging of the inflated and fixed human lung, utilizing the combination of synchrotron radiation and histology, establishes a novel, fundamental approach allowing greater understanding of the human lung. Deeper understanding of the normal lung architecture and the consequent morphological modifications resulting from physiopathological conditions will hopefully allow advances in biomedicine.

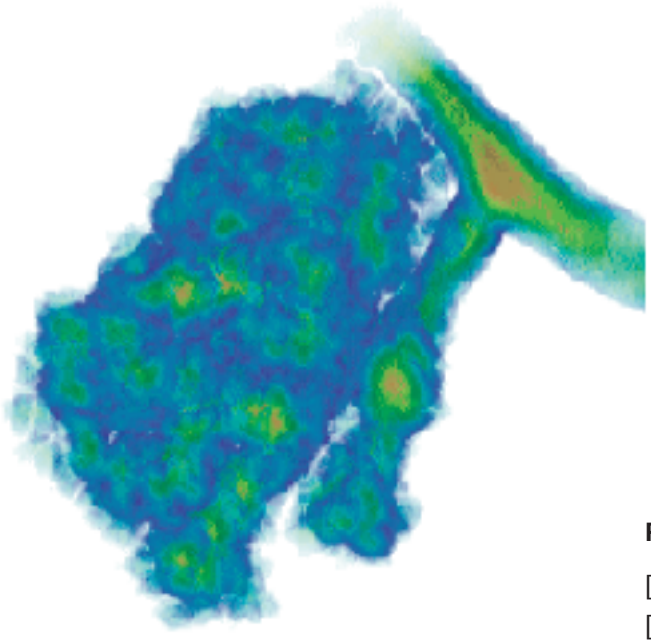

Fig. 2. Three-dimensional reconstruction of the sub-acinus.

Kenji Shimizu[a,b], Junpei Ikezoe[a] and Naoto Yagi[c]

(a) Ehime University School of Medicine
(b) Yamaguchi University
(c) SPring-8 / JASRI

E-mail: simi@kinchu.hosp.go.jp

References

[1] K. Uesugi *et al.*, Proc. SPIE **3772** (1999) 214.
[2] K. Shimizu, J. Ikezoe, H. Ikura , H. Ebara, T. Nagareda, N. Yagi, K. Umetani, K. Uesugi, K. Okada, A. Sugita and M. Tanaka, Proc. SPIE **3977** (2000) 196.

Diffraction & Scattering

*The number of beamlines at SPring-8, which are basically used for Diffraction and Scattering experiments, is steadily increasing. The beamlines are BL02B1, BL02B2, BL04B1, BL04B2, BL08W, BL09XU, BL10XU, BL39XU and few others. Their classification here is casual and as a matter of convenience. The beamlines numbered BL**B2 are newly installed and tested in 1999-2000. Reflecting the increase in the number of beamlines, the scope of activities in diffraction and scattering experiments at SPring-8 is getting wider and more profound. In the field of diffraction and scattering, it has become increasingly difficult to select the scientific works to be published in Research Frontiers as examples of the remarkable scientific achievements accomplished at SPring-8. Among the outstanding studies undertaken here at SPring-8, seven scientific works have been selected for publication in this volume. Surprisingly enough, four out of seven are from BL**B2.*

Moritomo et al. have discovered the phase separation of $Nd_{0.55}(Sr_{0.17}Ca_{0.83})_{0.45}MnO_3$ *and discuss insulator-metal behavior of CMR manganites based on a novel scenario. Tanigaki et al. have synthesized germanium clathrate with d-electron system,* $Ba_8Mn_2Ge_{44}$ *and determined its structure. Takata et al. have succeeded in elucidating the structure of IPR (Isolated Pentagon Rule)-violated fullerene,* $Sc_2@C_{66}$*, where IPR has been considered as the essential rule in fullerene geometry. Ito et al. have observed the temperature variation of the spin- and orbital-magnetic moment of Holmium Iron Garnet. Seto et al. have measured the nuclear resonant scattering of 40 K using synchrotron radiation for the first time. Kohara et al. have identified obtained an accurate structure factor of vitreous* B_2O_3 *up to a high scattering Q (~35*A^{-1}*). Funakoshi et al. have precisely measured the viscosity of albite melt under high pressure using an in situ observation of the falling sphere method.*

There has been a steady increase in activity at SPring-8 in the field of Diffraction & Scattering along with the increases in the number of beamlines.

Makoto Sakata

PHASE SEPARATION AND INSULATOR-METAL BEHAVIOR OF CMR MANGANITES

The doped manganites, $R_{1-x}Ca_xMnO_3$, where R is a trivalent rare-earth metal, have a distorted-perovskite structure with three-dimensional networks of the MnO_6 octahedra. Their generic behavior of paramagnetic-to-ferromagnetic transition is understood within the framework of double-exchange theory. We need to consider additional effects in order to understand the insulator-metal behavior as well as the colossal magnetoresistance (CMR). At present, the most probable candidate is the *percolation* model [1], in which the insulator-metal behavior occurs when the percolation pass of the metallic (ferromagnetic metallic; FM) is connected from one end to the other regions in the sea of the insulating (charge-ordered insulating; COI) state. The charge-ordering transition of doped manganites usually accompanies an antiferromagnetic transition with the CE-type structure, while the FM state is of half-metallic. Here, to judge the suitability of this model, we have performed a synchrotron radiation X-ray powder diffraction experiment on $Nd_{0.55}(Sr_{1-y}Ca_y)_{0.45}MnO_3$ at beamline **BL02B2** with high angular resolution and counting statistics [2].

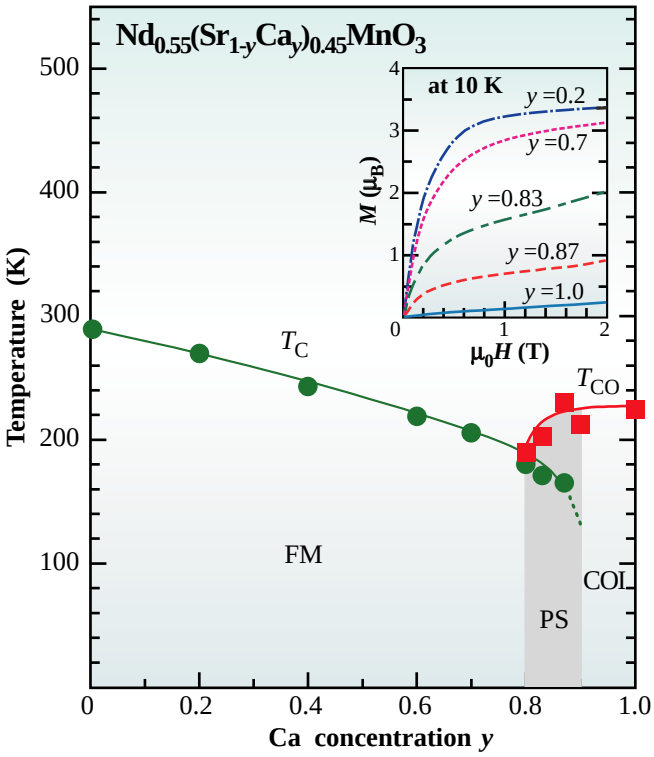

Fig. 1. Electronic phase diagram of $Nd_{0.55}(Sr_{1-y}Ca_y)_{0.45}MnO_3$. COI, FM and PS represent the charge-ordered insulating, ferromagnetic metallic and phase-separated states, respectively. Inset shows magnetization curves at 10 K.

To choose an appropriate chemical composition for the present study, we first have synthesized a series of ceramics $Nd_{0.55}(Sr_{1-y}Ca_y)_{0.45}MnO_3$, finely controlling the one-electron bandwidth through chemical pressure. Powder X-ray diffraction measurements at room temperature along with Rietveld analysis indicate that the samples were single phase without detectable impurities. Figure 1 shows an electronic phase diagram of $Nd_{0.55}(Sr_{1-y}Ca_y)_{0.45}MnO_3$. The Curie temperature T_C and the charge-ordering temperature T_{CO} were determined from the temperature-variation of the magnetization M and resistivity ρ. The insulator-metal behavior was enhanced in the proximity of FM-COI phase boundary (hatched region of Fig. 1). Thus, we have chosen $Nd_{0.55}(Sr_{0.17}Ca_{0.83})_{0.45}MnO_3$ for present investigation. The inset shows the magnetization curves measured at 10 K. The suppressed magnetization curve at 0.83 suggests a coexistence of the FM and antiferromagnetic COI phases [3].

In Fig. 2, we demonstrate prototypical examples of the X-ray powder diffraction patterns of $Nd_{0.55}(Sr_{0.17}Ca_{0.83})_{0.45}MnO_3$ at 265 K and 110 K. At 110 K we observed remarkable splitting of the Bragg reflections, indicating the phase separation (see inset of Fig. 2(b)). We have analyzed the powder patterns below 200 K using a two-phase model with two distorted-perovskites (*Pbnm*; Z = 4). The Rietveld refinements are satisfactory, in which R_{wp} and R_I (reliable factor based on the integrated intensities) are fairly typical of published structures. These two perovskite phases can be characterized by a lattice constant c. Hereafter, we will refer to the respective phases as 'short-c' (7.54 - 7.58 Å) and 'long-c' (7.60 - 7.62 Å) phases.

Figure 3 shows temperature variation of (a) resistivity ρ, (b) lattice constants and (c) intensity of the magnetic Bragg reflections of $Nd_{0.55}(Sr_{0.17}Ca_{0.83})_{0.45}MnO_3$. The most important point here is that the lattice constants indicate a discontinuous change at T_{CO}. In other words, the system is transformed into a two-phase state, *both of which differ from the room temperature phase*. Such a state is perhaps ascribed to the random nucleation of a low-temperature phase and subsequent stress-induced growth of the secondary phase (*stress-induced phase separation*). With further temperature decrease, an insulator-metal transition takes place at 157 K (= T_{IM}).

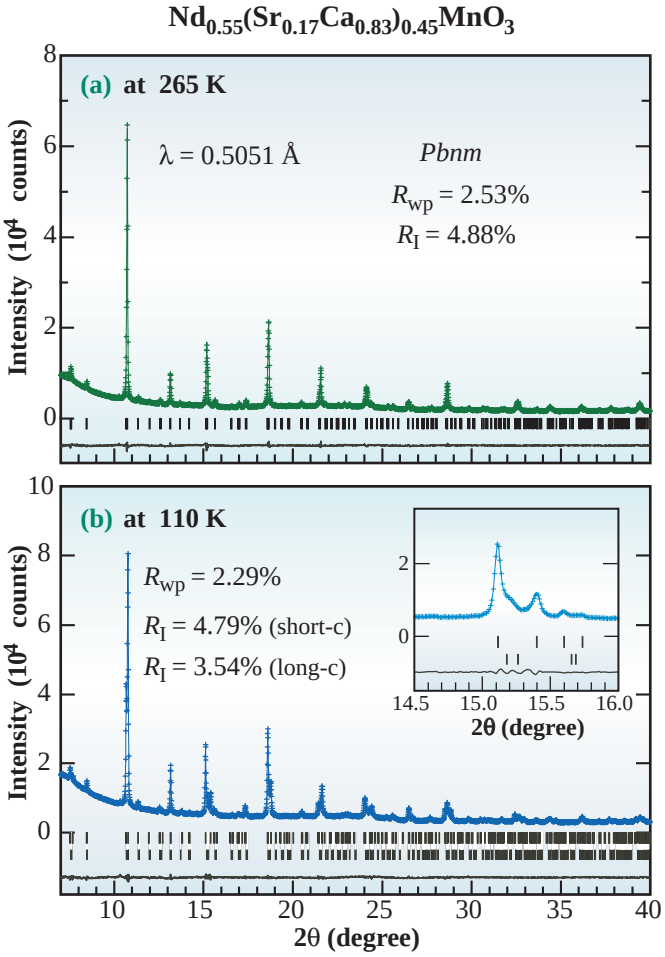

*Fig. 2. X-ray powder diffraction patterns (crosses) of $Nd_{0.55}(Sr_{0.17}Ca_{0.83})_{0.45}MnO_3$ at **(a)** 265 K and **(b)** 110 K. The solid curve is the result of the Rietveld analysis with a model for **(a)** single distorted-perovskite (Pbnm; Z = 4) and **(b)** two distorted-perovskites, respectively.*

The bottom panel of Fig. 3 shows integrated intensities of the magnetic Bragg reflections. The three magnetic reflections, that is, F-, A- and CE-types, seem to appear at the same temperature near T_{IM}. The F- and A-type (CE-type) components can be ascribed to the long-*c* (short-*c*) phase based on the lattice constants. The magnetic ordering at lower temperatures below T_{CO} *contradicts* to the percolation model. In addition, the volume ratio of the insulating short-*c* component rather decreases with cooling.

A new scenario for the insulator-metal behavior

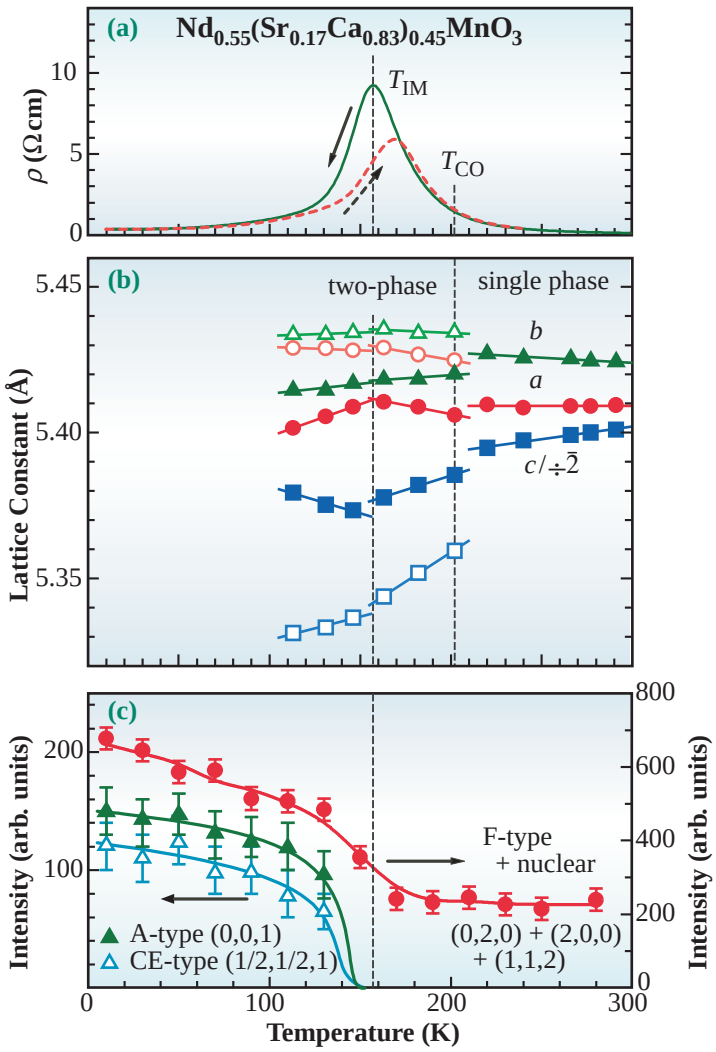

Fig. 3. Temperature dependence of ***(a)*** *resistivity ρ,* ***(b)*** *lattice constant and* ***(c)*** *intensity of the magnetic Bragg reflections of* $Nd_{0.55}(Sr_{0.17}Ca_{0.83})_{0.45}MnO_3$. *Open and closed symbols represent the short-c and long-c phases, respectively.*

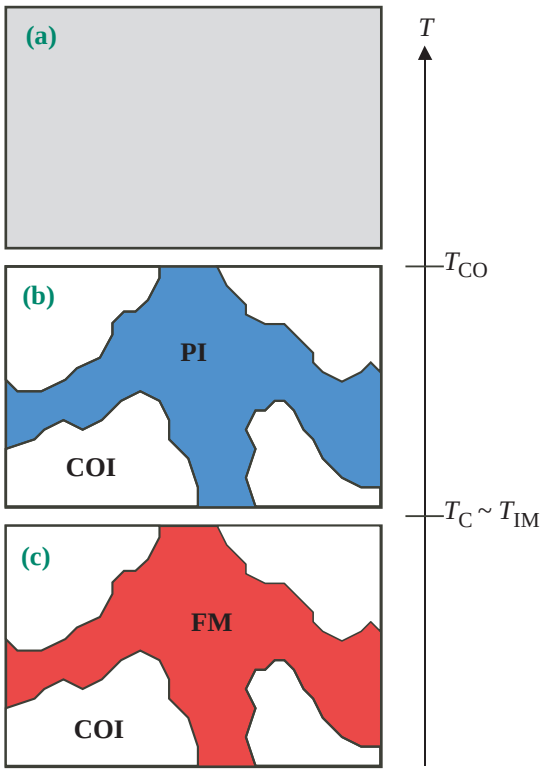

Fig. 4. Schematic illustrations of the mechanism for the insulator-metal behavior: ***(a)*** *$T > T_{CO}$,* ***(b)*** *$T_{IM} < T < T_{CO}$ and* ***(c)*** *$T < T_{IM}$. COI, PI and FM stand for the charge-ordered insulating, paramagnetic insulating and ferromagnetic metallic phases, respectively.*

is as follows. With a decrease in temperature below T_{CO}, the system is transformed from a single phase (Fig. 4(a)) to the two-phase state (Fig. 4(b)), possibly due to the stress-induced phase separation. These phases, that is, the short-*c* and long-*c* phases, can be ascribed to the COI and paramagnetic insulating (PI) phases, respectively. With further decrease of temperature below T_{IM}, the long-*c* phase indicates a PI to FM phase transition (Fig. 4(c)). If the metallic region were connected, the apparent insulator-metal transition would be observed.

Yutaka Moritomo and Akihiko Machida

Nagoya University

E-mail: moritomo@cirse.nagoya-u.ac.jp

References

[1] M. Uehara, *et al.*, Nature **399** (1999) 560.
[2] A. Machida, *et al.*, Phys. Rev. B **62** (2000) 3883.
[3] Y. Moritomo *et al.*, Phys. Rev. B **60** (1999) 10374.

GERMANIUM CLATHRATE WITH *d*-TRANSITION ELEMENT

New aspects in magnetism have recently arisen with the advent of nano-materials. Nano-cage materials directed to magnetism have become one of the most important issues in materials science, as seen in endohedral-fullerenes [1] and in a series of rare-earth boron compounds [2,3]. Giant magneto-resistance in manganese copper-oxides has also gained intense interests from the scientific and technological fields which concentrates on the unique interactions between magnetic- and conduction-electrons [4,5].

In this system, the long-distant magnetic *d*-electrons can interact with each other through nano-scale spacing in an isotropic three-dimensionality, leading to the occurrence of a unique spontaneous spin-ordering at 10 K.

The clathrate $Ba_8Mn_2Ge_{44}$, was made by simply melting the stoichiometric amounts of the elements using an RF-induction furnace under an argon atmosphere. It should be noted that the germanium atoms are melt followed by self-assembling into the clathrate structure during the process of natural

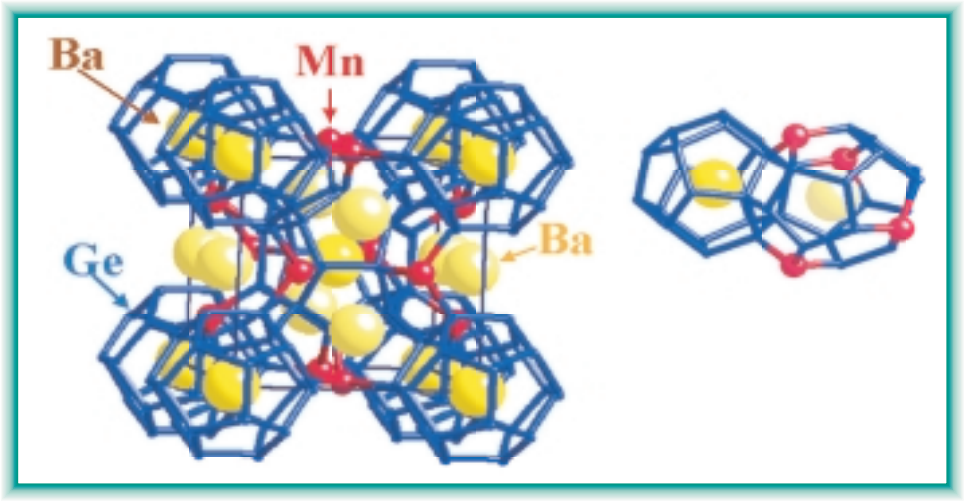

Fig. 1. Structure of Ge_{46} Clathrates endohedrally encapsulating Ba and magnetic d-electron Mn.

We have taken a new approach in designing a novel magnetic material on a model of germanium nano-cluster crystals with a polyhedral cage structure [6], where *d*-block element Mn resides on the position connecting Ge_{20} dodecahedra cluster cages and alkaline-earth metals Ba are encapsulated inside the cluster cages as shown in Fig. 1 [7]. The both elements thus introduced act as independent sources of magnetic- and conduction- electrons.

cooling. The product obtained was then analyzed by X-ray diffraction measurements at room temperature using synchrotron radiation at beamline **BL02B2** as shown in Fig. 2.

Preliminary Rietveld refinement using a Cerius [2] program has been performed, assuming that two Mn atoms reside on the crystallographic *6c* positions and eight Ba atoms are spherically encapsulated both inside the dodecahedral Ge_{20}

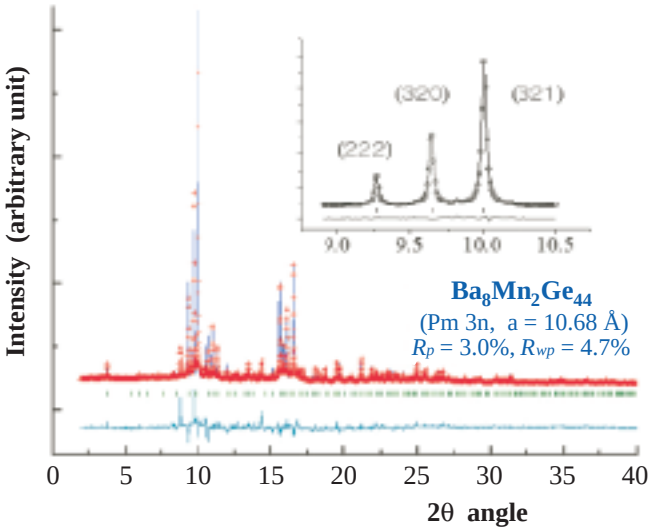

Fig. 2. High resolution X-ray diffraction spectrum of $Ba_8Mn_2Ge_{44}$.

and tetrakaidecahedral Ge_{24} cages (at the *2a* and *6b* positions). This resulted in a reasonable R_{wp} factor of 4.7%. The lattice parameter of $Ba_8Mn_2Ge_{44}$ at room temperature is 10.68 Å with a space group of Pm-3n. This is the first compound that accommodates *d*-electron element Mn in germanium type I clathrates. Since Ba is encapsulated, the compound is air-stable like endohedrally-doped C_{82}, being compared to the fact that C_{60} fullerides are generally air-sensitive.

Expecting new magnetic properties in $Ba_8Mn_2Ge_{44}$, we measured the magnetization under a low magnetic field. When the temperature was decreased from 20 K to 1.8 K under 10 G, a spontaneous magnetization was observed with a steep increase in intensity at 10 K, as seen in Fig. 3. A hysteresis was also observed when the magnetic field was scanned in a loop of 100 G at 1.8 K. These results demonstrate that a ferromagnetic transition occurs in this crystal. It should be emphasized that the observation of the ferromagnetic behavior is not due to the conventional magnetic direct-interactions. It is unambiguous that the ferromagnetic ordering occurs in this dilute magnetic system (9 wt% of Mn), since a hysteresis was seen as shown in the inset of Fig. 3 even though the value is small.

We have also used another mode to investigate magnetic behavior. First, the temperature was set at 1.8 K under a zero-field within the experimental errors of our SQUID apparatus, and magnetization was monitored under 10 G with increasing temperature to 16 K. Interestingly, the curve observed in this zero-field cooling mode (ZFC) showed a small different temperature dependence from that in the field cooling mode (FC). This is quite unusual for conventional ferromagnetic interactions.

Although it still needs the further investigation to have a satisfactory elucidation about the mechanism of the magnetism in this compound, it would at least be worthwhile to discuss here. One of the most important factors responsible for the occurrence of the magnetic orderings is likely the increase in the density of states at the Fermi level $N(E_F)$ associated with conduction electrons from Ba as well as a little itineration of *s,d*-electrons on Mn. In fact, when Mn is replaced by another nonmagnetic element like Au, no significant magnetization was

observed in $Ba_8Au_6Ge_{40}$, supporting the idea that the *d*-electrons on Mn atoms are essentially involved in the magnetic phenomena observed at low temperatures. Considering the large average interval of 8.3 Å between Mn atoms, it is plausible to suppose here that the spin ordering of the *d*-electrons can result from their RKKY like interactions via the conduction electrons spreading over the clathrate network.

Since the new aspects in magnetism described in the present paper can be realized with nano-scale control in the position of the elements, clathrates with magnetic elements will provide a good scientific stage for shedding a new light on magnetism in nano scale.

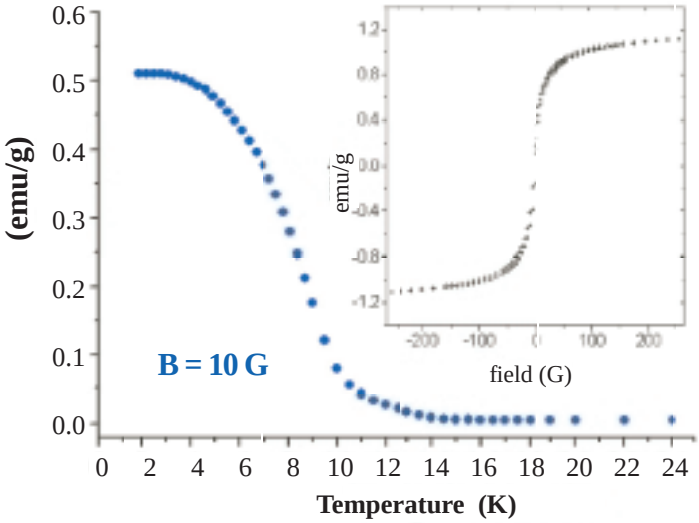

Fig. 3. Spontaneous magnetization curve of $Ba_8Mn_2Ge_{44}$ measured under 10 G.

Katsumi Tanigaki[a,b], Tetsuji Kawaguchi[a] and Masahiro Yasukawa[c]

(a) Osaka City University
(b) PRESTO, Japan Science and Technology Corp.
(c) CREST, Japan Science and Technology Corp.

E-mail: tanigaki@sci.osaka-cu.ac.jp

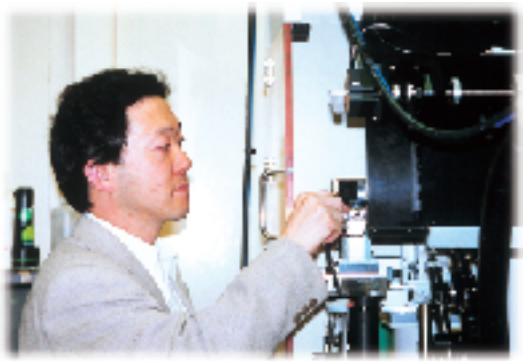

References

[1] T. Ogawa *et al.*, J. Am. Chem. Soc. **122** (2000) 3538.
[2] T. Susaki *et al.*, Phys. Rev. Lett. **82** (1999) 992.
[3] D.P. Young *et al.*, Nature **397** (1999) 412.
[4] S. Jin *et al.*, Science **264** (1994) 413.
[5] Y. Tokura *et al.*, J. Phys. Soc. Jpn. **63** (1994) 3931.
[6] H. Kawaji *et al.*, Phys. Rev. Lett. **74** (1995) 1427.
[7] R.F.W. Herrmann, K. Tanigaki, T. Kawaguchi, S. Kuroshima and O. Zhou, Phys. Rev. B **60** (1999) 13245; T. Kawaguchi, K. Tanigaki and M. Yasukawa, Appl. Phys. Lett. **77** (2000) 3438.

STRUCTURE OF IPR-VIOLATED FULLERENE, $Sc_2@C_{66}$

Isolated-pentagon rule (IPR) [1,2], stating that the most stable fullerenes are those in which all pentagons are surrounded by five hexagons, has been considered as the most important and essential rule in governing the geometry of fullerenes. In fact, all the fullerenes produced, isolated and structurally characterized to date have been known to satisfy IPR [3-5]. There are no IPR fullerenes possible between C_{60} and C_{70}, and so the observation of any fullerenes in that range means the violation of the IPR. Recently, Shinohara *et al.* have reported the first production, isolation of an IPR-violating metallofullerene, $Sc_2@C_{66}$ [6]. Immediately after the first production and isolation of $Sc_2@C_{66}$, the IPR-violated structure of the fullerene was determined for the first time [6] using synchrotron radiation powder data by the Maximum Entropy Method (MEM) combined with Rietveld analysis, MEM/Rietveld Method [5,7].

The purity (99.8%) of the material was confirmed by laser-desorption time-of-flight mass spectrometry. $Sc_2@C_{66}$ powder sample grown from toluene solvent was sealed in a silica glass capillary (0.3 mm inside diameter). X-ray powder pattern with good counting statistics was measured by the synchrotron radiation (SR) X-ray powder experiment with imaging plate (IP) as detectors at beamline **BL02B2** (Fig. 1). The exposure time on IP was 2 hours. The wavelength of incident X-rays was 0.75 Å. The X-ray powder pattern of $Sc_2@C_{66}$ was obtained with a 0.02° step up to 20.3° in 2θ, which corresponds to 2.0 Å resolution in *d*-spacing. By pre-Rietveld analysis of the MEM/Rietveld Method, the $Sc_2@C_{66}$ crystal structure is determined as that of space group $Pmn2_1$ (No.31); a=10.552(2) Å, b=14.198(2) Å, c=10.553(1) Å. The result of the pre-Rietveld fitting is shown in Fig. 2. The reliable factors of the pre-Rietveld fitting were R_{wp} = 2.4% and R_I = 13.1%.

Although there are a number of ways to violate IPR, the most straightforward way being to generate the so-called “fused-pentagon” where

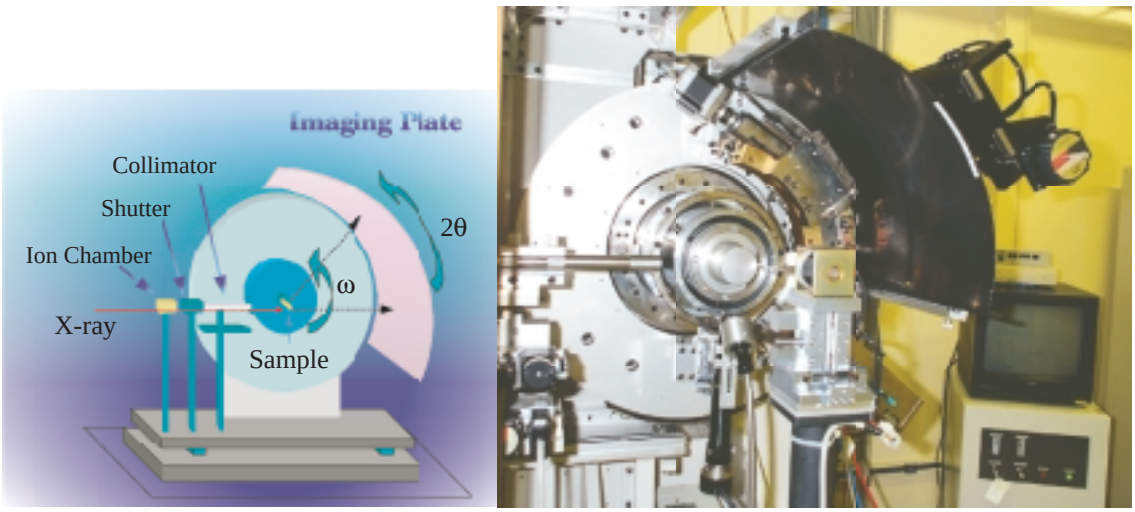

Fig. 1. The large Debye-Scherrer camera at BL02B2.

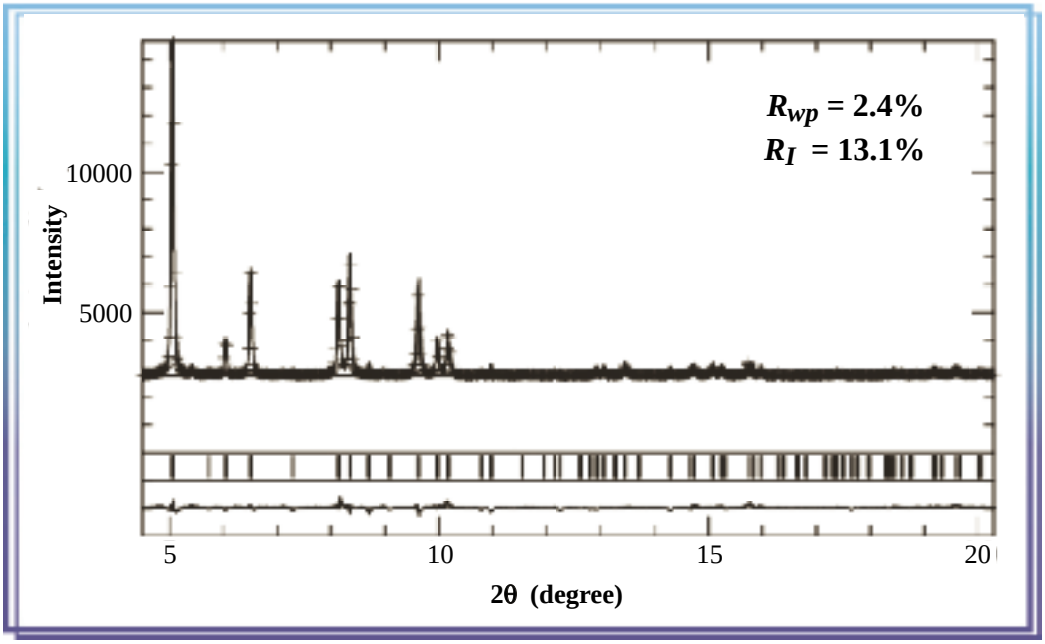

Fig. 2. Fitting result of pre-Rietveld analysis for the $Sc_2@C_{66}$ crystal.

pentagons are adjacent with each other. For 66-atom carbon cages with hexagonal and pentagonal faces, there are in total 4478 possible (non-IPR) structural isomers with $2\times D_3$, $1\times C_{3v}$, $18\times C_{2v}$, $112\times C_s$, $211\times C_2$ and $4134\times C_1$ symmetry [8]. Considering the observed 19-lines (5×2; 14×4) in the high resolution ^{13}C NMR spectrum of $Sc_2@C_{66}$, only 8 structural isomers of C_{66} with C_{2v} symmetry are compatible with this ^{13}C NMR pattern [6].

The MEM 3-D electron density distribution of $Sc_2@C_{66}$ is presented in Fig. 3(a) together with the $Sc_2@C_{66}$ geometry optimized by the non-local density function B3LYP/Basis set [Sc(LanL2DZ); C(3-21G)] calculations (Fig. 3(b)). The MEM charge densities, which has reliable factor of R_F=5.4%, clearly exhibit a pair of two-fold fused-pentagons on a C_{66}-C_{2v} cage that encapsulate a Sc_2 dimer. The present $Sc_2@C_{66}$ structure has the least number and degree of fused-pentagons out of the 4478 possible isomers.

$Sc_2@C_{66}$ shown in Fig. 3(b) contains two pairs of tow-fold fused pentagons to which the two Sc atoms are closely situated. The observed Sc-Sc distance is 2.87(9) Å, indicating the formation of a Sc_2 dimer in the C_{66} cage. The intrafullerene electron transfers in endohedral metallofullerenes have been known to play crucial roles in stabilizing the metallofullerenes [3-5,9,10]. The number of electrons in the area corresponding to Sc_2 dimer from the MEM charge density is 40.0(2) *e*, which is very close to that of $(Sc_2)^{2+}$ with 40 *e*. The *ab initio* calculation also indicates that the Sc_2 dimer donates two electrons to the C_{66} cage providing a formal electronic state of $(Sc_2)^{2+}@C_{66}^{2-}$. It is this charge-transfer interaction between the Sc_2 dimer and the fused pentagons that significantly decreases the strain energies caused by the pair of fused pentagons and thus stabilizes the fullerene cage. IPR is not necessarily a test for the stable geometry of endohedral metallofullerenes [6,9].

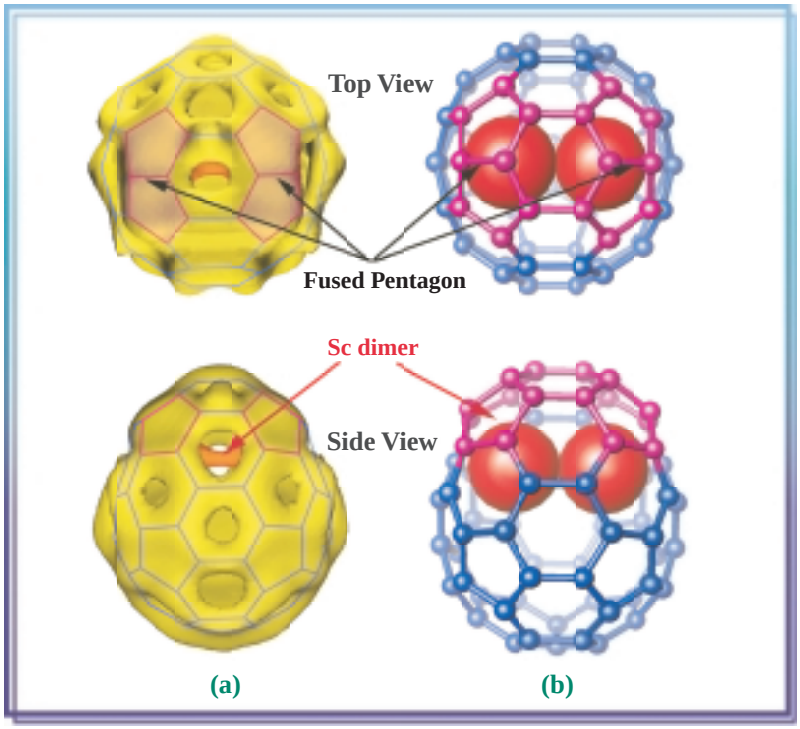

Fig. 3. ***(a)*** *The X-ray structure of the IPR-violating $Sc_2@C_{66}$ fullerene showing a top view along the C_2 axis and a side view. The equi-contour (1.4 e Å^{-3}) surface of the final MEM electron charge density. The Sc_2 dimer is colored in red. The two pairs of fused-pentagons are clearly seen.* ***(b)*** *The calculated $Sc_2@C_{66}$ structures.*

Masaki Takata, Eiji Nishibori and Makoto Sakata

Nagoya University

E-mail: a41024a@nucc.cc.nagoya-u.ac.jp

References

[1] H. Kroto, Nature **329** (1987) 529.
[2] T.G.Schmalz *et al.*, J. Am. Chem. Soc. **110** (1988) 1113.
[3] H. Shinohara *et al.*, Nature **357** (1992) 52.
[4] C.S. Yannoni *et al.*, Science **256** (1992) 1191.
[5] M. Takata *et al.*, Nature **377** (1995) 46; M. Takata *et al.*, Phys. Rev. Lett. **83** (1999) 2214.
[6] C-R. Wang *et al.*, Nature **408** (2000) 426.
[7] M. Takata, E. Nishibori and M. Sakata, Z. Kristallogr. **216** (2001) 71.
[8] P.W. Fowler and D.E. Manolopoulos, An Atlas of Fullerenes (Clarendon, Oxford, 1995) 27.
[9] K. Kobayashi *et al.*, J. Am. Chem. Soc. **119** (1997) 12693.
[10] H.C. Dorn *et al.*, in Fullerenes: Recent Advances in the Chemistry and Physics of Fullerenes and Related Materials (eds. K.M. Kadish & R.S. Ruoff) 990. (The Electrochemical Society, Pennington, 1998).

TEMPERATURE VARIATION OF SPIN- AND ORBITAL-MAGNETIC FORM FACTOR OF HOLMIUM IRON GARNET BY X-RAY MAGNETIC DIFFRACTION

X-ray magnetic diffraction with the use of elliptically polarized synchrotron radiation is a unique tool which enables us to take separate measurements of spin- and orbital-magnetic moments of ferromagnets [1]. These magnetic moments are fundamental physical quantities and give us essential knowledge regarding magnetism. To date, the white beam method [2-5] which utilizes elliptically polarized white X-rays of bending-magnet radiation, has been the most extensively employed technique. In the present experiment we have adopted an advanced method by utilizing a monochromatic beam. This method utilizes highly brilliant undulator radiation and a phase plate. One advantage of the monochromatic beam method is its capability of more precise measurements, as it is not subject to fluorescent X-rays and multiple scattering as much as the white beam method.

The monochromatic beam method was applied to a determination of the spin- and orbital-magnetic form factor of Holmium Iron Garnet, $Ho_3Fe_5O_{12}$, at various temperatures between 60 K and 300 K. This compound is a ferrimagnet with a compensation temperature (Tc) of approximately 130 K, at which the total magnetization vanishes. The total magnetization is composed of the magnetic moments of Ho and Fe atoms. The dominant component of the total magnetization, which is the Ho moment below the Tc, is believed to be switched to the Fe moment above the Tc. In this experiment, we aim to determine how the spin- and orbital-magnetic moments of this compound vary through the compensation temperature.

The experiment was performed at the undulator beamline **BL39XU**, where a phase plate made of diamond crystal is installed [6]. The phase plate is an X-ray optical device utilized to control the polarization of synchrotron radiation and to generate elliptically polarized radiation. The phase plate system has been successfully applied to MCD measurements at this beamline [7], and to the X-ray magnetic diffraction measurement [8]. The present study is the first case in which a phase plate was applied in the X-ray magnetic diffraction, together with the third-generation undulator radiation.

The prepared single crystal specimen of the compound was made by the LPE method. Elliptically polarized X-rays out of the phase plate were irradiated on the specimen and the diffraction intensity of the (880) reflection plane was measured using an APD detector [9]. The scattering angle to the specimen was set at the 90 degrees. The specimen was kept in a refrigerator to maintain the desired temperature between 60 K and 300 K. The specimen was also kept under a magnetic field of 0.6 Tesla by an electromagnet. The diffraction intensities were measured by reversing the magnetization direction (referred to as a magnetic effect or a flipping ratio). The magnetic field was applied in two ways; (i) along the incident beam and (ii) along the diffraction beam. The former measurement gives us the orbital-magnetic form factor at the 880 reciprocal lattice point, $\mu_L(880)$, and the latter measurement gives us the total magnetic form factor (orbital+spin), $\mu_{L+2S}(880)$.

In Fig. 1, the observed values of the $\mu_L(880)$ and

the $\mu_{L+2S}(880)$ are shown between 60 K and 300 K. Solid circles and solid squares represent the $\mu_L(880)$ and the $\mu_{L+2S}(880)$, respectively. Above the compensation temperature, which is 130 K, the absolute values of the $\mu_L(880)$ and the $\mu_{L+2S}(880)$, are shown by the open circles and open squares, respectively. It is noted in Fig. 1 that (i) the signs of both $\mu_L(880)$ and $\mu_{L+2S}(880)$ are reversed at the compensation temperature, (ii) the absolute values of the both $\mu_L(880)$ and $\mu_{L+2S}(880)$ decrease monotonically as the temperature increases. The estimated statistical error bars, which are not shown in the figure, are about the same as the size of data point. The solid lines and dashed lines in Fig. 1 represent the fitted cubic curves for the absolute values of the $\mu_L(880)$ and the $\mu_{L+2S}(880)$, respectively. From these fitted curves the spin-magnetic form factor $\mu_{2S}(880)$ was derived as $\mu_{2S}(880) = \mu_{L+2S}(880) - \mu_L(880)$ and is plotted in Fig. 2. We see, that the sign of the $\mu_{2S}(880)$ is opposite to that of the $\mu_L(880)$ and the absolute value of the $\mu_{2S}(880)$ decreases monotonically as the temperature increases. This is the first measurement of the temperature variation in the spin- and orbital-magnetic form factor of this compound.

Both Ho and Fe atoms contribute to the total magnetic form factor of this compound. Assuming that the orbital moment of Fe is quenched, as is almost the case for 3*d* transition-metal atoms, the total magnetic form factor is composed of the following three components; (a) the orbital moment of Ho, (b) the spin moment of Ho, and (c) the spin moment of Fe. The $\mu_L(880)$ would come from the orbital-magnetic form factor of Ho. The change in the sign of the $\mu_L(880)$ at the compensation temperature directly indicates the direction reversal of the magnetic moment of Ho. The $\mu_{2S}(880)$ is composed of the spin moments of Ho and Fe. In

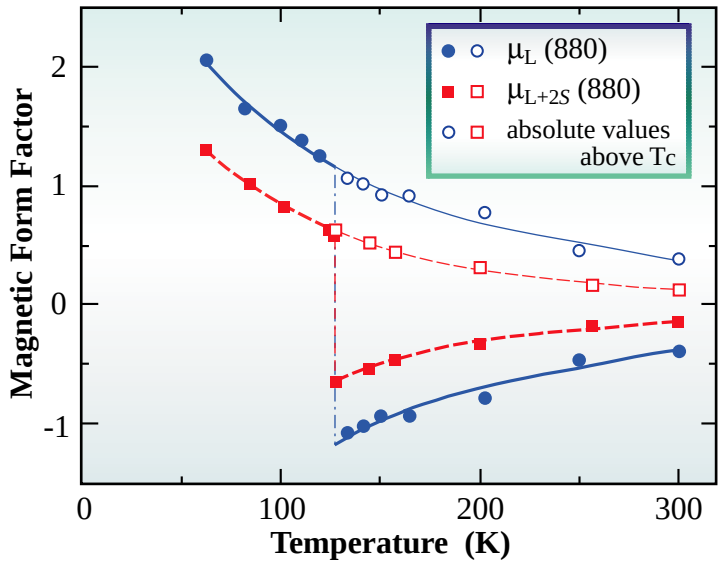

Fig. 1. Temperature variation of orbital-magnetic form factors (solid circles) and total magnetic form factors (solid squares) of Holmium Iron Garnet at the 880 reciprocal lattice point, $\mu_L(880)$ and $\mu_{L+2S}(880)$, respectively. Open circles and open squares represent absolute values of the form factors above the compensation temperature Tc (130 K). Solid lines and dashed lines represent the fitted cubic curves for the absolute values of $\mu_L(880)$ and $\mu_{L+2S}(880)$, respectively. Thicker lines are drawn for the data represented by solid circles and squares.

order to separate Ho and Fe contribution in the spin-magnetic form factor, further experiments and/or analyses are needed. Therefore we plan to obtain the spatial distribution of the spin and orbital moments of Ho and Fe in the compound.

In conclusion, (i) the spin- and orbital-magnetic form factors of the Holmium Iron Garnet at the 880 reciprocal lattice point were measured between 60 K and 300 K for the first time; (ii) both the magnetic form factors show the change in the sign at the compensation temperature which is the direct observation of the reversal of the magnetic moment direction; and (iii) the absolute values of both magnetic form factors indicate a monotonic decrease as the temperature increases.

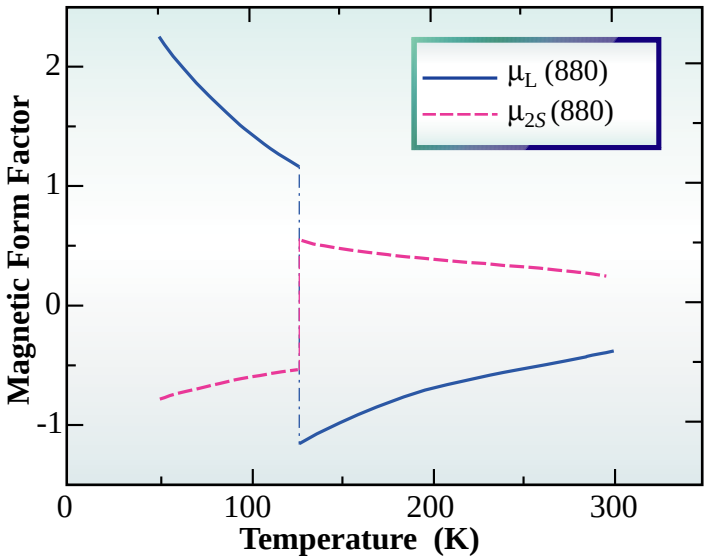

Fig. 2. Orbital-magnetic form factor $\mu_L(880)$ (solid lines) and spin-magnetic form factor $\mu_{2S}(880)$ (dashed lines). $\mu_{2S}(880)$ are derived from the fitted curves of $\mu_L(880)$ and $\mu_{L+2S}(880)$, as $\mu_{2S}(880) = \mu_{L+2S}(880) - \mu_L(880)$.

Masahisa Ito[a], Etsuo Arakawa[b] and Hiroshi Maruyama[c]

(a) Himeji Institute of Technology
(b) Tokyo Gakugei University
(c) Okayama University

E-mail: itom@sci.himeji-tech.ac.jp

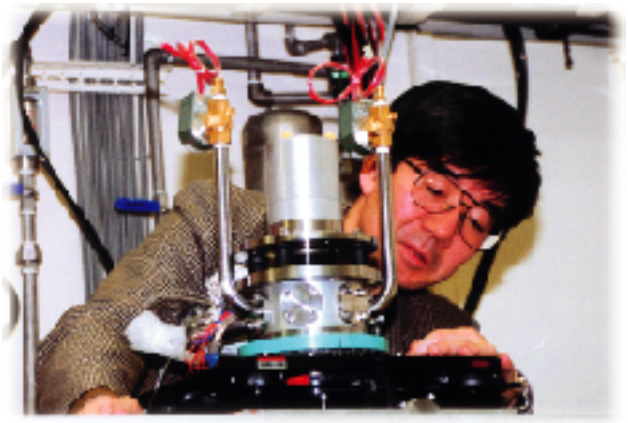

References

[1] M. Blume and D. Gibbs, Phys. Rev. B **37** (1988) 1779.
[2] D. Laundy *et al.,* J. Phys. Condens. Matter **3** (1991) 369.
[3] S. P. Collins *et al.,* Philos. Mag. B **65** (1992) 37.
[4] M. Ito *et al.,* J. Phys. Soc. Jpn. **64** (1995) 2333.
[5] D. Laundy *et al.* , J. Synchrotron Rad. **5** *(1998)* 1235.
[6] M. Ito, E. Arakawa, M. Suzuki, N. Kawamura, K. Hirano, S. Kishimoto, H. Maruyama and K. Namikawa, in preparation.
[7] H. Maruyama *et al.,* J. Synchrotron Rad. **6** (1999) 1133.
[8] M. Ito and K. Hirano, J. Phys. Condens. Matter **9** (1997) L613.
[9] S. Kishimoto *et al.,* to be published in Nucl. Instrum. Meth. in Phys. Res. A (2001).

NUCLEAR RESONANT SCATTERING OF SYNCHROTRON RADIATION BY ^{40}K

For the hyperfine-interaction studies of nuclear resonant scattering, synchrotron radiation has a number of distinct advantages when compared with a conventional radioactive source. In addition, the use of synchrotron radiation allows a direct measurement of the spectrum of phonon energy in solids or the diffusive motion of atoms in liquids. Although the energy tunability of synchrotron radiation allows performing nuclear resonance excitation experiments of various nuclides, the resonance excitation with synchrotron radiation has been confined only for a few isotopes. Therefore, the increase of the nuclides that can be excited with synchrotron radiation is extremely important. Among these nuclides, potassium is one of the most important elements in material and biological sciences, and a Mössbauer resonance has been observed for the potassium isotope ^{40}K [1,2]. Due to the lack of any radioactive parent nuclide populated for the 29.83 keV first excited state of ^{40}K, it was impossible to observe the Mössbauer effect by implementing ordinary radioactive sources. For this reason, inbeam methods for nuclear reactions {(*d, p*) and (*n, γ*) reactions} on the predominant potassium isotope ^{39}K were adopted to observe the Mössbauer effect, however, resulting in serious damage of the sample, which is frequently used as a source. This brought the ^{40}K nuclide to be one of the most important nuclides for nuclear resonance excitation experiments with synchrotron radiation. We have now measured the nuclear resonant scattering of synchrotron radiation using ^{40}K for the first time [3].

The experiments were performed at the JAERI beamline **BL11XU** . The storage ring was operated in a 116-bunch mode, giving a bunch distance of 41.3 ns. The measured sample was KCl powder, whose isotope ratio of ^{40}K was 4.03%. A double crystal Si(3 3 3) monochromator produced incident X-ray radiation with a bandwidth of ~ 2 eV at an energy of ~ 29.83 keV. An Al plate of 2 mm thick was placed in front of the slits to reduce the first harmonic radiation (9.94 keV) passing through the monochromator. A Si-avalanche photodiode detector

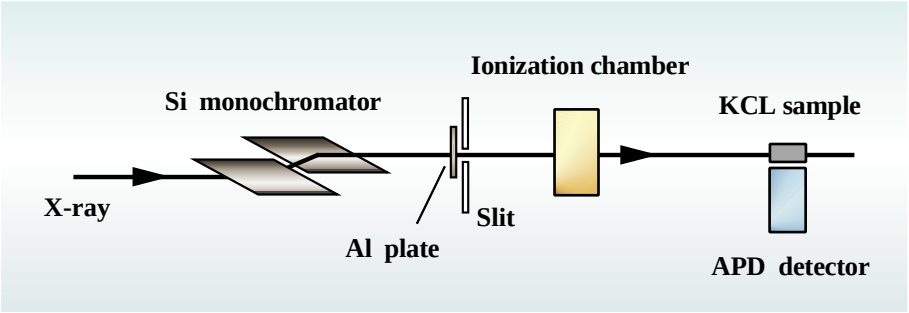

Fig. 1. Experimental setup.

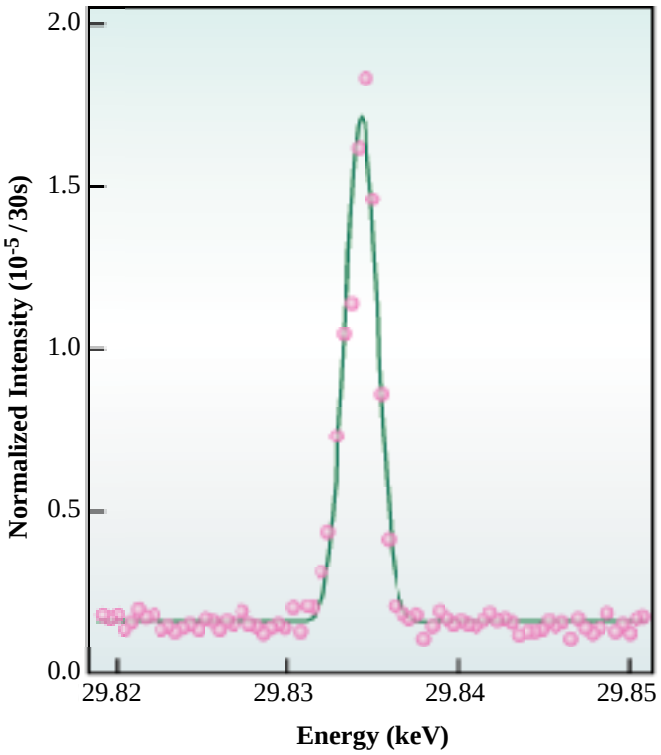

Fig. 2. Energy spectrum of delayed emission from ^{40}K in KCl. Solid circles represent the delayed counts normalized by the counts of the prompt scattering. The solid line is a Gaussian fit to the normalized delayed counts.

with a diameter of 3 mm was used to detect the scattering from the KCl sample [4]. Figure 1 shows the experimental setup. To search the nuclear resonance excitation of ^{40}K, we performed an energy scan of the incident X-ray radiation by changing the Bragg angle of the Si(3 3 3) monochromator. The measured energy spectrum is shown in Fig. 2. The nuclear resonance scattering by ^{40}K is clearly observed. In this measurement, the absolute energy of the first excited state of ^{40}K was obtained as 29.834 ± 0.011 keV, which was in good agreement with the previous reported value of 29.8299 ± 0.0006 keV [5]. The measured time spectrum of nuclear resonant scattering from ^{40}K in the KCl sample is shown in Fig. 3. In the time spectrum, no quantum beat was observed, which coincided with the cubic-symmetrical electronic states of K^+ ions in KCl crystal. Therefore, the observed spectrum can be fitted with a simple exponential time distribution. From this spectrum, the half-life of the first excited state was found as 4.13 ± 0.12 ns, being consistent with the value of 4.24 ± 0.09 ns previously reported [5].

In conclusion, we were capable of observing the nuclear resonant excitation of the first excited state of ^{40}K and have measured the time evolution of the decay. Our observation of the nuclear resonance excitation of ^{40}K indicates the possibilities in electronic and vibrational studies on potassium. This promises a bright future in the study of potassium in both material and life sciences.

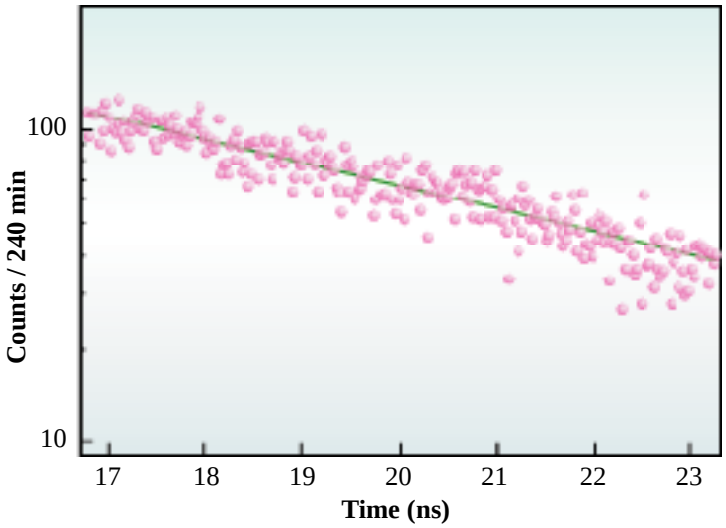

Fig. 3. Time distribution of the nuclear resonant scattering of synchrotron radiation by ^{40}K in KCl. The measured spectrum (solid circles) is fitted by an exponential function, and the half-life of the first excited state of ^{40}K was evaluated to be 4.13 ± 0.12 ns.

Makoto Seto

Kyoto University

E-mail: seto@rri.kyoto-u.ac.jp

References

[1] S.L. Ruby and R.E. Holland, Phys. Rev. Lett. **14** (1965) 591.

[2] D.W. Hafemeister and E. Brooks Shera, Phys. Rev. Lett. **14** (1965) 593.

[3] M. Seto, S. Kitao, Y. Kobayashi, R. Haruki, T. Mitsui, Y. Yoda, X. W. Zhang and Yu. Maeda, Phys. Rev. Lett. **84** (2000) 566.

[4] S. Kishimoto, Nucl. Instrum. Meth. A **309** (1991) 603.

[5] P. M. Endt, Nucl. Phys. A **521** (1990) 1.

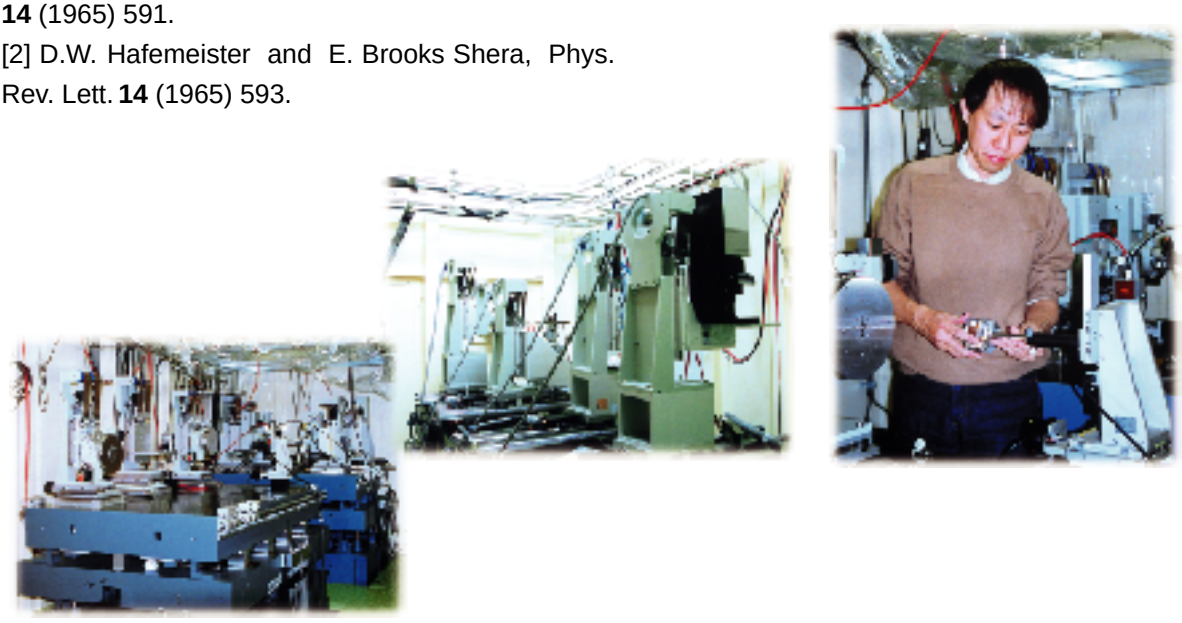

HIGH-ENERGY X-RAY STUDY OF THE STRUCTURE OF VITREOUS B_2O_3

High-energy X-ray ($E \geq 30$ keV) diffraction (HEXRD) using a synchrotron radiation source affords several advantages in studies of the structures of encapsulated liquids and glasses in transmission geometry, including: (i) higher resolution in real space due to a wide range of momentum transfer ($\hbar Q$), (ii) smaller correction terms (especially for absorption), (iii) the use of extreme sample environments (high-temperature, high-pressure), and (iv) the ability of direct comparison between X-ray and neutron diffraction data. The HEXRD technique, in conjunction with model calculations and neutron diffraction experiments, comprises one of the best methods available for investigating the structure of liquids and glasses.

This study was undertaken in order to investigate the short- and intermediate-range structure of vitreous B_2O_3. High-energy (40.9 keV [1] and 61.7 keV) synchrotron X-ray diffraction experiments were performed to obtain an accurate structure factor, $S(Q)$, for vitreous B_2O_3 up to high Q (~ 35 Å^{-1}), with small systematic corrections. The X-ray diffraction measurements were carried out at **BL04B2** and **BL14B1** bending magnet beamlines. The reverse Monte Carlo (RMC) modelling technique [2] was then applied to both the HEXRD and the published neutron diffraction data [3]. RMC simulations were carried out on a system containing 4000 atoms using the X-ray-weighted and neutron-weighted [3] total structure factors $S(Q)$, simultaneously. On the basis of the RMC model, we discuss the validity of the boroxol ring model for vitreous B_2O_3.

The experimental X-ray-weighted and neutron-weighted structure factors, $S^X(Q)$ and $S^N(Q)$, are shown as red lines in Fig. 1. $S^X(Q)$ exhibits significant oscillations up to the maximum Q value

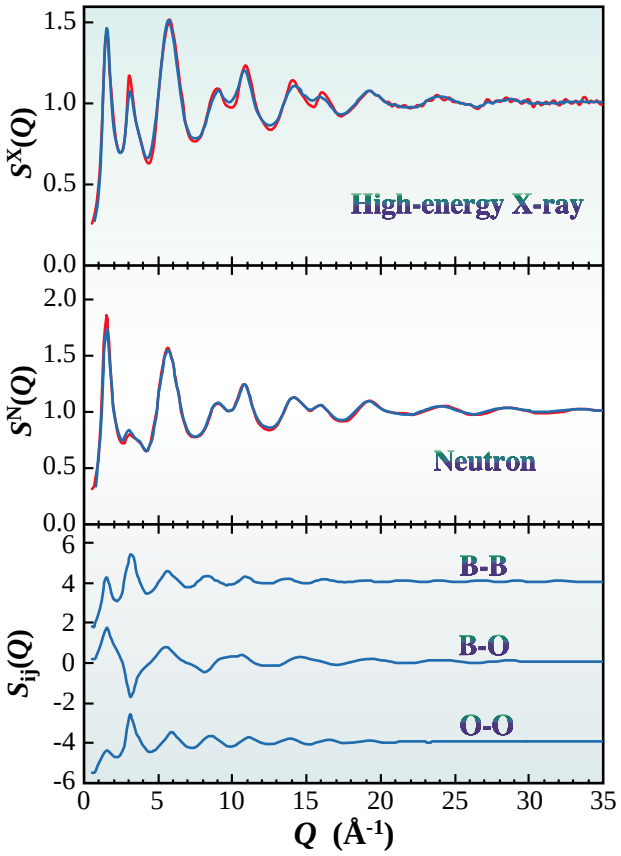

Fig. 1. Total and partial structure factors, $S^{X,N}(Q)$ and $S_{ij}(Q)$, respectively, from the RMC model (blue lines) for vitreous B_2O_3, in comparison with the experimental total structure factors (red lines).

of 35 Å^{-1}, although the oscillations in $S^N(Q)$ are at a considerably higher Q (> 40 Å^{-1}). There is a large discrepancy around 3 - 4 Å^{-1}, because of the difference in the intrinsic coherent scattering cross sections. The results of the RMC simulation are plotted as blue lines in Fig. 1 for comparison. Excellent agreement is obtained for both the structure factors, apart from minor deviation in $S^X(Q)$. The RMC model should be able to provide relatively detailed structural information, because of the contrast between the $S^N(Q)$ and $S^X(Q)$. The partial structure factors, $S_{ij}(Q)$, are also shown in Fig. 1. The first sharp diffraction peak (FSDP) observed at Q ~ 1.6 Å^{-1} implies the presence of intermediate-range order due to the cages formed by the topological connection of BO_3 units in the network [4]. This interpretation is supported by the RMC results, as the FSDP is found to be a positive feature in all three partial structure factors at Q ~ 1.6 Å^{-1} in Fig. 1.

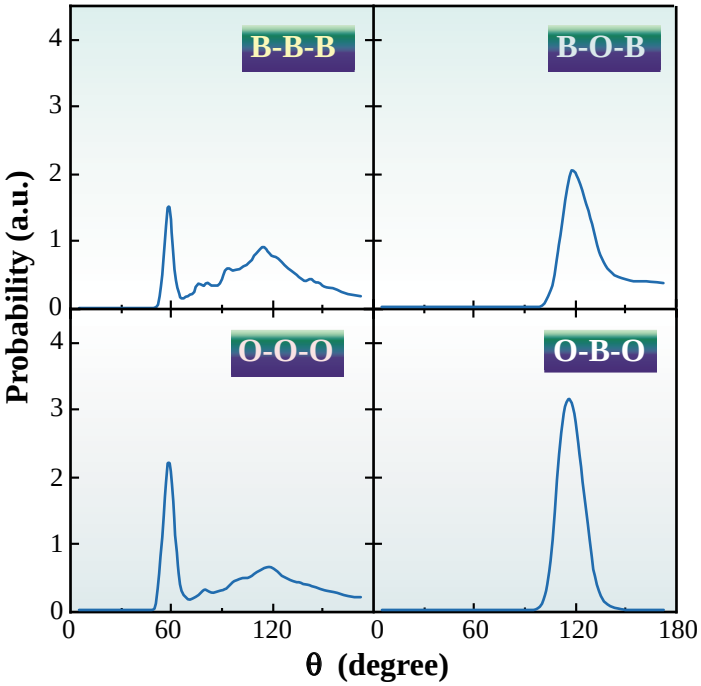

Fig. 2. Bond angle distributions for vitreous B_2O_3.

The bond angle distributions for B-B-B, O-O-O, B-O-B, and O-B-O are given in Fig. 2. The O-B-O and O-O-O distributions show a maximum close to the expected values for a regular BO_3 triangle of 120˚ and 60˚, respectively. The B-O-B angles are also narrowly distributed around a maximum near 120˚. The presence of a large number of planar boroxol rings (B_3O_6) is indicated by the small sharp peak at 60˚ in the B-B-B bond angle distribution. Recent neutron scattering studies of vitreous B_2O_3 indicate a model in which the majority of the boron atoms are in boroxol groups [3].

Figure 3 represents a 5 Å thick section of the RMC configuration, in which the presence of the boroxol rings is clearly visible. To estimate the fraction of the boroxol rings in vitreous B_2O_3 from the RMC configuration, the probability of finding a boron atom, which forms the B-B-B angle of 60˚ in the first coordination shell for B-B correlation, is calculated in Fig. 3. The value of the probability was found to be about 0.2, implying that the fraction of boroxol rings in vitreous B_2O_3 is not so large.

In order to obtain a more detailed understanding of the fraction of boroxol rings in the structure of vitreous B_2O_3, structural models of preserve-compacted B_2O_3 glasses are being generated from RMC fits to high-energy X-ray and neutron diffraction data.

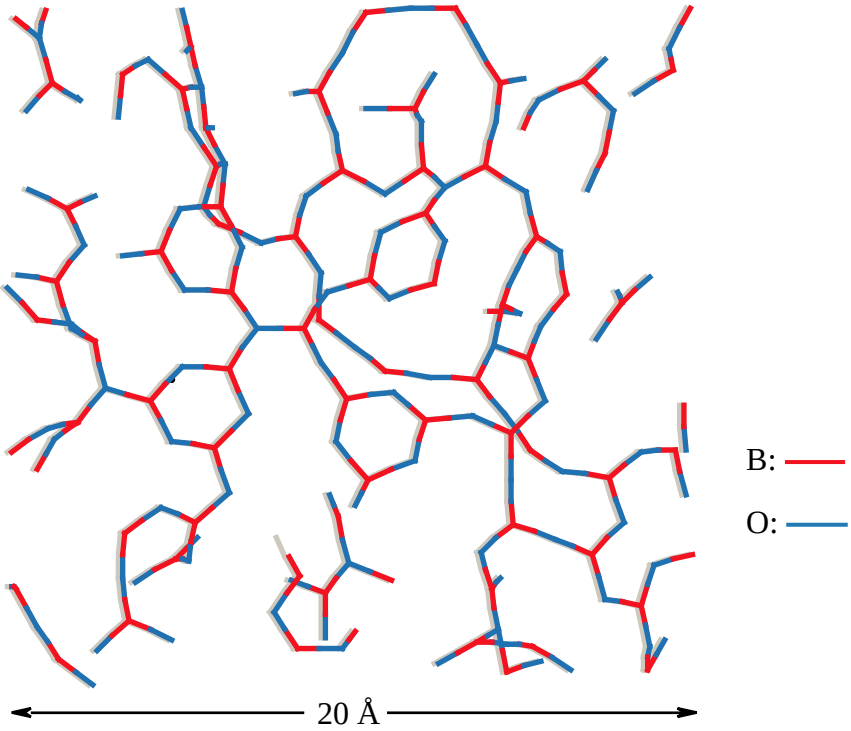

Fig. 3. A 5 Å thick slice of part of the largest RMC configuration for the borate (B-O) networks.

Kentaro Suzuya[a] and Shinji Kohara[b]

(a) SPring-8 / JAERI
(b) SPring-8 / JASRI

E-mail: suzuya@spring8.or.jp

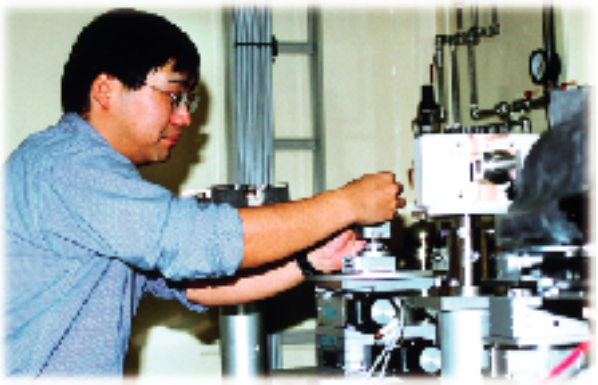

References

[1] K. Suzuya, S. Kohara, Y. Yoneda and N. Umesaki, Phys. Chem. Glasses **41** (2000) 282.
[2] R.L. McGreevy and L. Pusztai, Molec. Simul. **1** (1988) 359.
[3] A.C. Hannon *et al.*, J. Non-Cryst. Solids **177** (1994) 299.
[4] A.C. Wright *et al.*, J. Non-Cryst. Solids **129** (1991) 213.

VISCOSITY MEASUREMENTS OF ALBITE MELT UNDER HIGH-PRESSURE USING AN *IN SITU* X-RAY RADIOGRAPHY TECHNIQUE

An understanding of the viscosity of silicate melts under high-pressures is essential in contemplating the behavior of magma and volcanic eruptions. A variety of silicate melts have been investigated, leading to the conclusion that the viscosity of highly polymerized silicate melts decreases with increasing pressure, in sharp contrast to the behavior of normal liquids [1]. Thus far, the viscosity have been measured using a quench-falling sphere method, in which the terminal sinking velocity is determined by altering the quench rate [2-4]. In this method, however, the determination of the terminal velocity may involves uncertainties, due to the limitation of the sinking distance and the quench rate. The use of synchrotron radiation has enabled *in situ* observations of the falling sphere by implementing an X-ray radiography technique. This new method has many advantages over the traditional quench-falling sphere method [4,5]: (i) the precise terminal velocity of the falling sphere can be obtained, (ii) P-T condition is experimentally determined by combining *in situ* X-ray diffraction, and (iii) low-viscosity melts can be measured. Here, we report an *in situ* viscosity measurement under high pressure using an X-ray radiography falling sphere method. The first trial was performed on albite melt, which is one of the most important silicate melts.

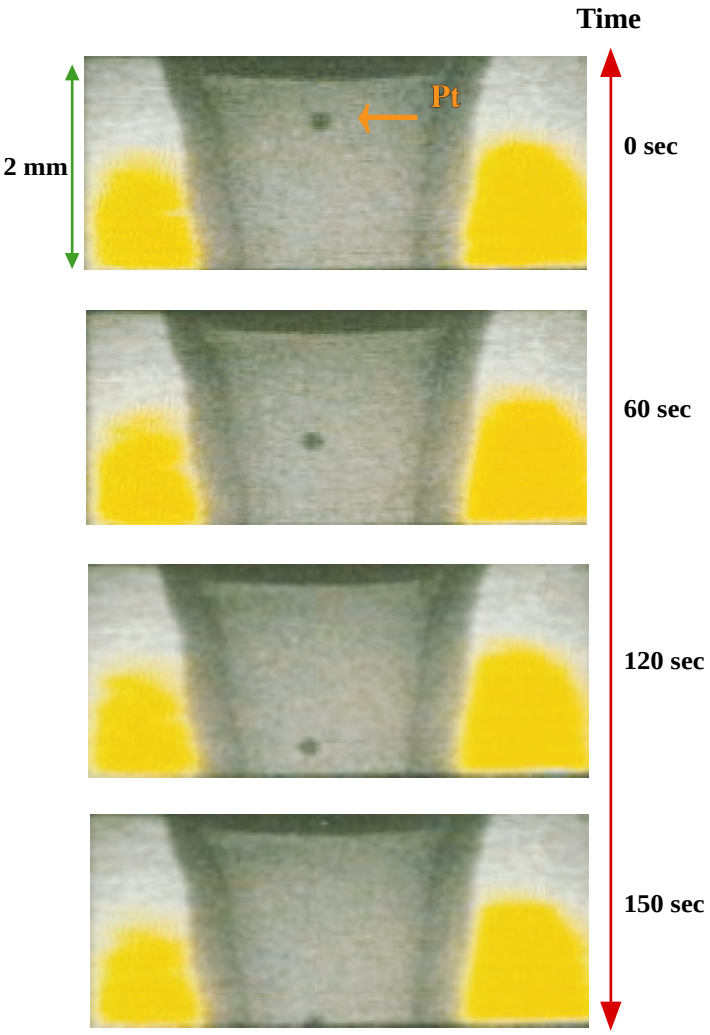

Fig. 1. The observed images detected by a high-speed CCD camera at 3.3 GPa and 1600 ℃. The measurable window was about 2 mm, because of the narrow anvil gap due to the compression. Each frame of these images was captured at intervals of 1/30 s.

We have set up an *in situ* viscosity measurement system combined with a multi-anvil apparatus at SPring-8 [6]. The system has been installed on a large volume multi-anvil apparatus (SPEED-1500) at beamline **BL04B1** [7]. Pressure is generated by a double-stage system with tungsten carbide cubes with a truncation edge length of 12 mm. The incident white X-ray from the bending magnet irradiates the sample cell through the anvil gap, and an image of the sample is projected on the fluorescence screen. This image is then magnified and detected by a high-speed CCD camera. For this experiments, a Pt sphere with a radius of 50 - 80 μm was embedded in the upper part of the albite sample. A fine powdered mixture of MgO and BN was filled surround the sample capsule as the inner pressure marker, and the pressure was calculated from the observed lattice constant of MgO. A thermocouple was placed on the top of the sample capsule. The sample was first compressed at the room temperature, followed by heating at a constant applied load. To avoid the differentiation effect or partial melting, the compressed sample was first annealed at 1000 °C, and then ramping was performed to reach the target temperature (1600 °C and 1700 °C). The heating rate was regulated to be about 200 °C/second. Once the target temperature was attained, the Pt sphere began to fall into the melt. The observed images from one of the series (3.3 GPa and 1600 °C) are shown in Fig. 1. The measurable window was about 2 mm, because of the narrow anvil gap due to compression. Each frame of these images was captured at intervals of 1/30 second. The high-speed and high-resolution CCD camera allowed for very good visual contrast between the Pt sphere

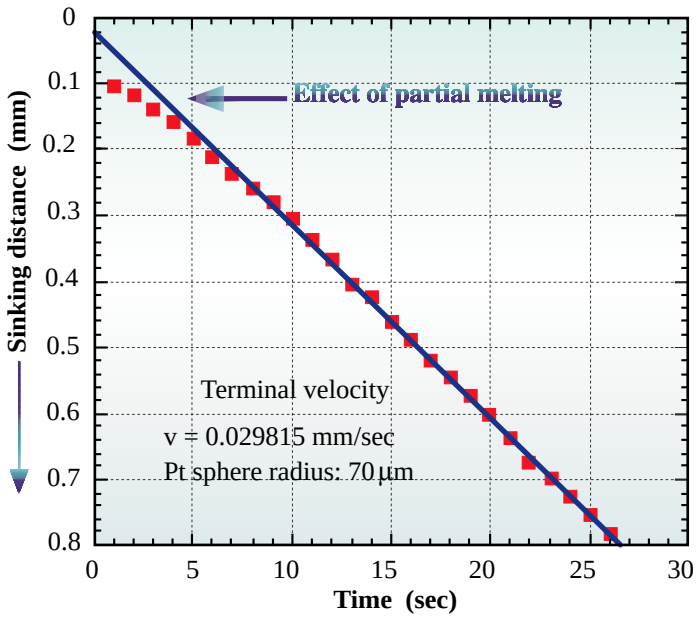

Fig. 2. Sinking distance of a Pt sphere in albite melt as a function of time (4 GPa, 1700 °C).

and albite melt possible in a short exposure time.

These measurements were carried out under the several P-T conditions up to 5.3 GPa at 1600 °C and 1700 °C. To determine the terminal velocity of the sinking sphere, we analyzed the images and obtained the geometrical center position of the Pt sphere from each captured frame. The settled distance (4 GPa and 1700 °C) is plotted in Fig. 2 as a function of time. At the moment the temperature reached 1700 °C, the Pt sphere (with a radius of 70 μm) began to sink slowly and sank at a constant velocity after 10 seconds. We used the linear part of the plot and determined the terminal velocity of the Pt sphere using a linear least square calculation. The viscosity was calculated from this velocity using Stokes' equation, including the Faxen correction for the wall effect [2,8].

The viscosities are summarized in Fig. 3, together with the data obtained by previous quench experiments. The error of our viscosity values is estimated within ±1.5 poise. As shown in this figure, our values clearly indicate the decrease of the viscosity with increasing pressure, which is significantly low (with no more than one order of poise) compared with those determined by the quench studies. Furthermore, at 1700 °C, the minimum viscosity is clearly seen to be around 4-5 GPa, which is consistent with the diffusivity results [9], therefore suggesting that some structural changes may occur at this pressure range.

Kenichi Funakoshi

SPring-8 / JASRI

E-mail: funakoshi@spring8.or.jp

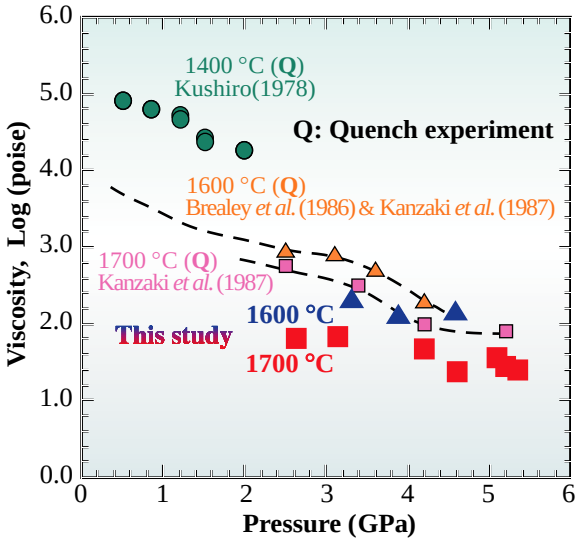

Fig. 3. Comparisons of the pressure dependence of the albite melt viscosity determined by in situ and quench experiments.

References

[1] C.M. Scarfe *et al.*, Magmatic process: Physicochemical Principles **1** (1987) 59, (Geochem. Soc. Univ. of Park, Pennsylvania.)

[2] I. Kushiro, Earth Planet. Sci. Lett. **41** (1978) 87.

[3] M. Brearley *et al.*, Geochim. Cosmochim. Acta **50** (1986) 2563.

[4] M. Kanzaki, Ph. D. Thesis, The University of Tokyo (1987).

[5] D.P. Dobson *et al.*, Earth Planet. Sci. Lett. **143** (1996) 207.

[6] K. Funakoshi, M. Kanzaki, A. Yasuda, A. Suzuki, H. Terasaki and S. Yamashita, Science and Technology of High Pressure, Proc. of AIRAPT-17, **2** (2000) 1023.

[7] W. Utsumi *et al.*, Rev. High Pressure Sci. Technol. **7** (1998) 1484.

[8] H.R. Shaw, J. Geophys. Res. **68** (1963) 6337.

[9] B.T. Poe *et al.*, Science **276** (1997) 1245.

XAFS

X-ray Absorption Fine Structure (XAFS) is now part of the everyday tool kit of many scientists, and no longer just a pioneering research tool for a select few. Thus, many material, important to both basic science and industry have been studied by using XAFS in order to clarify the relationship between their function and the atomic and/or electronic structure. This technique has also been utilized to discover new ways to develop more effective materials. Such an example is the XAFS analysis of three-way catalysts used to remove harmful compounds from automobile exhaust. A study of GeO_2 phase transitions under high pressure is another example and shows the possibility of XAFS studies under extreme conditions.

Development of the XAFS method is in progress, continuing to extend the fields to which XAFS can be applied. Such an example is the application of "capacitance XAFS" to Se doped AlGaAs containing defects. Capacitance XAFS spectra clearly show the temperature dependence, not seen in fluorescent XAFS. These results, indicating the site-selectivity of capacitance XAFS, suggest that XAFS will become an important tool for the structural study of material such as semiconductors. The second example is a total reflection XAFS on the surface of solutions. With the help of the high brilliance of SPring-8 and recently developed phase plate techniques, the packings of surfactant molecules are clarified. The third is a combination of fluorescent analysis and XAFS by using microbeam X-rays. The spatial distribution and the nickel species remained in a diamond crystal was clarified.

The high brilliance of SPring-8 will make the today's frontier techniques routine ones in the near future, allowing the control of polarization and microbeam X-rays, to open new application fields for XAFS analyses in SPring-8.

Masaharu Nomura

XAFS ANALYSIS OF THE LOCAL STRUCTURE OF CeO_2-ZrO_2 MIXED OXIDES

Oxygen storage/release capacity (OSC) is one of the important functions required of automobile three-way catalysts (TWCs) in order to efficiently remove harmful compounds such as hydrocarbons, CO and NOx in automotive exhaust gases [1]. In the TWCs, CeO_2 is widely used as a promoter due to its high OSC according to the reversible reaction ($2\ CeO_2 \leftrightarrow Ce_2O_3 + 1/2\ O_2$). However, the OSC performance and the durability of pure CeO_2 are still inadequate for practical use. Recently, our laboratory discovered that the addition of ZrO_2 to CeO_2 would enhance the OSC over that of pure CeO_2 as well as improve the thermal stability [2]. Thereafter, a considerable number of studies on the physical properties and structures of CeO_2-ZrO_2 have been made by many research groups (e.g. [3]). We have improved the OSC of CeO_2-ZrO_2 by modification of the preparation methods (Fig. 1). CZ55-1, CZ55-2 and CZ55-3 have identical composition ratio (Ce/Zr =1), yet they were prepared using different methodologies. Although the CeO_2-ZrO_2 has been widely utilized for commercial catalysts, the key factor in improving OSC is not clearly understood. The purpose of this study is to clarify the relationship between the OSC and the structure of CeO_2-ZrO_2. We investigated the local structure around both of Ce and Zr of these CeO_2-ZrO_2 by XAFS and clarified the cation-cation (cation = Ce, Zr) network at atomic level [4].

Although several groups have reported XAFS analyses on CeO_2-ZrO_2, all of them have utilized Ce L_3-edge (5.7 keV) XAFS [5] while there have been no studies employing Ce *K*-edge (40.5 keV) XAFS. The usable data region of Ce L_3-edge EXAFS is limited to ca. 3 - 9 $Å^{-1}$ in electron wave number (*k*) because of the presence of Ce L_2-edge (6.2 keV). Since Ce and Zr contributions to EXAFS signals are remarkable in the high-k part, the XAFS measurement of the Ce *K*-edge with a wide *k*-range is necessary in order to obtain the precise information

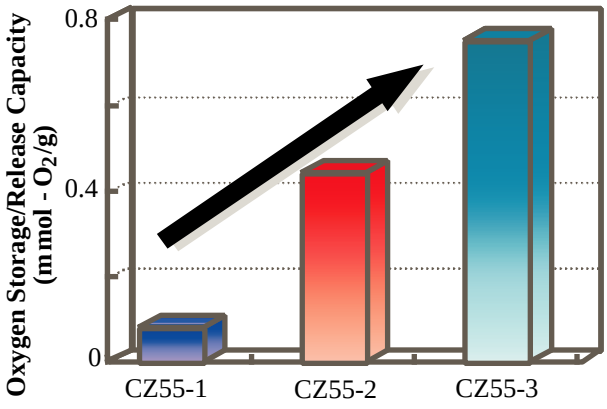

Fig. 1. Improvement of the oxygen storage/release capacity (OSC) of CeO_2-ZrO_2 with the same composition ratio (Ce/Zr =1). The OSC was estimated at 773 K. These samples were prepared by the following methods. CZ55-1 was prepared by the precipitation process using CeO_2 powder and zirconyl nitrate solution. CZ55-2 was prepared by the coprecipitation process using cerium nitrate and zirconyl nitrate solutions. CZ55-3 was synthesized by the heating CZ55-2 at 1473 K under reductive condition.

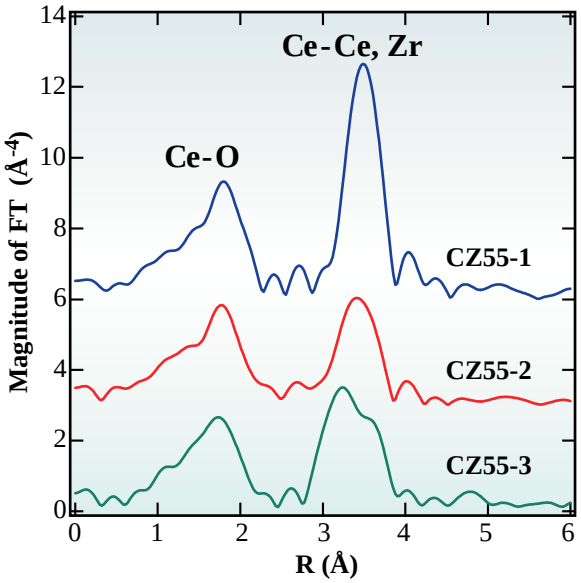

Fig. 2. Fourier-transformed $k^3\chi$ data from Ce K-edge EXAFS.

on Ce-Ce and Ce-Zr bonding. The high-energy X-ray at SPring-8 makes it possible to record XAFS spectra with an excellent signal-to-noise ratio at the *K*-edges of heavy elements [6].

Ce *K*-edge (40.5 keV) and Zr *K*-edge (18.0 keV) XAFS spectra were measured at **BL01B1** and **BL16B2**. Measurements were carried out using a Si (311) double crystal monochromator in a transmission mode at room temperature. The detailed procedure of data reduction have been described elsewhere [7]. Fourier transformations (FTs) were performed on Ce and Zr *K*-edges EXAFS spectra in about 3.0 - 17.0 $Å^{-1}$ region.

The FTs of the Ce *K*-edge EXAFS spectra are presented in Fig. 2. The position and amplitude of the Ce-O peaks for CZ55-1, CZ55-2 and CZ55-3 are slightly different from each other. The CZ55-2 and CZ55-3 exhibit lower Ce-cation (cation = Ce, Zr) peak intensities than that of CZ55-1. Additionally the Ce-cation peak of CZ55-3 appears to have split in two. The FTs of the Zr *K*-edge EXAFS spectra are shown in Fig. 3. Here, the shape of FTs for CZ55-1, CZ55-2 and CZ55-3 are obviously different. According to the results mentioned above, it is thus suggested that the OSC exhibits a significant correlation with the local structure around Ce and Zr. A quantitative curve-fitting analysis was performed for cation-cation shells in FTs to clarify this network. First, the Ce-cation shell for CZ55-1 was fitted with a single Ce-Ce shell, while the Zr-cation shell was also fitted with a single Zr-Zr shell. Thus, CZ55-1 consists of pure CeO_2 and ZrO_2 existing simultaneously (Fig. 4 (a)). Secondly, in the case of CZ55-2, not only Ce-Ce (Zr-Zr) but also Ce-Zr (Zr-Ce) shells were required to obtain an appropriate fit for the cation-cation shell at the Ce (Zr) *K*-edge. The Ce-cation shell was fitted with Ce-Ce (coordination number; CN = 8.0) and Ce-Zr (CN = 3.6) shells. The CN of the Ce-Ce shell is larger than that of the Ce-Zr shell. Likewise the CN of the Zr-Zr (CN = 3.0) was not equal to that of the Zr-Ce (CN = 4.0). This indicates that the CeO_2-ZrO_2 solid solution in CZ55-2 forms, but Ce rich domain and Zr rich one still remain

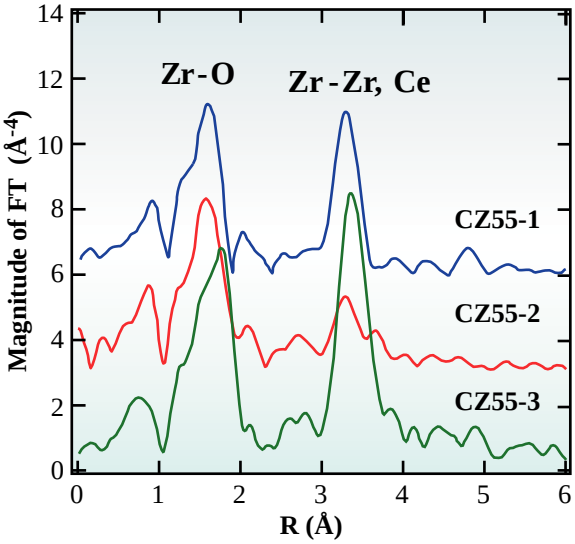

Fig. 3. Fourier-transformed $k^3\chi$ data from Zr K-edge EXAFS.

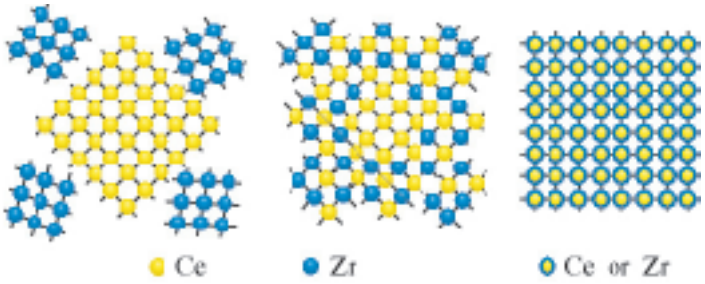

(a) CZ55-1 **(b) CZ55-2** **(c) CZ55-3**

Fig. 4. Model illustration of the cation-cation network for the CeO_2-ZrO_2 samples with the same chemical composition (Ce/Zr = 1). CZ55-1 consists of pure CeO_2 and ZrO_2. Ce rich domain and Zr rich one in CZ55-2 still remain. $Ce_{0.5}Zr_{0.5}O_2$ solid solution in CZ55-3 forms homogeneously at the atomic level.

(Fig. 4 (b)). Finally, the Ce-cation shell for CZ55-3 was fitted with Ce-Ce (CN = 6.0) and Ce-Zr (CN = 6.0) shells. The Zr-cation shell also was fitted with Zr-Zr (CN = 6.0) and Zr-Ce (CN = 6.0) shells. The evaluated values correspond with the Ce/Zr composition ratio = 1 of the sample. It is clear that the $Ce_{0.5}Zr_{0.5}O_2$ solid solution in CZ55-3 forms homogeneously at atomic level (Fig. 4 (c)). We conclude from these results that the OSC increases with enhanced homogeneity of the CeO_2-ZrO_2 solid solution at the atomic level.

Thus the relationship between the OSC and the cation-cation network of CeO_2-ZrO_2 has been elucidated, however, the mechanism of the OSC improvement is not yet completely understood. We consider that the configuration of the oxygen around Zr and Ce is modified by enhancing the homogeneity of CeO_2-ZrO_2 solid solution at atomic level. This modification should generate additional active oxygen for the OSC improvement. In order to study this possibility we plan to investigate the oxygen storage/release behavior of homogeneous CeO_2-ZrO_2 solid solution by XAFS and clarify the configuration of oxygen.

Through this research, we have determined an important rule that catalyst design at the atomic level is necessary in order to develop high performance catalysts of practical use.

Yasutaka Nagai[a], Takashi Yamamoto[b] and Tsunehiro Tanaka [b]

(a) Toyota Central R&D Labs., Inc.
(b) Kyoto University

E-mail: e1062@mosk.tytlabs.co.jp

References

[1] S. Matsumoto, Toyota Tec. Rev. **44** (1994) 10.
[2] M. Ozawa *et al.*, J. Alloys Comp. **193** (1993) 73.
[3] T. Omata *et al.*, J. Solid State Chem. **147** (1999) 573.
[4] Y. Nagai, T. Yamamoto, T. Tanaka, S. Yoshida, T. Nonaka, T. Okamoto, A. Suda and M. Sugiura, J. Synchrotron Rad. **8** (2001) 616.
[5] G. Vlaic *et al.*, J. Catal. **168** (1997) 386.
[6] T. Uruga *et al.*, J. Synchrotron Rad. **6** (1999) 143.
[7] T. Tanaka *et al.*, J. Chem. Soc., Farad. Trans. **84** (1988) 2987.

XAFS STUDY OF GeO_2 UNDER PRESSURE

When quartz-type crystalline GeO_2 (q-GeO_2) is compressed to pressures of 10 GPa at temperatures capable of inhibiting the crystallization of thermodynamically stable high-pressure phases, a pressure-induced phase transition occurs altering the coordination number (CN) of Ge from 4 to 6 [1]. Some groups have reported the high-pressure phase to be amorphous, while others insist the phase is crystalline in nature [2]. The sixfold coordination of Ge is either partly [1] or completely [2] preserved after the release of pressure. Pressure-induced CN changes have also been observed for vitreous GeO_2 at 6 - 10 GPa, although these changes are reversible [1]. Alkali germanate glasses, prepared under ambient conditions, contain a maximum of 20% of the sixfold coordinated Ge, throughout a composition range from 10 to 30 mol% alkali oxide. This phenomenon is known as germanate anomaly [3] .

We have compressed quartz-type crystalline GeO_2 (q-GeO_2) and vitreous Li_2O-$4GeO_2$ (g-GeO_2), at room temperature to pressures up to 14 GPa to observe local structural changes by *in-situ* XAFS; this method allowed the investigation of the nature of the pressure-induced transition [4].

q-GeO_2 and g-GeO_2 were well-ground, mixed with amorphous boron, and placed in a high-pressure cell made of boron and epoxy resin. Au foil, serving as a pressure marker, was separately charged in the cell. A cubic-type multi-anvil press (SMAP 180), installed on the **BL14B1** bending magnet beamline, was used for compression. The X-ray beam, monochromatized by Si (111) reflection, was focused vertically by two mirrors. The incident X-ray beam was directed into the sample using vertical (0.2 mm) and horizontal (0.3 mm) slits. We then measured the X-ray absorption spectra near the Ge *K*-edge and the Au *L*-edge. The pressure generated was calculated from the equation of state of Au using Au-Au distances determined by Au *L*-edge EXAFS measurements. Measurements were made at room temperature. EXAFS data analysis is described in detail elsewhere [5].

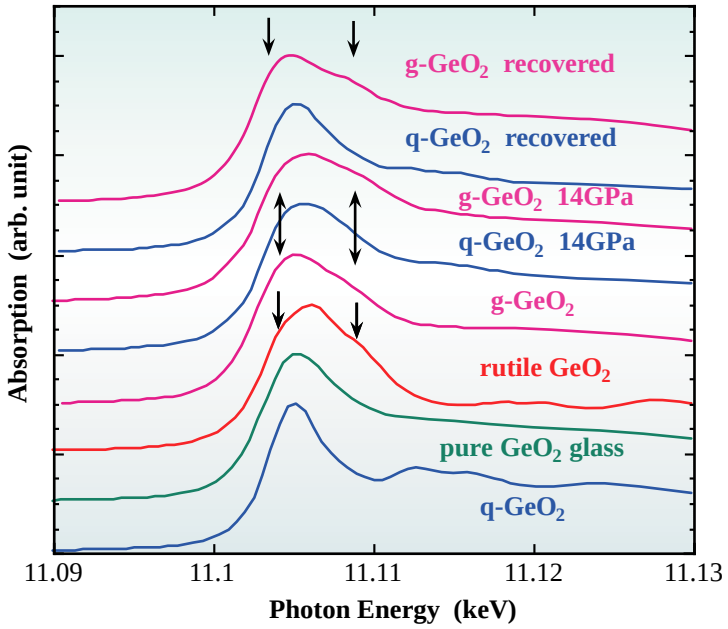

Fig. 1. Experimental Ge K-edge XANES spectra of various GeO_2 samples. Arrows indicate the two shoulders characteristic of six-fold coordination of Ge.

To distinguish between fourfold and sixfold coordination, we recorded the XANES spectra of q-GeO_2 and g-GeO_2 under various conditions (Fig. 1). The XANES spectra display two discernible shoulders, characteristic of a sixfold coordination of Ge. At 14 GPa, q-GeO_2 demonstrates the shoulders. These features, however, disappear when q-GeO_2 is restored to ambient pressure, indicating an almost complete reverse transition in the q-GeO_2 sample. The spectra of starting g-GeO_2 glass already

displays slight traces of the shoulders, demonstrating the germanate anomaly. At 14 GPa, the spectra possess the characteristics of sixfold Ge coordination. The spectra of g-GeO_2 allowed to recover from high pressure are similar to those of the starting glass.

Compression and decompression greatly varies the Ge-O distances of both q-GeO_2 and g-GeO_2 (Fig. 2). Throughout the compression of q-GeO_2 below 8 GPa, the Ge-O distance gradually shortens, indicating the conventional compression pattern of quartz-type crystalline structures. An abrupt increase in Ge-O distance, however, occurs between 8 and 12 GPa, corresponding to the CN change. The extrapolation of Ge-O distances at pressures ranging from 12 or 14 GPa to ambient pressure correlates well with a rutile structure; therefore, the CN change

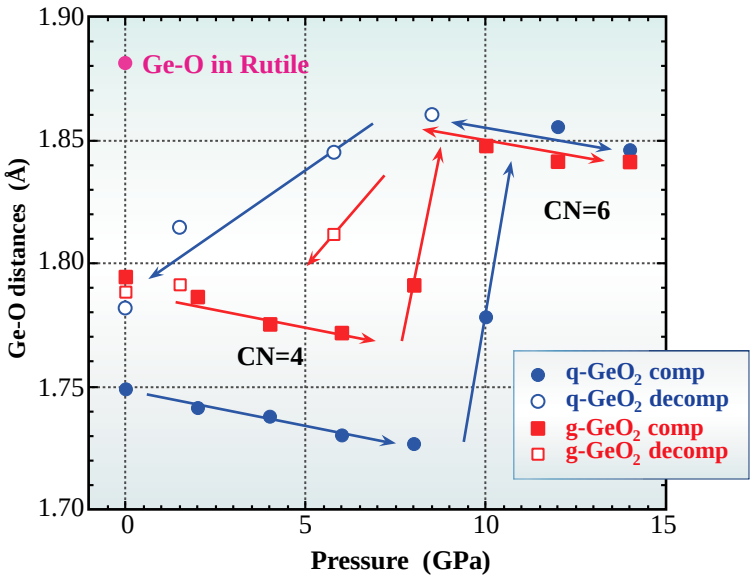

Fig. 2. Variation of Ge-O distance of quartz-type q-GeO_2 and g-GeO_2 by compression (solid symbols) and decompression (open symbols). Circles signify q-GeO_2 while the squares indicate g-GeO_2. Solid lines provide a guide for the eye only.

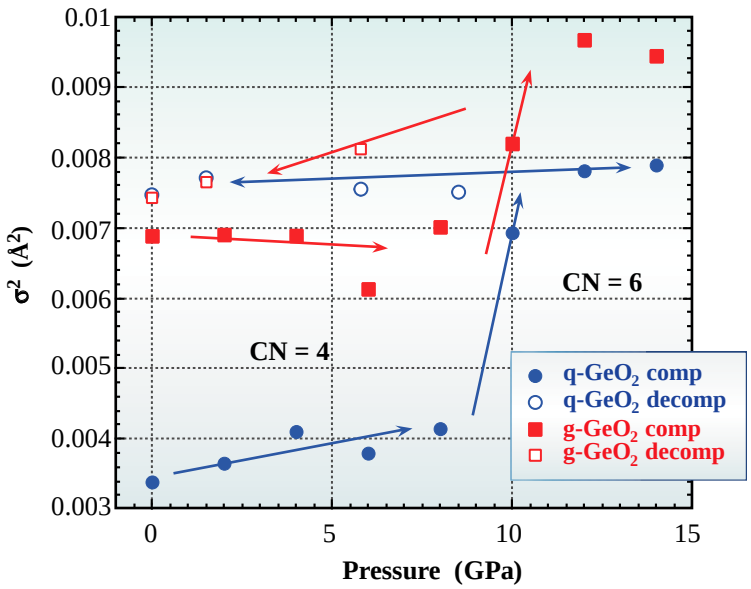

Fig. 3. Variation of Debye-Waller factors, σ^2 of q-GeO_2 and g-GeO_2, by compression (solid symbols) and decompression (open symbols). Circles indicate q-GeO_2 and the squares designate g-GeO_2. Solid lines provide a guide for the eye only.

is completed below 12 GPa. Decompression facilitates a reverse transition, occuring gradually below 6 GPa. Upon complete release of pressure, the Ge-O distance is 1.78 Å, slightly larger than that in the initial q-GeO_2 and similar to that of g-GeO_2. The CN change of g-GeO_2 begins above 6 GPa to finish below 10 GPa, a lower pressure than necessary for q-GeO_2 by 2 GPa. The reversal change of CN occurs below 10 GPa for g-GeO_2, with a smaller hysteresis than q-GeO_2. At the complete release of pressure, the Ge-O distance is 1.79 Å the same as observed for the untreated g-GeO_2. As the g-GeO_2 originally includes a fraction of the Ge possessing a sixfold coordination, we expected a continuous

increase in CN with increasing compression. The Ge-O bond, however, gradually shortens below 6 GPa and elongates within a narrow pressure range only. These results indicate that the compression of the GeO_4 tetrahedron is energetically less costly than CN change, even under circumstances where the GeO_6 octahedron nuclei preexists.

The variation of σ^2 of q-GeO_2 and g-GeO_2 reveals that the initial value of g-GeO_2 is larger than that of q-GeO_2, reflecting the glassy state (Fig. 3). Compression results in the increase of σ^2 for both q- and g-GeO_2, corresponding to the changes in CN [5]. Decompression leaves the once-increased σ^2 of q-GeO_2 at similar values. The reversal change in g-GeO_2 occurs below 10 GPa with hysteresis. Several arguments question whether the high pressure phase is amorphous or crystalline. Present σ^2 of 0.008 Å^2 for q-GeO_2 at pressures greater than 10 GPa is considerably larger than the value of 0.004 Å^2 for rutile-type GeO_2 [5]; it is smaller, however, than that of g-GeO_2 in the same pressure range. This result suggests that the local structure around Ge atoms within the high pressure phase is more random than the rutile phase and less random than g-GeO_2 possessing sixfold coordination. As the CN change occurs at low temperatures during which the thermally activated diffusion process is restrained, the transition likely occurs by a martensitic mechanism. Consequently, we propose that the high pressure phase consists of a fine crystalline domain possessing many defects. The relatively large value of σ^2 in this phase indicates poor crystallization, resulting from defects introduced by a martensitic transition.

Osamu Ohtaka

Osaka University

E-mail: ohtaka@ess.sci.osaka-u.ac.jp

References

[1] J.P. Itie *et al.* , Phys. Rev. Lett. **63** (1989) 398; D. J. Durben and G.H. Wolf, Phys. Rev. B **43** [1991) 2355.

[2] J. Haines *et al.*, Phys. Rev. B **61** (2000) 8701.

[3] S. Sakka and K. Kamiya, J. Non-Crystalline Solids **49** (1982) 103.

[4] O. Ohtaka, A. Yoshiasa, H. Fukui, K. Murai, M. Okube, Y. Katayama, W. Utsumi and Y. Nishihata, J. Synchrotron Rad. **8** (2001) 791.

[5] A. Yoshiasa *et al.*, J. Synchrotron Rad. **6** (1999) 1051.

PHOTOEMISSION PROCESS OF A LOCALIZED ELECTRON IN CARRIER TRAP AND ITS APPLICATION TO SITE-SELECTIVE X-RAY ABSORPTION FINE STRUCTURE MEASUREMENT

X-ray absorption fine structure (XAFS) measurement is an important experimental technique, which uses synchrotron radiation (SR) for local structure analyses. In XAFS analysis, *microscopic* information, such as bond lengths and the coordination number, is derived from the *macroscopic* absorption property, and thus structural homogeneity of the sample is necessary. When the sample is heterogeneous with various local structures, the XAFS spectrum provides only the average information of these local structures. A meaningful analysis using this average information is impossible, except in the rare case in which the spectrum can be deconvoluted into a few spectra of some well-known structures. A heterogeneous system is not only common but also is of interest in current material science. For instance, the defects in a single crystal and heterointerfaces fabricated by epitaxial growth have singular structures in the crystal. The assumption of sample homogeneity restricts the applicability of XAFS measurement.

Recently, we proposed a new XAFS method, capacitance XAFS measurement [1]. In this method, since the amount of X-ray absorption is evaluated by a capacitance change due to X-ray induced photoemission of a localized electron, a site-selective XAFS analysis of the specific atoms with the localized electron may be achieved. It is well known that the defects and dangling bonds at the heterointerface in semiconductors localize electrons owing to their characteristics as trap centers, suggesting that the *microscopic* absorption property of these singular atoms can be selectively analyzed by capacitance XAFS measurement.

In this research, the X-ray induced photoemission property of the localized electron and the site-selectivity of capacitance XAFS measurement based on this process are discussed.

The detailed concept and experimental apparatus of capacitance XAFS method were described in previous papers [1,2]. In our experiments performed at the High Brilliance XAFS beamline **BL10XU**, the capacitance involved in the Schottky diode of a compound semiconductor, Se-doped AlGaAs, was measured under SR irradiation. It is well know that a deep level of the electron trap, the DX center, is formed in this sample due to the intrinsic property of the donor impurity in zinc-blende semiconductors.

Figure 1 shows the capacitance XAFS spectra at the Ga *K*-edge (10.375 keV). The sample

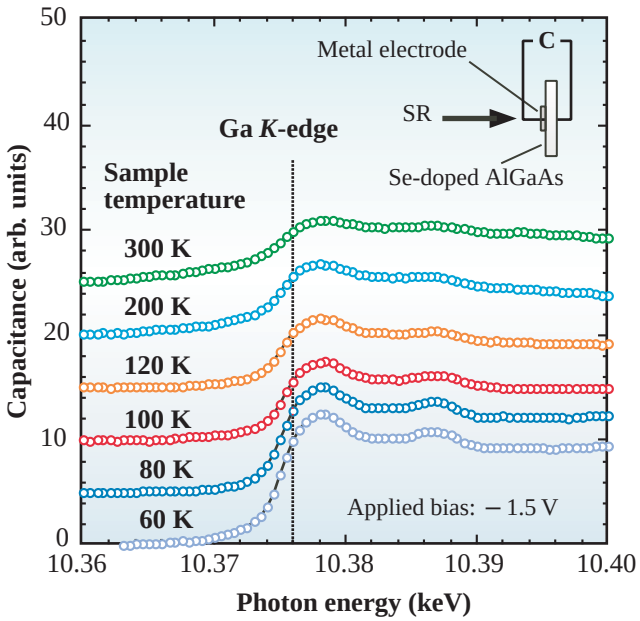

Fig. 1. Temperature dependence of capacitance XAFS at the Ga K-edge.

temperature was varied from 60 K to 300 K. As shown in this figure, the edge jump decreases with increasing substrate temperature, and finally, it almost disappears at room temperature. This tendency is in contrast to that of the conventional XAFS method. In conventional fluorescence XAFS method, since the X-ray penetration depth and escape depth of the fluorescence, which are independent of the sample temperature, determine the number of detectable atoms, no temperature dependence of the edge-jump is observed. On the other hand, the valence electronic states are easily modified by thermal energy of the order of ~ meV. The temperature dependence of edge-jump in Fig. 1 provides evidence that the valence electron is related to the signal-detection process in capacitance XAFS measurement. In fact, the activation energy of the photoemission process of trapped electron is estimated to be 7.33 meV from a fitted result of the temperature dependence based on the Arrhenius' equation as shown in Fig. 2.

Moreover, a capacitance-voltage (C-V) analysis which provides the carrier concentration in the semiconductor, indicates that the activation energy of the extra donor generation process under SR is evaluated to be 7.68 meV [2]. Almost the same activation energies for the photoemission in capacitance XAFS measurement (7.33 meV) and this extra donor generation indicate that the signal amplitude of capacitance XAFS measurement is determined by the X-ray induced photoemission of the localized electron to conduction band in the semiconductor. This is consistent with the concept of capacitance XAFS method.

Figure 3 shows a possible photoemission dynamics based on these finding. Only the energy diagram around the Fermi level, E_f, is illustrated in this figure. The Fig. 3 (a) indicates a steady state before the X-ray irradiation. The localized electrons occupy the trap level in the band gap of the semiconductor. When the X-ray is absorbed at the defect atom, (b) excitation of the localized

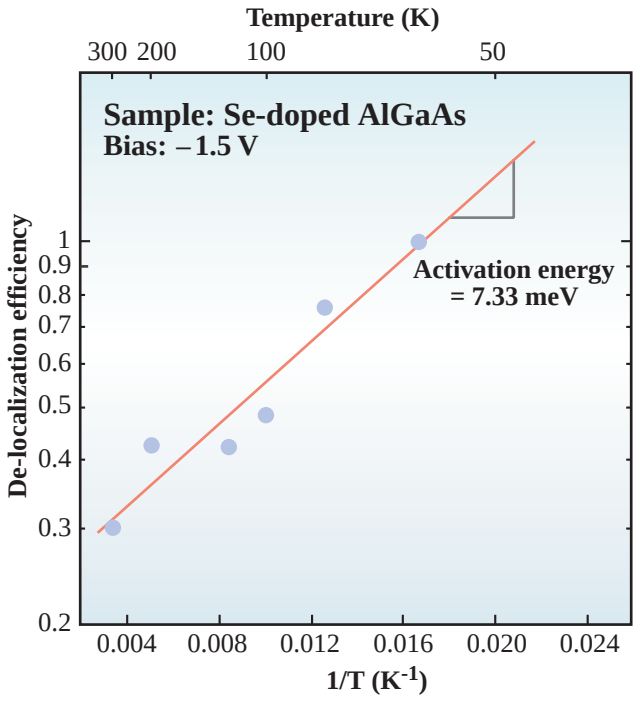

Fig. 2. Arrhenius' plot estimation of thermal activation energy of the photoemission process in the capacitance XAFS method.

electrons into a conduction band is expected (Fig.3 (b)). The de-localized electrons are swept out from the depletion layer so that the positively charged trap center pushes down the E_f to $E_f - \Delta E$. The Fermi level of the semiconductor should be equal to that of the metal electrode used for the capacitance formation. Consequently, (c) the energy level of the conduction band is increased by ΔE (Fig.3 (c)). The level modification reduces the thickness of the depletion layer without the localized electron, resulting in the capacitance increment by the X-ray absorption. This dynamics indicates the *microscopic* X-ray absorption at the defect, not the *macroscopic* absorption at bulk, is selectively obtained by capacitance XAFS method. The details of structural analysis using XAFS method are described in SPring-8 Research Frontiers 1997/1998 [3].

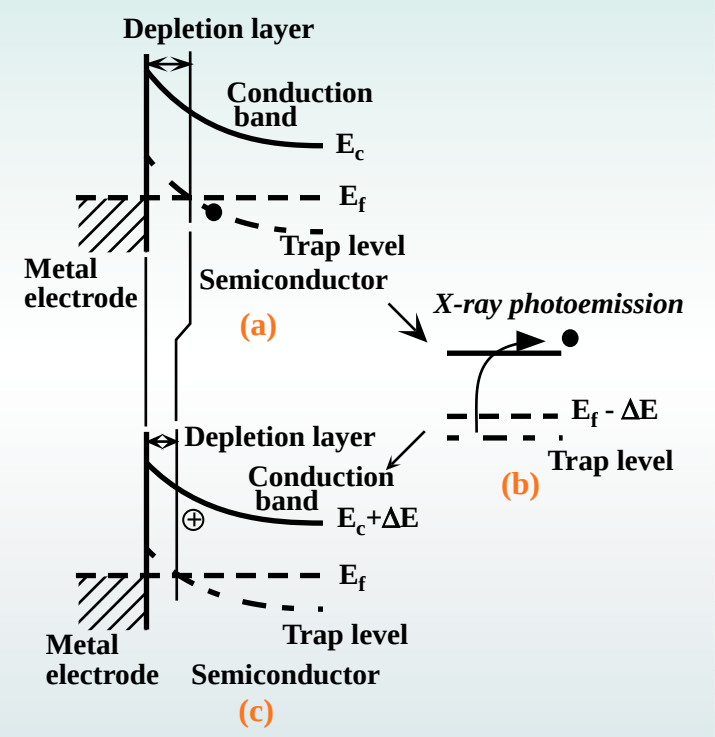

Fig. 3. Possible photoemission dynamics in capacitance XAFS measurement.

Masashi Ishii

SPring-8 / JASRI

E-mail: ishiim@spring8.or.jp

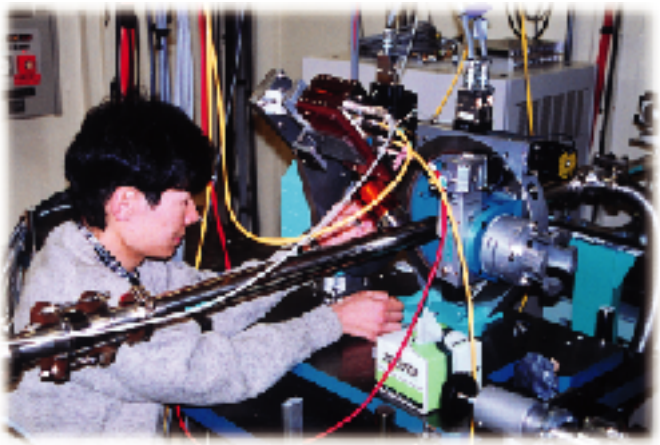

References

[1] M. Ishii *et al.*, Appl. Phys. Lett. **74** (1999) 2672.
[2] M. Ishii, Y. Yoshino, K. Takarabe and O. Shimomura, J. Appl. Phys. **88** (2000) 3962.
[3] M. Ishii, SPring-8 Research Frontiers 1997/1998, p.94.

POLARIZATION XAFS STUDY OF IONS AT SOLUTION SURFACE

Soap, when dissolved in water, easily forms bubbles even at millimolar concentrations. Such bubbles surround the included air with a monolayer of soap molecules, as seen for the large fatty acid sodium salt illustrated in Fig. 1. Soap, a typical surfactant, has a strong tendency to come to the surface of an aqueous solution, resulting in a highly concentrated surface density. Surfactant molecules normally possess a long hydrocarbon chain with an ionic head. The hydrophobicity of the long hydrocarbon makes the surfactant insoluble in water, sticking to oily substances instead; the hydrophilicity of the ionic group forces the surfactant molecule adhere tightly to the surface of the aqueous solution.

The molecular packing of the surfactant at the solution surface depends on the identity and concentration of the counter ion; for fatty acid soaps, use of metal ions, such as calcium(II), cadmium(II) or zinc(II), as the counter ion assist in the formation of a solid monomolecular film (the Langmuir monolayer) at the solution surface. Although the structure varies between the ions, well organized structures including both the fatty acid and the cations must form at the solution surface. As information concerning these surface structures are interesting to colloid and solution chemists in addition to being important in the detergent industry, a large number of thermodynamic and spectroscopic studies have attempted to elucidate this structure. Such studies have utilized laser driven sum-frequency-generation and second-harmonic-generation spectroscopy to address this question, since these techniques are strictly surface sensitive. None of these attempts, however, have yet been able to give the coordination structures of the metal ions at the Langmuir monolayer. Unlike the available methods to study solid surfaces, few techniques exist that are suitable for the study of liquid surfaces.

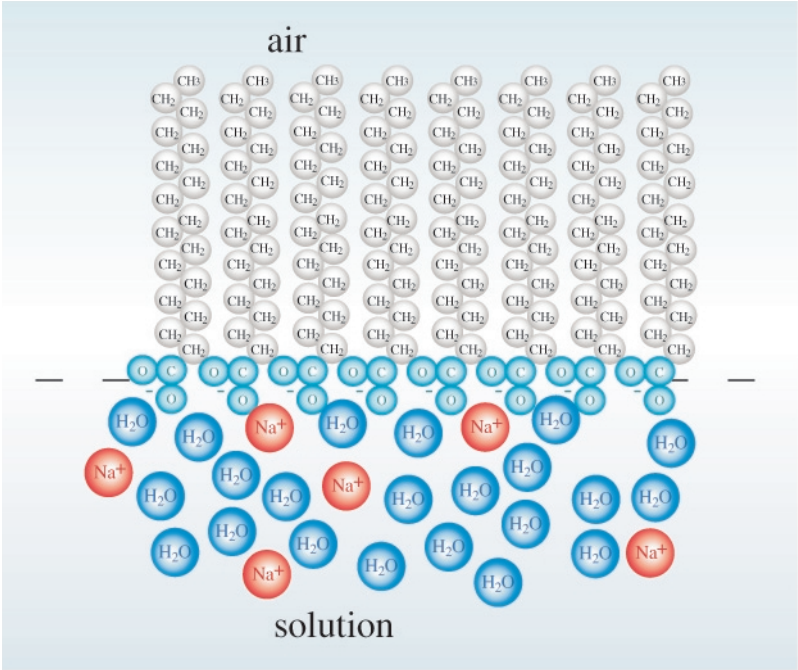

Fig. 1. A schematic model for stearate monolayer structure at the aqueous solution surface.

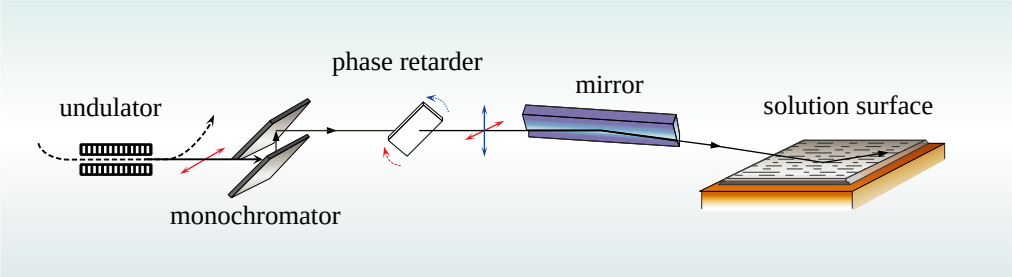

Fig. 2. Total-reflection polarization-XAFS system for the study of solution surfaces at beamline BL39XU.

We are developing a method of X-ray absorption spectroscopy to allow the study of solution surfaces. A monochromatized X-ray beam is introduced onto the solution surface at a small glancing incidence angle to allow the detection of surface elements only, under total-reflection conditions. A high brilliance and small divergence X-ray beam deriving from the undulator at beamline **BL39XU** is most appropriate for this application.

In addition, the solution surface is a two-dimensional reaction field; the geometry of ions at the surface may preferentially orient with respect to the liquid surface. To describe the coordination structures of ions at the solution surface by the XAFS method, we require linearly polarized X-rays both parallel and normal to the surface. As the liquid surface cannot be turned upright, a beamline capable of supplying X-rays polarized both horizontally and vertically to the surface is essential for these measurements.

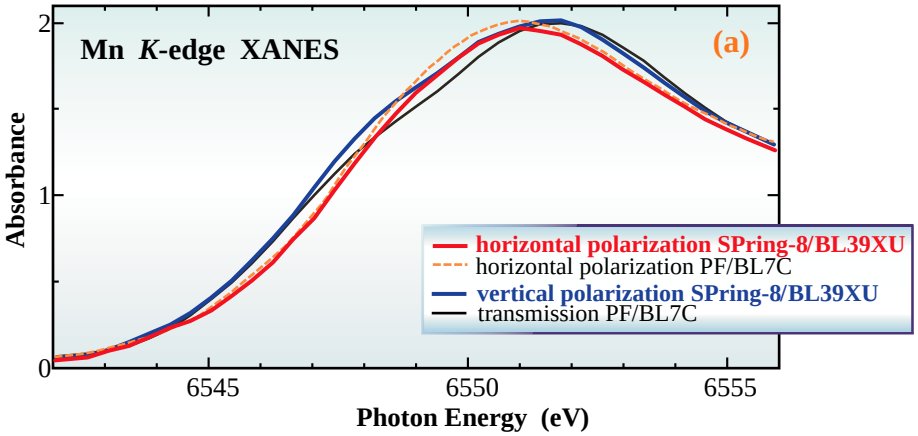

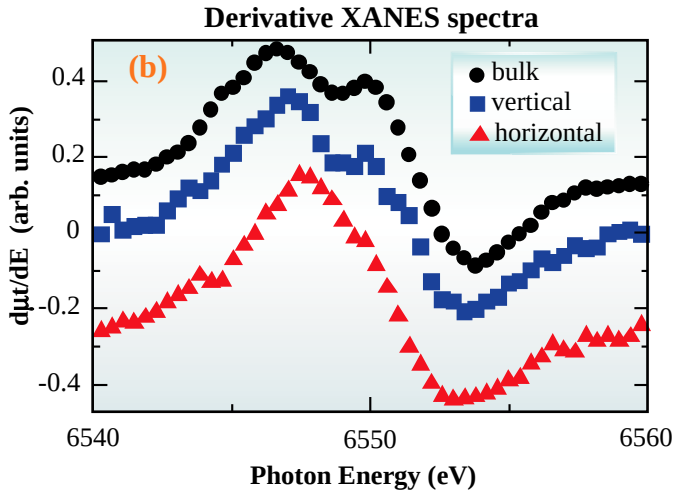

Fig. 3. ***(a)*** *Mn K-edge XANES spectra for the Mn(II)-stearate monolayer at the aqueous solution surface.*
(b) *The first derivative XANES spectra for Mn K-edge.*

The phase retarder at BL39XU, originally installed for X-ray magnetic circular dichroism (XMCD) studies, is also an ideal component for the present study, capable of quickly converting the horizontally polarized X-rays into vertically polarized beams.

The X-rays from the monochromator pass through a diamond crystal phase retarder to be reflected by a silicon mirror (Fig. 2). The mirror is tilted at an angle designed to deflect the beam horizontally at an angle large enough to remove higher harmonics from the double-crystal monochromator; the beam is also deflected vertically at 1 mrad, the total-reflection incidence angle at the solution surface.

The solution cell, described in a previous report [1], contains a sample solution with 1 mmol/dm^3 Mn(II) ion. The solution surface is covered by a monolayer of stearic acid ($CH_3(CH_2)_{16}COOH$). We obtained the Mn *K*-edge X-ray absorption spectra using two linearly polarized X-rays (Fig. 3(a)). The vertical polarization spectrum possesses a shoulder at the edge; the horizontal spectrum does not, clearly demonstrated in the first derivative spectra (Fig. 3(b)). In our evaluation of the transmission spectra for bulk Mn(II) solutions, the shoulder

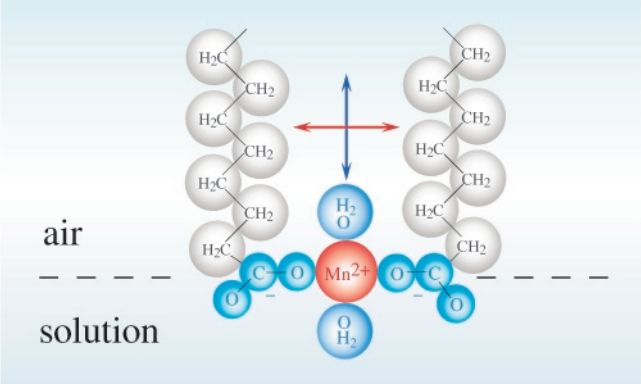

Fig. 4. The proposed coordination structure for the Mn(II)-stearate monolayer at the aqueous solution surface. The polarization directions correspond to the spectra in Fig. 3, respectively.

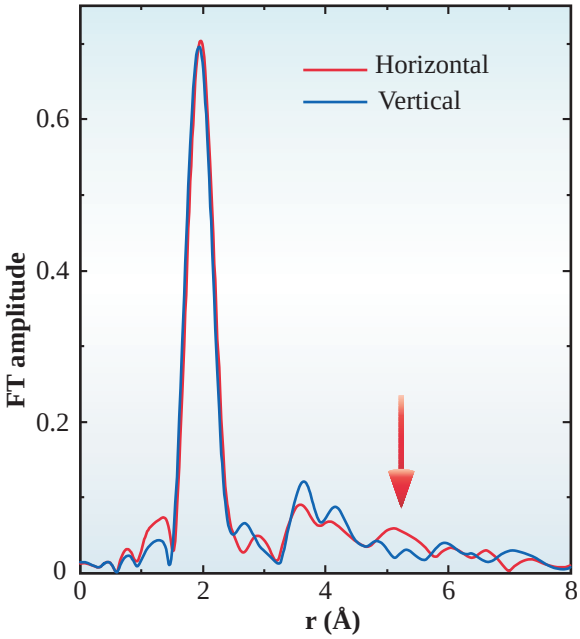

Fig. 5. The Fourier-transformed EXAFS spectra for the Zn(II)-stearate monolayer at the aqueous solution surface.

structure or double peaks in the first derivative are characteristic of such bulk solutions. As the coordination structure of the Mn(II) ion in the bulk solution is octahedral containing six coordinating water molecules, the coordination structure on the vertical axis must be similar to that of bulk one. Structures in the horizontal plane must differ from the bulk structure. We present a candidate model for such a structure (Fig. 4).

For a Zn(II)-containing solution covered by a monolayer of stearic acid, the two polarization XANES spectra at Zn *K*-edge are similar, yet differ from the bulk one. The spectra clearly indicate that Zn(II) adopts tetrahedral symmetry at the Langmuir monolayer, in contrast to the octahedral structure observed in the bulk [2]. Careful inspection of the EXAFS spectra indicated that a difference between two polarization EXAFS at around 5 Å (Fig. 5); a small peak appears in the horizontal spectrum only. This peak may correspond to the Zn-Zn distance in the

Langmuir monolayer. A distance of approximately 5 Å correlates with that found for zinc acetate in an unhydrated crystal, a structure adopting a layered conformation. Each layer accommodates zinc ions on the same plane, connected by acetate bridges of a 4.8 Å distance. We outline our proposed model for the Zn-stearate Langmuir monolayer in Fig. 6.

This new spectroscopic method is useful for the analysis of liquid surfaces, providing information previously thought to be impossible.

Iwao Watanabe

Osaka University

E-mail: watanabe@chem.sci.osaka-u.ac.jp

References

[1] I. Watanabe, H. Tanida, S. Kawauchi, M. Harada and M. Nomura, Rev. Sci. Instrum. **68** (1997) 3307.

[2] I. Watanabe *et al.*, J. Am. Chem. Soc. **119** (1997) 12018.

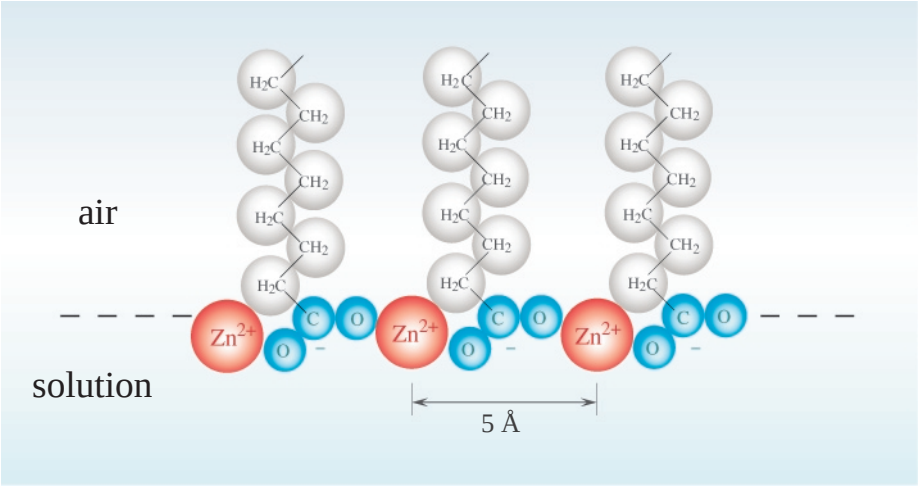

Fig. 6. The proposed coordination structure for the Zn(II)-stearate monolayer at the aqueous solution surface.

MICRO XAFS CHARACTERIZATION OF TRACE NICKEL DISSOLVED INTO SYNTHETIC DIAMONDS

Diamond is a unique substance possessing a high thermal conductivity, hardness and electric resistivity. The applications of diamond, valuable as hard materials, are expanding into electronics and optics. Diamond can be synthesized using either high pressure techniques or chemical vapor deposition (CVD) techniques. To produce a single large diamond crystal, however, crystallization should occur in a metallic solvent at a high temperature and high pressure. The most commonly used metallic solvents are Cr, Mn, Fe, Co, Ni, and Cu or a combination. Although many studies have examined the phase diagrams of Fe, Ni and Co with carbon at high pressures, the mechanism of diamond synthesis and the nature of the resulting synthesized diamond remain unclear.

We utilized synchrotron radiation-excited X-ray fluorescence (XRF) analysis to analyze trace impurities in synthetic diamonds. XRF analysis is the most suitable of various analytical methods to characterize metallic impurities due to the strong elemental selectivity, high sensitivity and large capacity for spatial resolution, as compared to optical absorption or electron spin resonance (ESR). To investigate the distribution of trace impurities in diamonds grown in a $Fe_{55}Ni_{29}Co_{16}$ solvent, we utilized an X-ray microprobe system at beamline **BL39XU** [1] with a spatial resolution of 10 μm. Figure 1 displays the Ni, Co and Fe XRF images and the transmitted X-ray image of the {110} diamond wafer of a 278 mm thickness. As previously reported [2], Ni and Co prefer to be dissolved into {111} growth sectors; the concentrations of these metals are below detection limits in {100} growth sectors. Fe cannot be detected in either the {111} or the {100} growth sectors. The Ni concentration is approximately 30 ppm. The Co concentration is an order of magnitude lower than that of Ni.

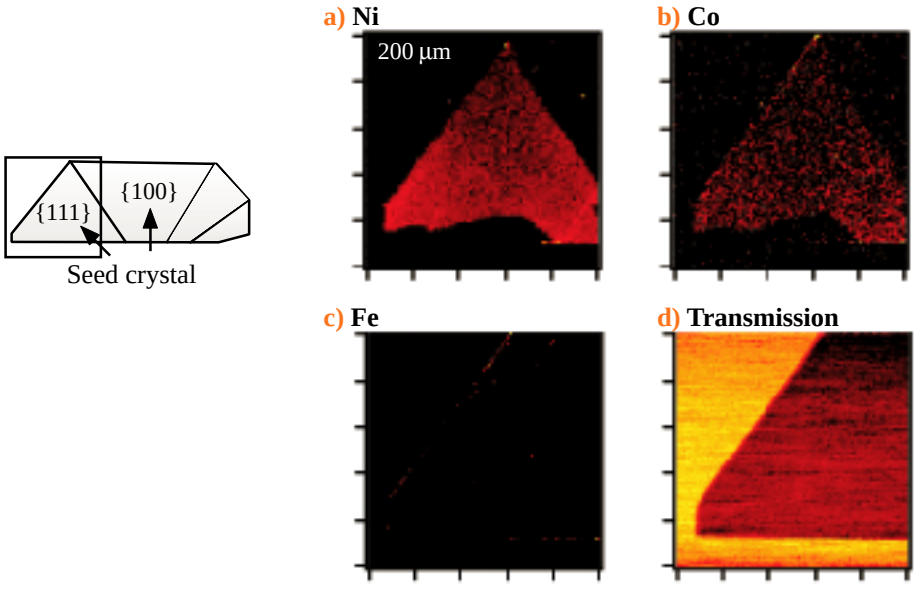

*Fig. 1. Schematic drawing and X-ray images of a synthetic diamond grown at high pressure and high temperature utilizing a $Fe_{55}Ni_{29}Co_{16}$ solvent. **a)** Ni, **b)** Co, **c)** Fe and **d)** transmission images.*

The combination of the brilliant undulator radiation from SPring-8 and the gap tuning method has made possible a discussion of the local structure of trace Ni and Co from X-ray absorption fine structure (XAFS) spectra. The near edge spectra of both Co and Ni display a characteristic pre-edge feature and these are completely different from the spectra of metallic Ni and Co which can be observed where inclusions exist [3]. Figure 2 shows the XAFS spectrum of Ni in the {111} growth sector. To obtain greater sensitivity, we utilized a beam size of 150 μm for these measurements. Utilizing this beam size and Ni concentration, only 4×10^{12} atoms of Ni in the diamond contributed to the XAFS spectrum. Figure 3 demonstrates the extracted EXAFS (Extended X-ray Absorption Fine Structure). Fourier transformation of the EXAFS oscillation possesses two peaks resulting from the dissolved Ni (Fig. 4). One peak, consistent with the model derived from the pre-edge peak, corresponds to Ni in the tetrahedral site of the diamond lattice. The other peak indicates the existence of Ni-Ni bond. This result suggests the presence of an extremely small metallic cluster of Ni within the diamond; further investigations are now in progress.

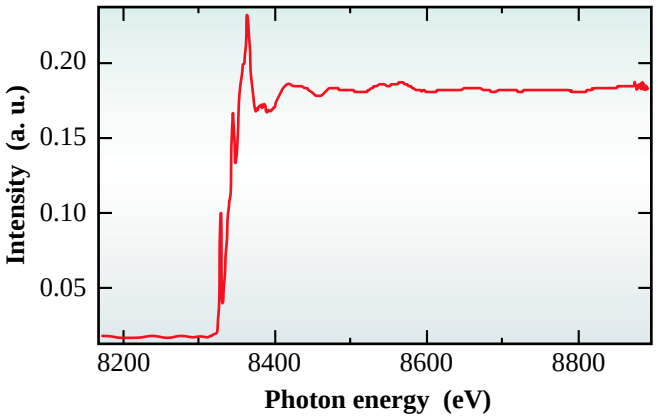

Fig. 2. Ni K XAFS spectrum obtained from dissolved Ni within the diamond using the XRF yield method. The Ni concentration is approximately 30 weight ppm (6 atomic ppm) in the {111} growth sector.

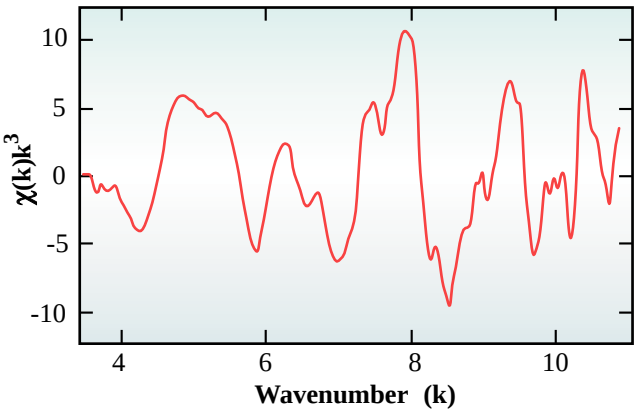

Fig. 3. EXAFS oscillations χ (k) of the dissolved Ni within the diamond.

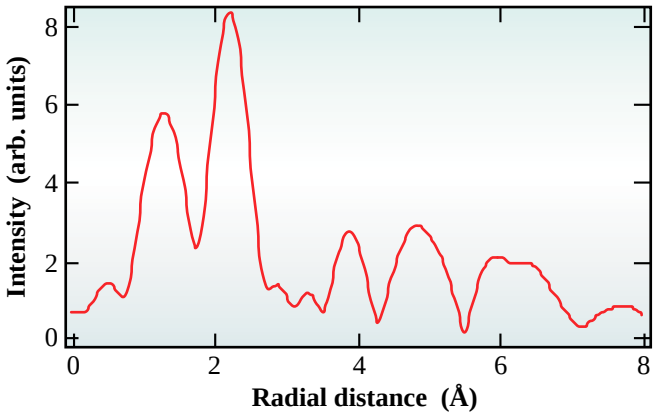

Fig. 4. Fourier transformation of EXAFS oscillations around Ni atoms within the diamond.

Shinjiro Hayakawa[a] and Masao Wakatsuki[b]

(a) Hiroshima University
(b) National Institute of Materials and Chemical Research

E-mail: hayakawa@hiroshiam-u.ac.jp

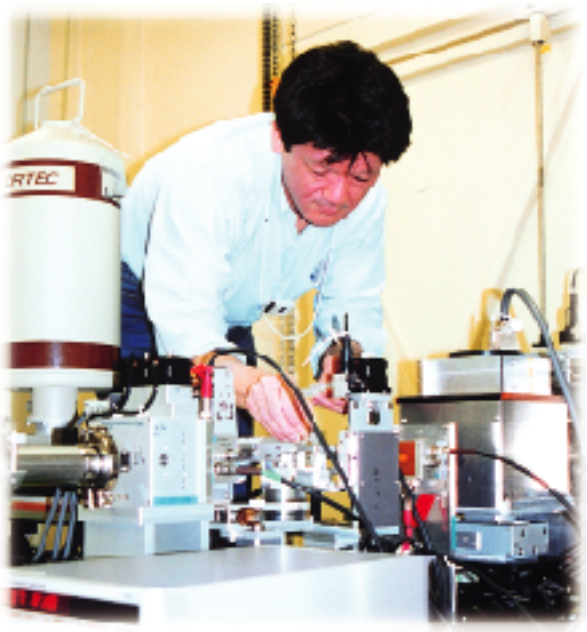

References

[1] S. Hayakawa *et al.*, Spectrochem. Acta B **54** (1999) 171.
[2] X. Jia *et al.*, Proc. of 4th ICNDST (1994) 525.
[3] S. Hayakawa, X.-P. Jia, M. Wakatsuki, Y. Gohshi and T. Hirokawa, J. Crystal. Growth **210** (2000) 388.

SPECTROSCOPY

The highly brilliant light ranging from the hard X-ray region to the soft X-ray region of SPring-8 provides remarkable opportunities for the study of the electronic structures of a wide range of atoms, molecules and condensed matter. Recently, there have been growing activities in magnetic circular dichroism (BL39XU, BL25SU), Compton scattering (BL08W), magnetic X-ray scattering (BL39XU), spectroscopy of atoms and molecules (BL27SU) and photoemission spectroscopy of solids (BL25SU). In addition, a new beamline for infrared spectroscopy (BL43IR) has been successfully commissioned. Especially, the high quality soft X-rays from SPring-8 combined with high-resolution monochromators have turned out to be highly efficient and unique in the world of photoemission experiments in strongly correlated systems. The relatively large escape depth of photoelectrons being excited by the soft X-rays have enabled us to perform "bulk-sensitive" photoemission experiments with sufficiently high energy resolution.

Atsushi Fujimori

STUDY OF ELECTRONIC STATES IN 3*d* TRANSITION-METAL OXIDES BY X-RAY RESONANCE MAGNETIC SCATTERING

Transition-metal oxides such as NiO, CoO, and MnO have been recently recognized as charge transfer type insulators of which the band gap exists between the p-band of O^{2-} and the upper Hubbard *d*-band of transition metal M^{2+}. The lower Hubbard band and the *p*-band overlap each other, while the degree of overlap and the energy level of each band differ among NiO, CoO, and MnO. Information regarding the mechanism of the spin state changes of these materials is crucial in the discussion of highly correlated antiferromagnetic insulators on the basis of the charge transfer model. In this context, the *p*-type band of these materials displays interesting magnetic features.

Due to the lack of an effective experimental method, such information of the spin states has never been elucidated. X-ray resonance magnetic scattering is a new spectroscopic method, providing spin resolved information regarding unoccupied states. This method can be applied to antiferromagnetic materials, even though magnetic circular X-ray dichroism or spin resolved photoemission spectroscopy are not applicable for these materials. Moreover, this method enables us to separate the electronic states according to symmetry utilizing polarization dependence of the scattering amplitudes.

The first observation of X-ray resonance magnetic scattering from NiO was reported by Hill *et al.* [1] , introducing the observation of a strong enhancement of magnetic scattering at the energy corresponding to the pre-peak position in the *K*-absorption spectrum. This peak was claimed to be due to the quadrupole resonant magnetic scattering corresponding to the *d*-band, which was also confirmed by Neubeck *et al.* [2]. Furthermore, they

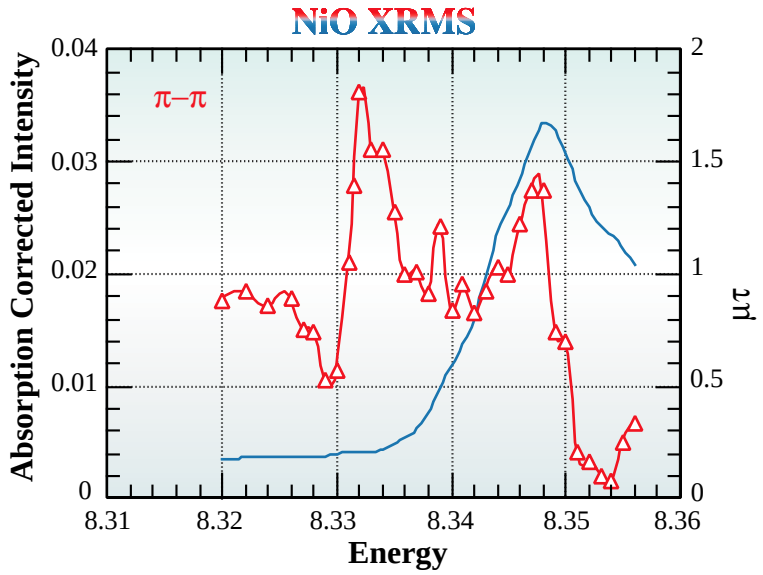

Fig. 1. Energy dependence of the resonance magnetic scattering intensity at the K-absorption edge of nickel. Polarization of the incident beam and scattered beam are in the π–π configuration. Intensities are corrected for the absorption. The K-absorption spectrum is designated by the solid line.

found dipole resonant magnetic scattering at energy corresponding to the main peak position in the *K*-absorption spectrum, along with an observation of CoO [3], where both dipole and quadrupole resonant magnetic scattering were also reported. The respective origins of the dipole scattering amplitude of NiO and CoO, however, still have not been satisfactorily determined. The 4*p*-bands of the transition metal in both NiO and CoO are believed to be empty, suggesting no existence of exchange splitting. We planned to investigate the spin polarized spectrum of the vacant states of antiferromagnetic NiO and MnO using polarization analyzed X-ray resonance magnetic scattering. This is the first step in our investigation of the transition metal oxides, toward the observation of the spin polarized spectrum of vacant states in the antiferromagnetic NiO [4].

The experiment was performed at **BL39XU** where the undulator X-ray beam is monochromatized by a Si (111) monochromator. A total reflection mirror is used to suppress higher harmonics. The X-ray beam is highly polarized in π polarization. To make σ polarized incident beam, a diamond phase retarder is used. A π or σ component of the scattered beam was analyzed by an Si (331) analyzer crystal. A sample is a slab-like (111) single T-domain crystal. Both components of the magnetization parallel and perpendicular to the scattering plane are possible to appear, as no magnetic field has been applied.

Rocking curves of a half integer order 5/2 5/2 5/2 reflection are measured in the π–π and the σ–σ polarization configurations at energies near the *K*-absorption edge. Integrated intensity plots, corrected for absorption, are shown in the figures. The spectrum shown by open triangles in Fig. 1 is measured in the π–π configuration, while the spectrum shown by open triangles in Fig. 2 is measured in the σ–σ configuration. The solid lines

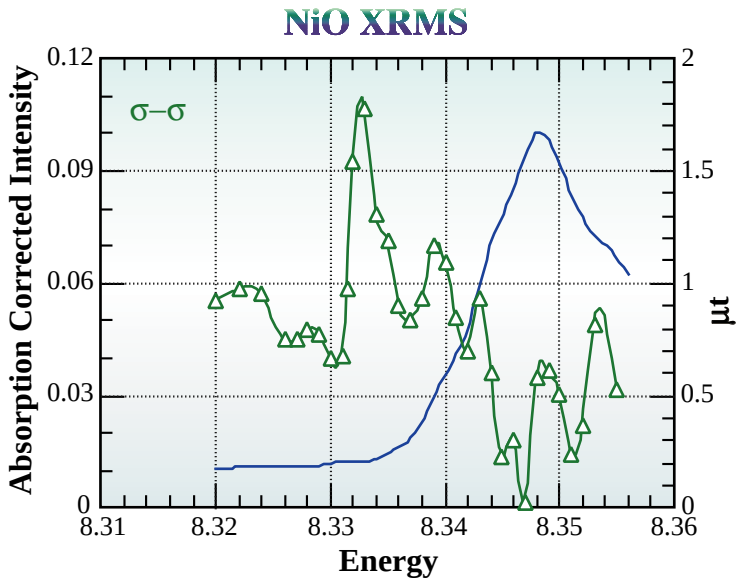

Fig. 2. Energy dependence of the resonance magnetic scattering intensity at the K-absorption edge of nickel. Polarization of the incident beam and scattered beam are in the σ–σ configuration. Intensities are corrected for the absorption. The K-absorption spectrum is designated by the solid line.

in both figures designate absorption spectra measured on NiO powder. We observed a strong intensity enhancement in both resonant magnetic scattering spectrum at 8.332 keV, corresponding to the pre-peak position of the absorption spectrum. Another strong intensity enhancement in the π–π configuration at 8.347 keV, corresponding to the main-peak position of the absorption spectrum, was observed, as well as an anti-phase dip at the same energy in the σ–σ configuration. Interestingly, this anti-phase behavior between the π–π and the σ–σ configurations appears again on the higher energy side of the 4*p* absorption peak. We recognize this phenomenon in Fig. 3, where the spectrum indicated by open triangles is a difference spectrum between π–π configuration and σ–σ configuration after being scaled at the maximum. An anti-phase oscillatory behavior in the difference spectrum suggests the existence of some other mechanism beyond the simple 4*p* polarization model. At the pre-peak position, the peak widths of the π–π configuration and the σ–σ configuration spectra interestingly appear to differ, where higher energy side of the π–π configuration spectrum is wider than that of the σ–σ configuration spectrum. A small hump in the difference spectrum at the pre-edge position in Fig. 3 indicates this fact. Our immediate future direction is to proceed to the measurement of MnO. A comparison of the spectra between NiO and MnO is highly expected.

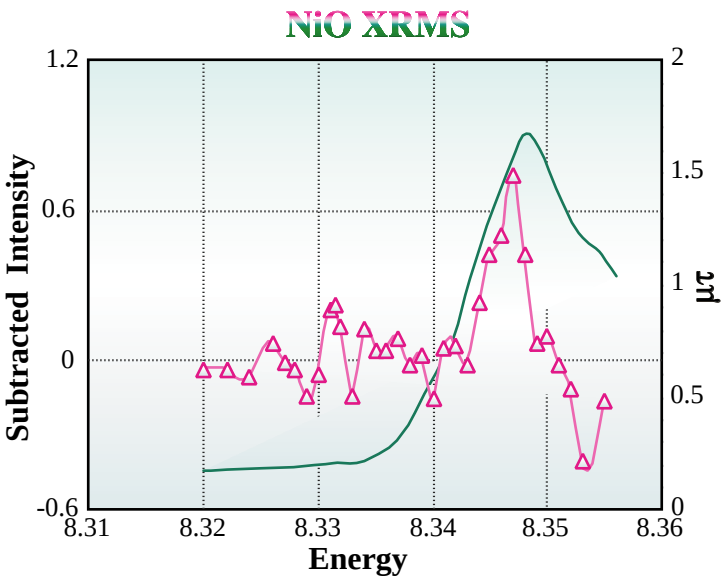

Fig. 3. A difference spectrum between the π–π configuration and the σ–σ configuration, after the intensity had been scaled at the maximum. Large p-type polarization appears at the region, which coincides with the main absorption peak. The spectrum is bipolar, while the absorption is unipoler type. A small hump can be seen at the slightly high energy side of the pre-edge absorption peak.

Kazumichi Namikawa[a], Hiroshi Maruyama[b] and Masahisa Ito[c]

(a) Tokyo Gakugei University
(b) Okayama University
(c) Himeji Institute of Technology

E-mail: namikawa@u-gakugei.ac.jp

References

[1] J.P. Hill *et al.*, Phys. Rev. B **55** (1997) R8662.
[2] W. Neubeck *et al.*, to be published.
[3] W. Neubeck *et al.*, Phys. Rev. B **60** (1999) R9912.
[4] K. Namikawa, H. Maruyama, M. Ito, E. Arakawa, N. Kawamura, M. Suzuki, A. Koizumi and M. Mizumaki, The 3rd Int. Forum Harima Conf. (2000) 16.

STEREOVIEW OF 3-D ATOMIC ARRANGEMENT BY CIRCULARLY POLARIZED-LIGHT PHOTOELECTRON DIFFRACTION

Stereoscopic photographs of a three-dimensional atomic arrangement have been obtained for the first time [1]. Two-dimensional photoelectron diffraction patterns obtained by left and right helicity light can be used as stereoscopic photographs when the two patterns are simultaneously viewed by the left eye and the right eye. Using a display-type spherical-mirror analyzer [2], stereoscopic photographs can be obtained directly on the screen without using any computer-aided conversion process.

Atomic arrangements, however, have not been yet directly observed. STM (scanning tunneling microscope) or TEM (transmission electron microscope) can provide atomic images in two-dimensional, but not in a three-dimensional atomic arrangement. Detailed atomic positions can be obtained with the use of other tools for structure analysis, such as LEED (low-energy electron diffraction) and X-ray diffraction, however requiring complicated analysis.

When the kinetic energy of photoelectrons from the core state is above several hundred eV, the scattering of photoelectrons from surrounding atoms create an intensity modulation in the angular distribution, known as photoelectron diffraction. The so-called forward focusing peaks appear in a two-dimensional photoelectron diffraction pattern along the direction connecting the emitter and the scatterer of photoelectrons. The recent research has shown that, utilizing circularly polarized light for the excitation of photoelectrons, these forward focusing peaks are rotated in the same direction as the electric vector of the incident circularly polarized light [3]. This was the first observation of the orbital angular momentum of electrons. This circular dichroism occurs for both chiral or magnetic materials and non-chiral and non-magnetic materials such as Si(001) [3] or W(110)-O [4] surfaces.

The rotation angle $\Delta\phi$ of these forward focusing peaks around the photon incident axis is expressed by a simple formula: $\Delta\phi = m / kR \sin^2\theta$ [3], where m is the magnetic quantum number of the photoelectron, k is its wave number, R is the internuclear distance between the emitter and the nearest-neighbor scatterer, and θ is the angle between the directions of incident photon and the outgoing photoelectron. This rotation has been explained as being due to the transfer of angular momentum of the photon to the photoelectron, where its z component angular momentum is changed by ±1 when excited by the circularly polarized light. The discovery of this rotation property has created new fields in the analysis of atomic, electronic, and magnetic structure of surfaces. Stereomicroscopy of atomic structure we describe herein is one of the most important applications of this phenomenon.

We show an example in Fig. 1, where (a), (b) indicate the photoelectron diffraction patterns of W 4*f* photoelectrons from W(110) surface at the kinetic energy of 800 eV for left and right circularly polarized light, respectively. This experiment was performed at **BL25SU** using the high-energy-resolution display-type spherical-mirror analyzer [5]. Its energy resolution is 0.3% of the pass-energy, and the angular resolution is higher than 1 degree. When Fig. 1 (a) is looked with the left eye and (b) with the right eye, the three-dimensional arrangement of atoms can be viewed as shown in (c): the A atom looks closer, the B and C atoms look farther, and the others look even farther. This image coincides with the real arrangement of W atoms viewed from the atom O, as shown in Fig. 1 (d). The magnification ratio is approximately 10^{10}.

These figures can be viewed as stereo-photographs

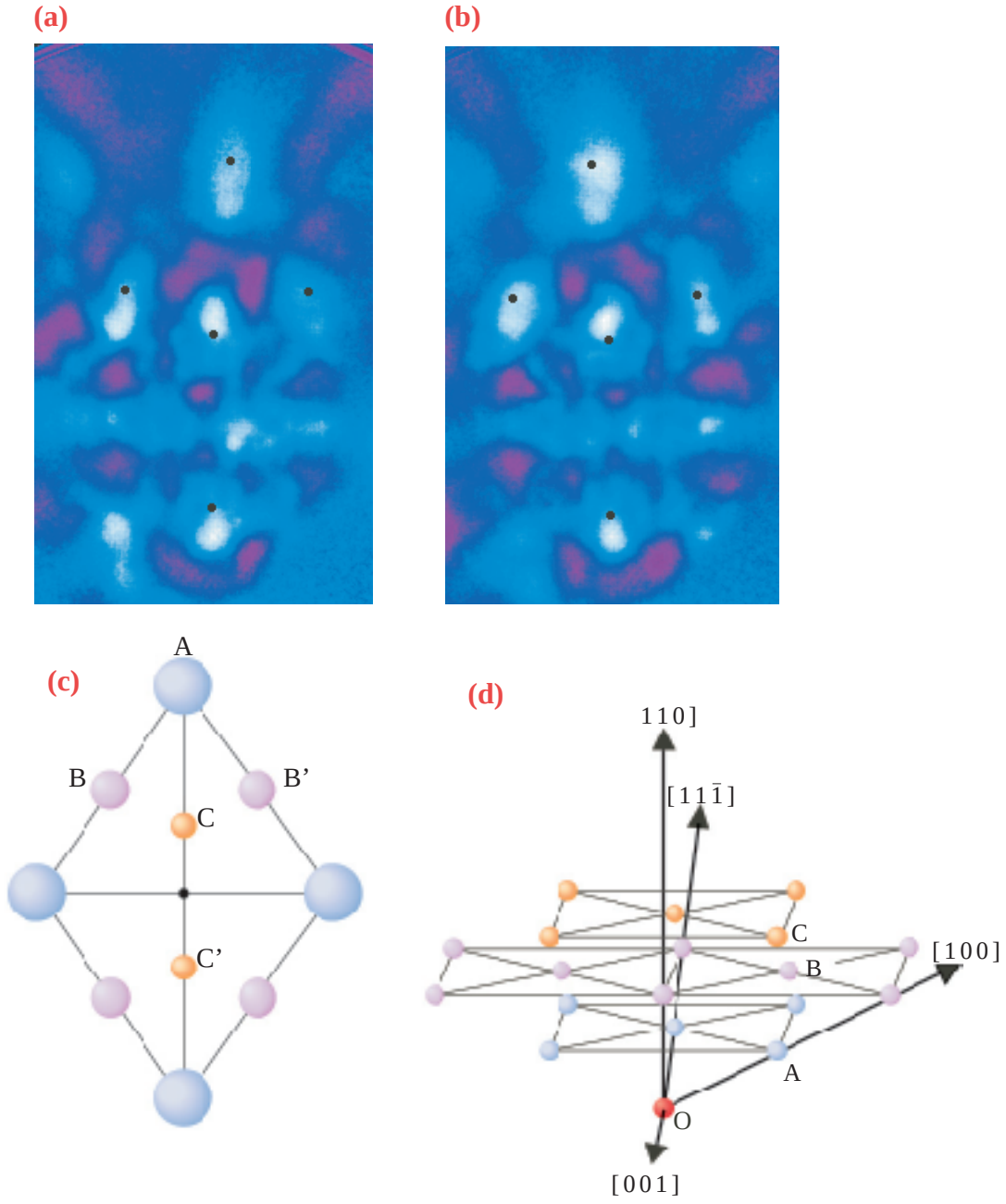

Fig. 1. Stereoscopic photographs of W(110) crystal, which is actually the two-dimensional circularly polarized-light photoelectron diffraction patterns of W 4f from the W(110) surface. ***(a)***, ***(b)*** *show the results for left and right circularly polarized light, respectively. The kinetic energy is 800 eV. The small black circles indicate the calculated directions of each forward-focusing peak along the crystallographic axes shown in* ***(c)***. *Looking at* ***(a)*** *with the left eye and* ***(b)*** *with the right eye, the three-dimensional arrangement of atoms shown in* ***(d)*** *can be viewed.*

due to the following reasons: the photoelectrons have orbital angular momentum, propagating from a point of some distance called the impact parameter, not from the center of the emitter atom; the angular momentum is the product of the momentum and the impact parameter, thus when the angular momentum is plus (minus), the impact parameter is also plus (minus); and these plus-minus impact parameters correspond to our right and left eyes, thus the obtained photoelectron diffraction patterns are the same as the image seen by right and left eyes. More details are described in ref. [1].

Hiroshi Daimon

Nara Institute of Science and Technology (NAIST)

E-mail: daimon@ms.aist-nara.ac.jp

References

[1] H. Daimon, Phys. Rev. Lett. **86** (2001) 2034.
[2] H. Daimon, Rev. Sci. Instrum. **59** (1988) 545.
[3] H. Daimon *et al.*, Jpn. J. Appl. Phys. **32** (1993) L1480.
[4] H. Daimon *et al.*, Phys. Rev. B **58** (1998) 9662.
[5] M. Kotsugi, K. Enomoto, Y. Miyatake, T. Nakatani, Y. Saitoh, T. Matsushita, S. Imada, T. Furuhata, S. Suga, K. Soda, M. Jinno, T. Hirano, K. Hattori and H. Daimon, Rev. Sci. Instrum. (2001) - in press.

DISSOCIATION DYNAMICS OF INNER-SHELL EXCITED MOLECULES BY MEANS OF PRECISE MEASUREMENTS OF RECOIL MOMENTA OF FRAGMENT IONS

When one of the inner-shell electrons of an atom in a molecule is promoted to a vacant valence molecular orbital or to a Rydberg orbital, either an Auger process or a series of Auger processes generally occur in the femtoseconds time scale and multiply charged ions are produced. These parent ions normally dissociate rapidly into fragments due to Coulomb repulsion among several positively charged centers. Recent research has demonstrated that nuclear motion can proceed in the core-hole state before the Auger decay occurs. This nuclear motion should be reflected in the angular correlation among products of dissociation that occurs following subsequent Auger decay.

To probe such nuclear motion in the study of dissociation dynamics, we have installed an apparatus at beamline **BL27SU** which enables us to take direct measurements of momentum distribution of all the fragment ions. This technique consists of a time-of-flight measurement using position-sensitive two-dimensional detectors with delay-line anodes. Combining this apparatus with the source of very high resolution linearly polarized soft X-rays [1], we have been able to study the dissociation dynamics of the linear triatomic molecule CO_2 following the excitation of either the C1*s* [2] or O1*s* [3] electron into $2\pi_u$ or σ^* molecular orbital in unprecedented detail. We focused on the three-body breakup of the triply charged molecular ion, $CO_2^{3+} \rightarrow C^+ + O^+ + O^+$, following the C1*s* $\rightarrow 2\pi_u$ excitation. The results of the measurements are best represented by so-called Newton diagrams as shown in Fig. 1. In these diagrams, the magnitude of the linear momentum of the first O^+ is normalized to unity and the vector is placed on the x-axis in the negative direction. The respective linear momentum of C^+ and the second O^+ are then plotted relative to this unit vector in the positive and negative y directions, respectively, so as to satisfy the momentum conservation requirements.

The separate observation of the two Renner-Teller split states claims for a salient feature in the present study. The C1$s^{-1}2\pi_u$ core-hole state is predicted to be split into two states via vibronic coupling with the bending vibration; one in which the π orbital lies in the bending plane (panel **a**, in-plane) and the other in which it extrudes perpendicularly from the bending plane (panel **b**, out-of-plane). However, the separate observation of these states has never been achieved. The present technique enables us to obtain this separation successfully. If only the events of which the vector product of the linear momenta of two O^+ fragments is parallel to the *E* vector and the linear momentum of the C^+ fragment is perpendicular to the *E* vector are selected from the recorded data, the selected events form an ensemble of the dissociation events from the core-hole state whose transition moment is perpendicular to the plane of the bending motion (panel **a**). In contrast, if the events of which the vector product of linear momenta of the two O^+ fragments is perpendicular to the *E* vector and the linear momentum of the C^+ fragment is parallel to the *E* vector are selected, then the obtained ensemble is that of the dissociation events from the core-hole state whose transition moment is parallel to the plane of the bending motion (panel **b**). For in-plane excitation, the islands of C^+ and second O^+ have clearly shown to possess considerably long tails, whereas those for out-of-plane excitation do not, indicating that the molecules are bent considerably in the former excitation just before

dissociation, whereas the latter is not. We can interpret this as reflection of the nuclear motion in the core-excited states toward the equilibrium geometry, representing the first direct verification of the occurrence of linear and bent structures for the C1$s^{-1}2\pi_u$ core-hole states (Renner-Teller split pair).

Norio Saito[a], Kiyoshi Ueda[b] and Inosuke Koyano[c]

(a) National Institute of Advanced Industrial Science and Technology
(b) Tohoku University
(c) Himeji Institute of Technology

E-mail: koyano@ sci.himeji-tech.ac.jp

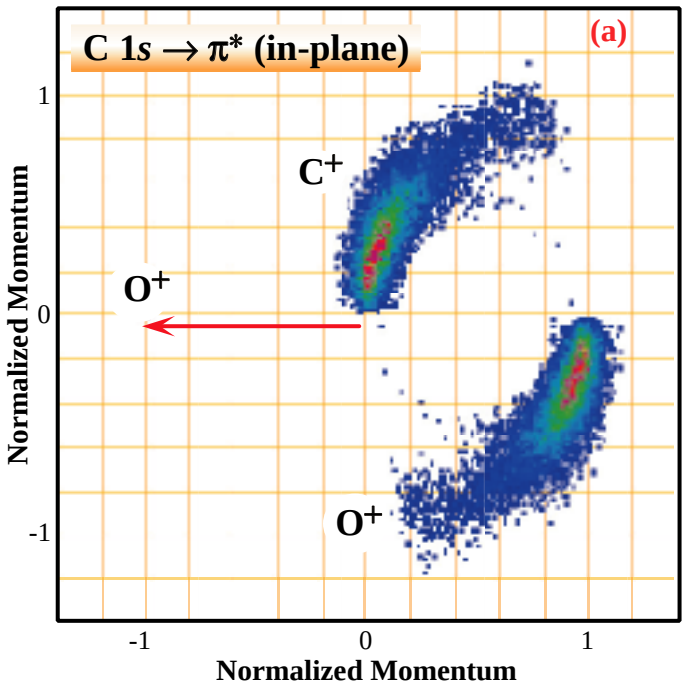

*Fig. 1. Newton diagrams for the three fragment ions, formed by three-body breakup of the triply charged molecular ion CO_2^{3+}. **(a)** for C1$s^{-1}2\pi_u$ (in-plane) excitation, **(b)** for C1$s^{-1}2\pi_u$ (out-of-plane) excitation.*

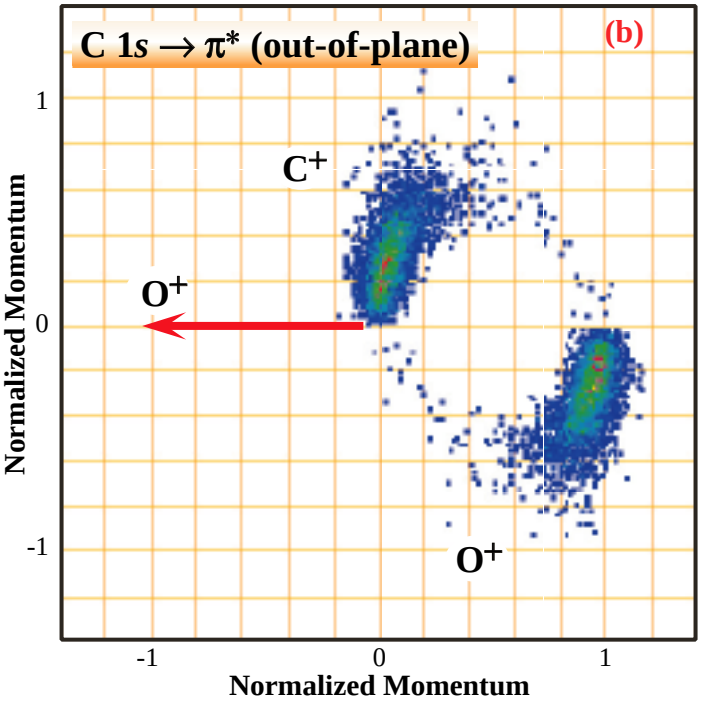

References

[1] H. Ohashi *et al.*, J. Electron Spectrosc. Rel. Phenom. - in press.

[2] N. Saito, M. Lavollee, Y. Muramatsu, F. Heiser, U. Becker, H. Chiba, K. Kubozuka, A. Czasch, T. Weber, R. Moshammer, H. Schmidt-Böcking, I. Koyano and K. Ueda, to be published in Phys. Rev. Lett.

[3] Y. Muramatsu, K. Ueda, N. Saito, H. Chiba, A. Czasch, T. Weber, R. Moshammer, O. Jagutzki, H. Schmidt-Böcking, M. Lavollée, K. Kubozuka and I. Koyano, to be published in Phys. Rev. Lett.

INSTRUMENTATION & TECHNIQUES

The developments of Instrumentation and Techniques at SPring-8 have come into a new stage in the sense that the recent developments are closely related to the outstanding characteristics of synchrotron radiation emitted by the ring. Considering that the important key words are "high brightness" and "high stability", most of the recent developments effectively utilize these specific qualities.

The above features is in striking contrast to the instrumentation developed just after the commissioning of SPring-8, which could be called "first stage" because in most cases the output results were obtained just based on the high flux of SPring-8. In this sense the first stage could be characterized just by an extension of instrumentation and techniques developed at second-generation light sources.

The following section provides three examples of such developments made in the above new stage.

The first topic describes a specially designed crystal bender. The incident beam position should be very stable, because otherwise the "fixed" position may move in the vertical direction. A larger incident beam size that is typical in second-generation sources, might increase such aberrations.

The second article discusses the use of high-resolution spectroscopy on molecules. Obviously, such high resolution has been obtained just because of the coherent irradiation on the diffraction grating used, which has become feasible due to the very small vertical emittance of the stored beam.

The third topic is related to the modulation of circular polarization of undulator radiation. Although the principle of modulation spectroscopy is very clear, great care has to be taken not to disturb the position of the stored beam during the modulation. In fact, even a small movement of the position might produce "false" MCD signals. Whether this kind of "false" effect is negligible or not should be evaluated in the future.

Tsuneaki Miyahara

FIXED HEIGHT EXIT BENDER OF SYNCHROTRON X-RAY ABOVE 40 keV

Sagittal focusing is an efficient method for focusing synchrotron X-rays. Usually, the second crystal of a double-crystal monochromator is bent into a cylindrical shape, ideally without introducing any deformation of the crystal in the scattering plane. Accordingly, both energy and momentum resolutions are kept as high as those achieved by flat-flat double-crystal monochromators. The radius of the bend that will provide optimal focussing is a function of the Bragg angle; as the Bragg angle becomes smaller, so does the radius. Various bending mechanisms for sagittal focusing have been developed. However, most applications have been restricted to relatively low energy X-rays due to the difficulty of generating an ideal bend with small radius. In addition, simultaneous achievement of optimal focus and fixed-exit height despite changing output energy is preferable for most applications, and requires an even more complex bending mechanism.

Although the rhombohedral or double triangle ribbed crystals bent with a cam driver mechanism fulfill the fixed-exit condition, they are apt to introduce non-uniform bend due to cramping at the crystal center. We developed a new sagittal focus bender [1] that is compatible with the SPring-8 standard monochromator [2,3] for bending-magnet beamlines. In principle, the bender uses a conventional four-point bending mechanism, but the rollers for four-point bending are attached to rotation arms, making the central position of the crystal fixed regardless of the bending radius. This procedure is based on a simple geometrical theorem illustrated in Fig. 1(a). Two circles, A and B, are always across at the right angles to the circles C and D, the centers, O_C and O_D, of which lie on the

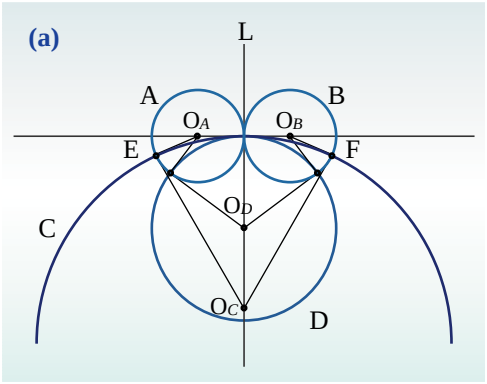

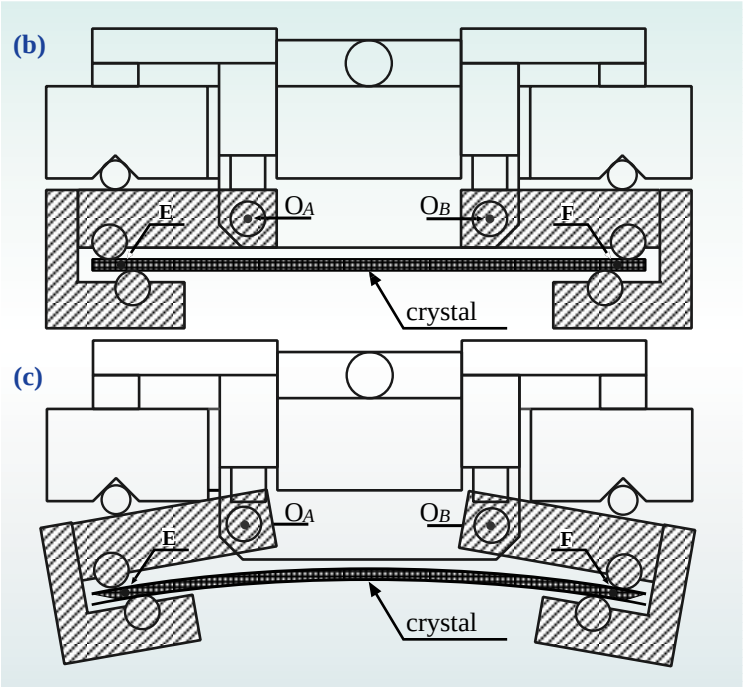

Fig. 1. ***(a)*** *Geometrical basis of the fixed exit bender. Actual bending mechanism* ***(b)*** *when the crystal is flattened and* ***(c)*** *when the crystal is bent.*

perpendicular bisector L of the centers of circle A and B. This shows that the crystal, which corresponds to either circle C or D in Fig. 1, is bent cylindrically without changing the height of the middle point of its arc, when pure torque is applied at the cross points E and F. The actual bending mechanism when the crystal is flattened is shown in Fig. 1(b). The crystal was cramped with four cylindrical rollers of the cradle (gray region in Figs. 1(b) and 1(c)). The bending is performed without changing the position of the crystal center by rotating the cradle around O_A and O_C, as shown in Fig. 1(c).

Since the SPring-8 standard monochromator is designed to keep the exit-beam height constant, even with in changing energy, combination of the bending mechanism with the monochromator also preserves exit-beam height constancy with an optimized bending radius for each energy.

We used a row of grouped crystals joined by thin hinges of a Si (3 1 1) plate with a rectangular shape of 90 mm (along the beam) $\times$ 100 mm (across the beam) $\times$ 2 mm (thickness), as shown in Fig. 2, in order to avoid anticlastic bending that would degrades the total throughput. The focusing test was carried out at **BL14B1**, which is a bending magnet beamline dedicated to JAERI and equipped with a SPring-8 standard double-crystal monochromator. The fixed-exit bender was mounted on the second crystal stage of the monochromator as shown in Fig. 3. A pair of (3 1 1) Si crystals were used both for the first and second crystals. For the first crystal, an indirectly cooled flat plate was used instead of the standard direct fin-cooled crystal.

Figure 4 shows the observed beam profiles at 40 keV with different bending radii, R. The horizontal beam size was 65 mm at the screen position for the unbent crystal. The beam reflected from the slot parts of the crystal appeared like the teeth of a comb. We can quantify the number of slots reflecting the X-ray beam by counting the sharp lines. From the image, all slots were found to reflect the X-ray beam even when the bending radius was 4 m. The gain of the photon density was measured by horizontal slit scans, and was found to be 12 times larger than the flattened crystal, when the bending radius of 4 m was used (Fig. 4).

Dynamic sagittal focusing testes were performed

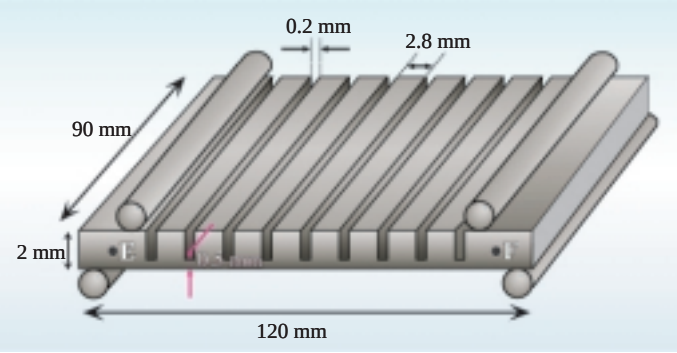

Fig. 2. Schematic diagram for a series of crystal slabs joined by thin hinges, cut parallel to the bending rods.

between 40 keV (R = 4 m) and 60 keV (R = 2 m). The beam height at the sample position was measured after optimizing of the bending radius and the parallel alignment the first and second crystals. The deviation of the beam height in the above energy range was within ±0.15 mm. Preliminary setup was carried out with flat-flat double crystals before installing the bender. The deviation of beam height with flat-flat double crystals was 0.1 mm in the 40 keV to 60 keV range. The practical deviation of beam height with the bender was somewhat larger than expected. When bending is performed, the fixed points are not on the surface of the bent crystal, but only in the center of the crystal. Because of the thickness and polygonal nature of the bent crystal, the practical beam height was changed slight in the 40 keV to 60 keV range. However, the beam deviation should be negligible in most experiments.

This sagittal focus bender is designed for an inclined double crystal monochromator. The properties of sagittal focusing of inclined geometry with a Si (111) reflection were tested. In Fig. 5 we compare a near-edge spectrum of a Cu foil registered in a dynamically focusing mode with that of a normal flat crystal. Because the two spectra are identical, we conclude that energy resolution is not affected by sagittal focusing, nor is any distortions introduced.

Dynamical sagittal focusing in a wide energy range, from 8.5 keV to 150 keV, performed without exchanging monochromator crystals will become feasible by using the present bending mechanism in the inclined geometry.

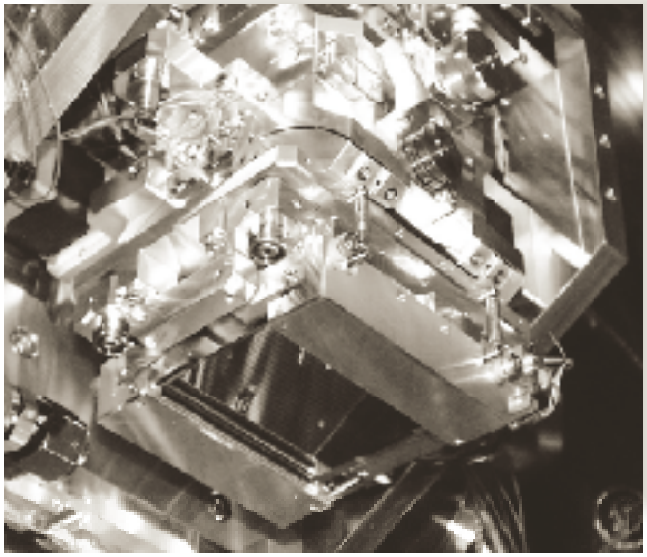

Fig. 3. Sagittal focus bender with a row of grouped crystals joined by thin hinges installed in standard monochromator as the second crystal.

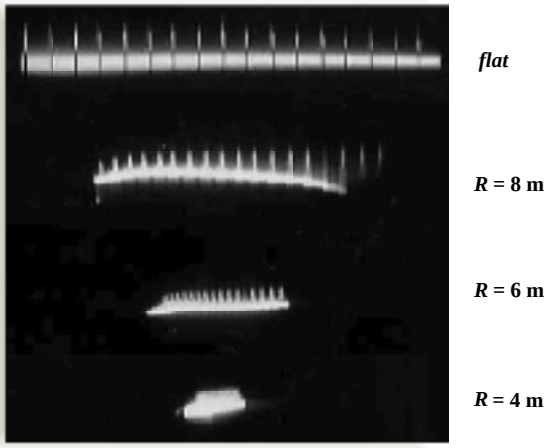

Fig. 4. Beam profiles using the sagittally focusing crystal monochromator at 40 keV. The period of the slotted crystal is 3 mm. The X-ray beam was more effectively focused at smaller bending radii R.

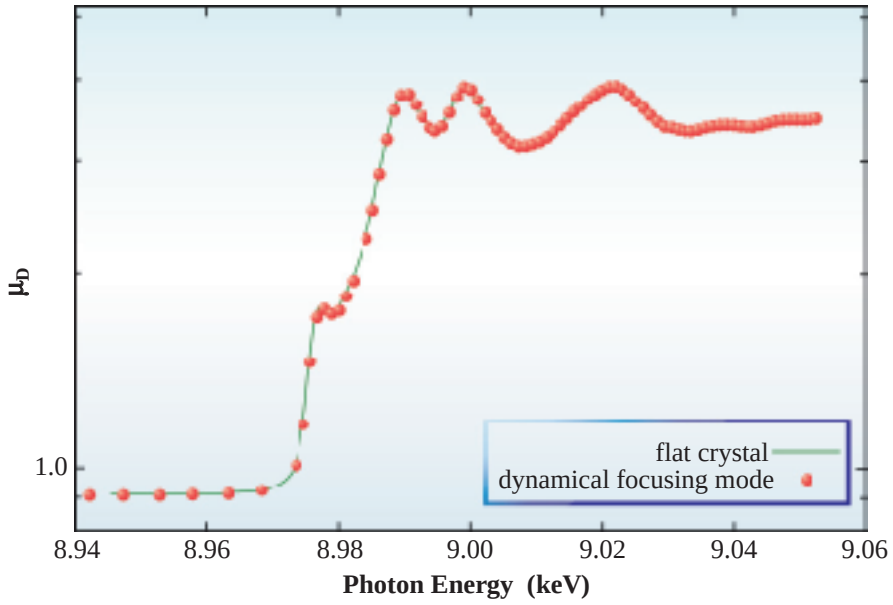

Fig. 5. Near-edge absorption spectra of Cu foil, registered in the dynamical focusing mode and in the flat crystal mode. Energy resolution is not affected, as all edge structures are reproduced without distortion.

Yasuhiro Yoneda

SPring-8 / JAERI

E-mail: yoneda@spring8.or.jp

References

[1] Y. Yoneda, N. Matsumoto, Y Furukawa, and T. Ishikawa, J. Synchrotron Rad. **8** (2001) 18.

[2] T. Uruga *et al.*, Rev. Sci. Instrum. **66** (1995) 2254.

[3] M. Yabashi *et al.*, SPIE Proc. **3773** (1999) 2.

HIGH-RESOLUTION RESONANT AUGER ELECTRON SPECTROSCOPY FOR INVESTIGATING NUCLEAR MOTION IN CORE-EXCITED MOLECULES

Synchrotron radiation sources and the soft X-ray monochromators have been improved significantly in the past few decades. Currently, it is possible to promote a specific inner-shell electron to any unoccupied atomic and molecular orbital with an excitation photon band pass smaller than the natural width of the inner-shell excited states. In this context, the experimental width of the Auger lines is not determined by the natural width of the inner-shell excited states, but, in general, by the convolution of the excitation photon band pass and the band pass of the electron energy analysis. This line narrowing effect, often called the Auger resonant Raman effect, has been used for spectroscopic investigations of the Auger final states of rare gas atoms, as well as for investigations of the nuclear motion dynamics of the inner-shell excited molecules. The inner-shell excited molecule thus created decays mostly via the resonant Auger emission, initiating molecular dissociation. Nuclear motion, however, occurs in the core-excited state on a timescale of tens of fs, which is the lifetime of the inner-shell excited state, affecting the dissociation after the Auger decay. The objective of this study is to establish resonant Auger spectroscopy as a direct probe of the nuclear motion in the core-excited states.

Experiments were performed at the soft X-ray photochemistry experimental station (C-station) installed at beamline **BL27SU** [1]. This experimental station is designed for the study of photoionization and electronic relaxation dynamics

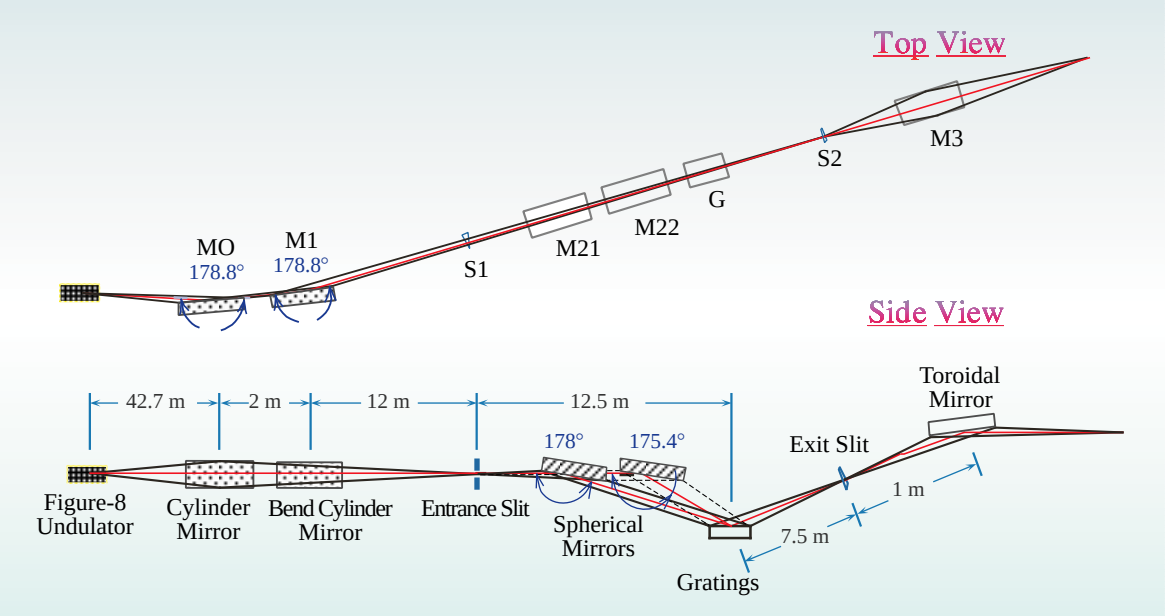

Fig. 1. Optical layout of the monochromator at BL27SU.

of core-excited atoms and molecules, as well as the observation of ion fragmentation processes of molecules by using a high resolution monochromator (E/ΔE >10000). The monochromator is of the Hettrick type, and is equipped with varied line spacing plane gratings and spherical focusing mirrors [2]. Figure 1 shows the optical layout of the monochromator. Three gratings and two spherical mirrors cover the photon energy range from 0.2 to 3 keV. By measuring the photoabsorption spectrum of rare gas atoms and N_2 in the *K*-shell excitation region, the resolving power (E/ΔE) is estimated tentatively. For example, Fig. 2 shows the Ne photoabsorption spectrum in the $1s \rightarrow np$ Rydberg resonance excitation region. The $1s \rightarrow np$ (n= 3 - 6) transitions are clearly discerned in the spectrum. Comparison with other high-resolution photoabsorption measurements leads an estimated resolving power (E/ΔE) of better than 10000. The details of the monochromator and the performance tests have been reported in recent articles [3-5].

In the past year, we have installed a high-resolution electron energy spectroscopy apparatus (GAMMADATA-SCIENTA SES 2002 with a tunable gas cell GC-50) onto the beamline as a part of the end station and initiated the subnatural-width resonant Auger electron spectroscopy of atoms and molecules [6-8]. The first result of this investigation using the Ne $1s \rightarrow 3p$ excitation is as follows. Figure 3 shows the observed resonant Auger emission lines, whose final states are $Ne^+2p^{-2}(^1D_2)3p$. The photon band pass and the band pass for the electron energy analyzer are 60-68 meV and 13 meV, respectively, while the Doppler width due to thermal motion of the Ne atoms is 79 meV. The measured width of 100 - 105 meV is the convolution of these three widths and is much smaller than the natural width of the Ne 1*s* hole state (~ 250 meV). At this resolution, we distinguished for the first time three multiplet components — ^2P, ^2D, and ^2F — and confirmed that the measured values of the anisotropy parameter β for these three are in excellent agreement with the theoretical predictions [8].

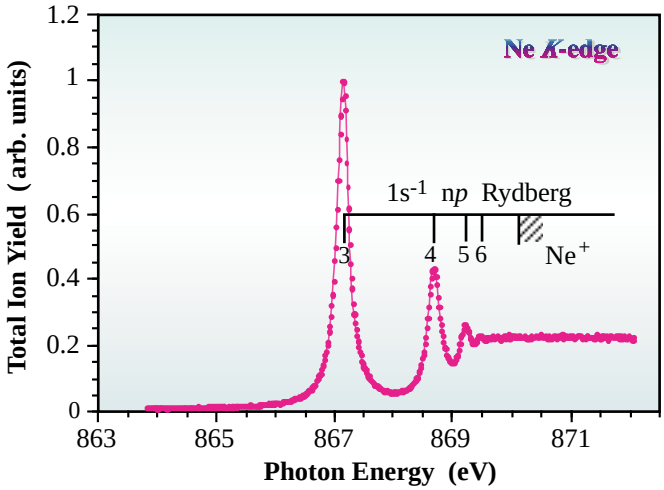

Fig. 2. Total ion yield spectrum of Ne at K-edge.

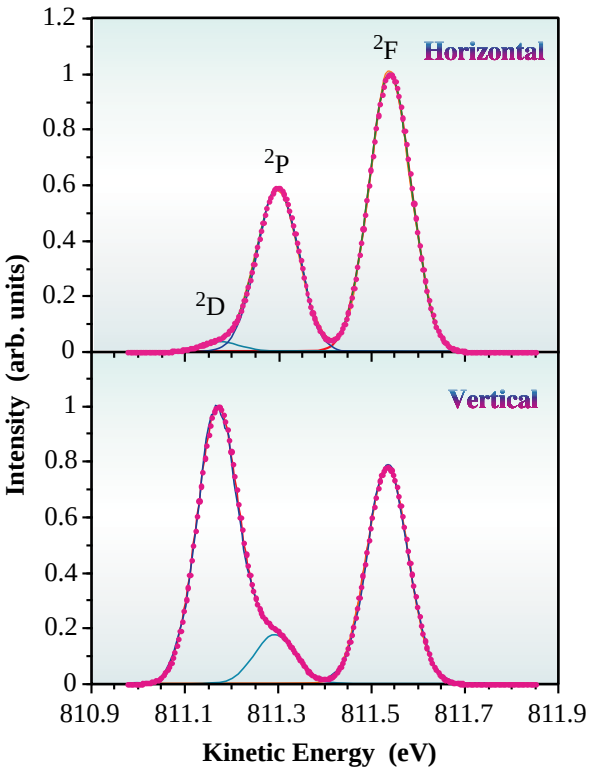

Fig. 3. Part of the electron spectra of the resonant Auger transitions from the Ne $1s^{-1}3p$ state to the final Ne^+ $2p^{-2}$ ($^1D_2$)3p — ^2D, ^2P and ^2F — states recorded at a photon energy of 867.12 eV with horizontal (upper) and vertical (lower) polarizations. The electron spectrometer axis is in the horizontal direction.

Yuske Tamenori[a], Haruhito Ohashi[a] and Kiyoshi Ueda[b]

(a) SPring-8 / JASRI
(b) Tohoku University

E-mail: tamenori@spring8.or.jp

References

[1] I. Koyano *et al.*, J. Synchrotron Rad. **5** (1998) 545.

[2] M. C. Hettrick and S. Bowyer, Appl. Opt. **22** (1983) 3921.

[3] E. Ishiguro *et al.*, J. Electron Spectros. Relat. Phenom. **101-103** (1999) 979.

[4] H. Ohashi. E. Ishiguro, Y. Tamenori, H. Okumura, A. Hiraya, H. Yoshida, Y. Senba, K. Okada, I. H. Suzuki, N. Saito, K. Ueda, T. Ibuki, S. Nagaoka, I. Koyano and T. Ishikawa, Nucl. Instrum. Meth. (2001) - in press.

[5] Y. Tamenori, H. Ohashi, E. Ishiguro, H. Okumura, T. Fukui, T. Miura, H. Kishimoto, J. Tanase, N. Kamachi, K. Endo and T. Ishikawa, Nucl. Instrum. Meth. (2001) - in press.

[6] Y. Shimizu *et al.*, J. Phys. B **33** (2000) L685.

[7] Y. Muramatsu *et al.*, Chem. Phys. Lett. **330** (2000) 91.

[8] Y. Shimizu, H. Ohashi, Y. Tamenori, Y. Muramatsu, H. Yoshida, K. Okada, N. Saito, H. Tanaka, I. Koyano, S. Shin and K. Ueda, J. Electron Spectros. Relat. Phenom. (2001) - in press.

PERIODIC POLARIZATION SWITCHING FOR MCD MEASUREMENTS

Light polarization has become increasingly important for such soft X-ray spectroscopic techniques as magnetic circular dichroism (MCD) and circular dichroism (CD) measurements. Such experimental methods require good polarization quality and the fast switching of photon helicity. To promote high-sensitivity studies and to improve the signal-to-noise ratio for circular dichroism, we have developed a new MCD measurement system coupled with the right and left circular polarizations (RCP and LCP) switching [1].

BL23SU is a soft X-ray beamline used for spectroscopic studies for a wide variety of applications, such as surface chemistry, biology, and condensed matter physics [2]. The light source (ID23) is an APPLE-2 type undulator [3]. Figure 1 shows the structure and motion of permanent magnet rows of the undulator. This planar double-array undulator generates any kind of elliptical polarization of light by adjusting the relative position of pairs of magnet rows (phase shift) and changes the photon energy in the soft X-ray range by varying the gap distance between the upper and lower jaws.

Figure 2 provides an outline of the MCD-measurement-control system at beamline **BL23SU**, which is based on the SPring-8 public beamline model [4]. Experiments using MCD measurements can be performed with a personal computer (MCD-PC) by using sophisticated applications software. The beamline workstation (BL-WS) is connected to the MCD-PC and controls the beamline insertion device (ID23-gap/phase) and the monochromator [5], which establishes the selected monochromatized photon energy, maintaining the robustness of the system.

The MCD sample current (I_1) and monitor current (I_0) are collected by the MCD-PC. During the MCD measurements, the undulator control, the monochromator control, and the data accumulation

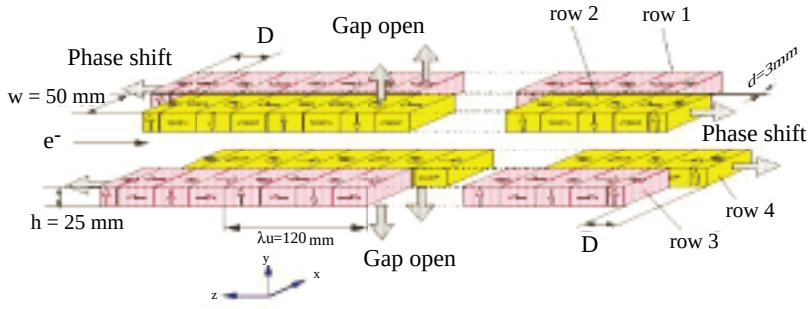

Fig. 1. The magnetic structure and movement of the double-array undulator. λu and D indicate the magnetic period length and the phase shift distance, respectively.

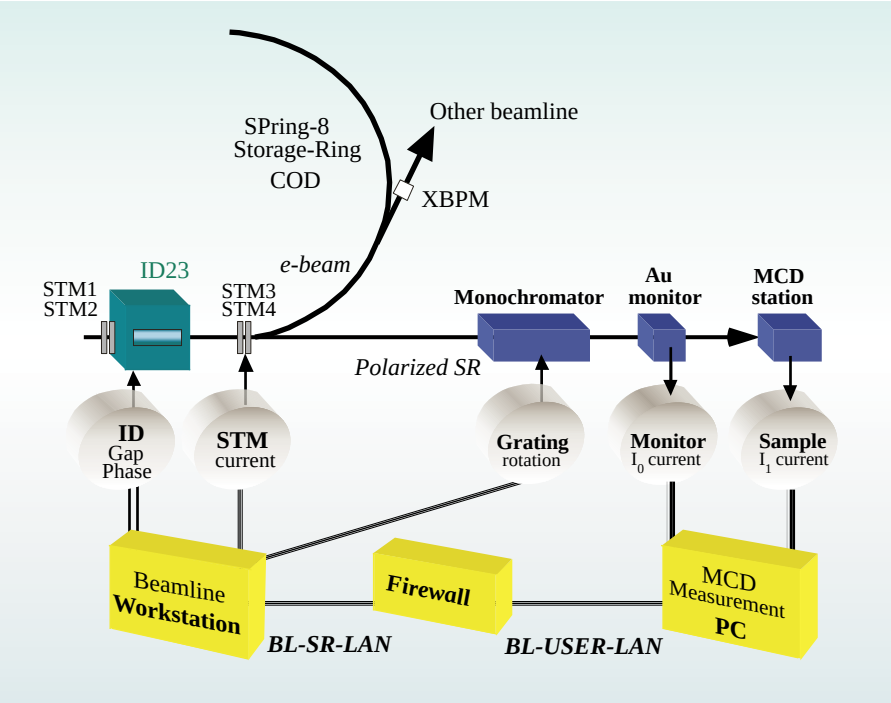

Fig. 2. Schematic illustration of the MCD measurement control system at beamline BL23SU with ID23. Experimenters can carry out the MCD measurements via several SPring-8 networks, including BL-SR-LAN and BL-USER-LAN. VMEs and BL-X-terminals are omitted.

are operated simultaneously. For instance, a measurement cycle proceeds as follows: (i) photon energy tuning; (ii) ID23 phase-shift to provide RCP X-rays; (iii) simultaneous sampling of I_0 and I_1; (iv) ID23 phase-shift to provide LCP X-rays; and (v) sampling again of I_0 and I_1. At this point the cycle returns back to (i) to be continued. Figure 3 shows the first results of MCD measurements, made for the of Fe2*p* absorption of Fe metal in a magnetic field of 0.4 T excited by RCP and LCP soft X-rays with a polarization switching frequency of 0.1 Hz. We believe that this circular dichroism measurement system with periodic photon-helicity switching by a variably-polarizing undulator provides great opportunities for the study of a very weak circular dichroism signals in the soft X-ray region.

It should be noted that the closed orbit distortion of the storage ring caused by the ID23 drive is minimized using the steering magnets installed in the upstream and downstream of the undulator.

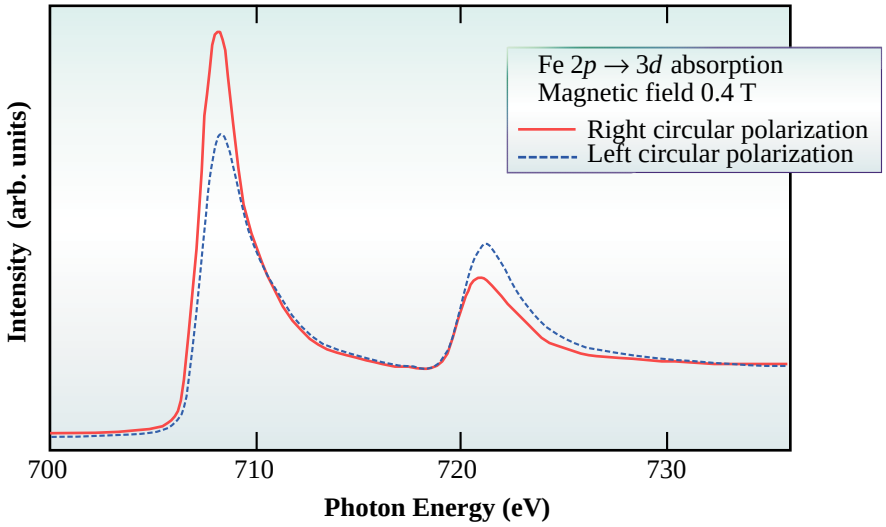

Fig. 3. Fe $L_{2,3}$ absorption spectra of Fe metal in a magnetic field 0.4 T excited by right and left polarized X-rays with a polarization switching frequency of 0.1 Hz.

Akane Agui[a], Takeshi Nakatani[a,b] and Tomohiro Matsushita[b]

(a) SPring-8 / JAERI
(b) SPring-8 / JASRI

E-mail: agui@spring8.or.jp

References

[1] A. Agui, A. Yoshigoe, A.Yokoya, Y. Saitoh, Y. Hiramatsu, T. Shimada, T. Nakatani, T. Matsushita, Y. Miyahara, H. Tanaka, M. Takeuchi, T. Bizen, S. Sasaki, M. Takao, H. Aoyagi, T.P. Kudo, K. Satoh, S. Wu, and H. Ohkuma, to be published in Rev. Sci. Instrum.

[2] A. Yokoya *et al.*, J. Synchrotron Rad. **5** (1998) 10.

[3] S. Sasaki, Nucl. Instrum. Meth. A **347** (1994) 83.

[4] T. Nakatani *et al.*, J. Synchrotron Rad. **5** (1998) 536.

[5] Y. Saitoh, Y. Teraoka, A. Agui, A. Yoshigoe, A. Yokoya, to be published Nucl. Instrum. Meth. (2000).

Industrial Applications

Wide variation in the usage of atomic elements in mixed or composite materials has been a current trend in the industrial fields of semiconductors and metallic, magnetic, ceramic, and plastic materials. Many companies are now interested in the possibility of using synchrotron radiation X-rays for material characterization as well as development of new materials or improvement of production technologies. Measurement of XAFS, X-ray fluorescence analysis, and X-ray diffraction for small areas in such materials provides especially useful information in terms of crystallinity or component distribution. In this section, some interesting industrial applications of synchrotron radiation X-rays in the industrial field are shown.

Advanced rechargeable batteries are required for portable computers, phones, automobiles, and other various electronic products for communication. In order to improve the efficiency and prolong the life of these devices, it would be useful to explore the behavior of cathode materials in the batteries during the recharge cycle.

Development of high-density recording devices has been an active pursuit in the information technology field. Giant magnetic resistance multilayers can be one of the candidates for the high-density magnetic recording material. Therefore, detailed analysis is important to determine the precise components and multilayer thicknesses.

Feature sizes of electronic devices such as LSI's and semiconductor lasers have become progressively smaller. On the other hand, the diameter of substrate wafers is increasing, making homogeneity of crystal quality crucially important. In order to investigate minute strains giving rise to the generation of crystalline defects or wafer warpage, X-ray topography or micro-diffraction combined with a precisely parallel X-ray beam is advantageous. Large-diameter silicon wafers for future LSI's are imaged with a contrast depicting the strain distribution in topographic plates. Also peak shifts in the X-ray rocking curves using an X-ray microbeam show local lattice deformation in active regions in the electronic devices, which may lead to deterioration of the device performance or poor production yields.

Thus, the hard X-rays from third-generation synchrotron radiation such as those generated at SPring-8, are predicted to be useful for industrial material characterization.

Junji Matsui

IN SITU XAFS STUDY ON CATHODE MATERIALS FOR LITHIUM-ION BATTERIES FROM THE STANDPOINT OF INDUSTRIAL USE

$LiNi_{0.8}Co_{0.2}O_2$ is one of the current candidates for a cathode material of advanced rechargeable batteries with high capacity. The stability of $LiNi_{0.8}Co_{0.2}O_2$ is superior to $LiNiO_2$, exhibiting a single-phase region upon oxidation from 3.0 V to 4.1 V. The capacity fading, however, occurs not only during charge/discharge cycling but also when batteries are kept at high temperatures, creating difficult problems for practical use. To overcome the problems of capacity fading, it is essential to understand the electronic and structural changes accompanied by the capacity fading. For this purpose, *in situ* XAFS analysis is very useful, because it gives information on both the local and electronic structure surrounding an absorbing atom without disassembly of the battery for a measurement. Some studies applying *in situ* XAFS analysis to $LiNiO_2$ or $LiNi_{0.5}Co_{0.5}O_2$ have been already reported [1-3]. Nakai *et al.* revealed that the oxidation of the Ni ion occurred and the Jahn-Teller distortion of the NiO_6 octahedron decreased with Li deintercalation. The *in situ* XAFS analysis of the capacity faded battery, however, has not been reported. In this study we prepared the batteries with various capacities to measure the *in situ* Ni and Co *K*-edge absorption spectra of $LiNi_{0.8}Co_{0.2}O_2$ [4].

Figure 1 shows a drawing of the coin cell newly developed for *in situ* XAFS measurements in a transmission mode. The use of 0.4 mm Beryllium windows allow X-rays to penetrate the cell. XAFS data can therefore be obtained at various voltages without removing the cathode material from the cell.

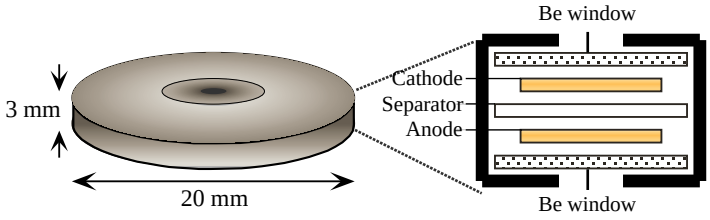

Fig. 1. Schematic drawing of the coin cell.

Table 1. The conditions of cells.

Cell no.	Condition	Capacity (relative value)
1	Initial state (no treatment)	NA
2	After one charge/discharge cycle*	100
3	After 515 charge/discharge cycles*	9.5
4	After keeping at 80 °C for 3 days**	64.3
5	After keeping at 60 °C for 25 days**	14.7

* The charge/discharge cycling have been done at rate of 1 mA/cm^2 in the range of voltage from 3.0 V to 4.1 V.
** Kept at charged state which corresponds to a voltage of 4.1 V.

To investigate the changes resulting from cycling and keeping at high temperatures, we prepared cells at different cycling states, and keeping temperature and time conditions. The cells used in this study are summarized in Table 1.

Ni and Co *K*-edge XAFS data were collected using beamline **BL16B2**. Incident X-rays were monochromatized using a Si (111) double-crystal monochromator. The harmonic content of the beam was minimized utilizing a Rh-coated Si mirror, inclined to 5 mrad. The X-ray intensities were monitored using ionization chambers filled with nitrogen gas for the incident beam and a mixture of argon (25%) and nitrogen (75%) for the transmitted beam.

Figure 2 shows the Ni *K*-edge XANES spectra of $LiNi_{0.8}Co_{0.2}O_2$ for several samples. In both edges, chemical shifts of the edge peak energy were found. A graphical comparisons of the edge peak energies as a function of the cell voltages are shown in Fig. 3. The edge peak energy (Ep) is defined here as the energy at maximum height of the edge jump. Continuous shifts toward higher energies indicate the increases in the average oxidation states of Ni upon lithium removal [2]. For capacity faded samples, the ranges of chemical shifts upon charging are less than that in "after one cycle". A good correlation between the range of chemical shift and the capacity of the cell was found.

Fourier-transformation of the Ni *K*-edge EXAFS spectra for several samples are demonstrated in Fig. 4. The first peak at approximately 1.5 Å corresponds to Ni-O interactions, and the second peak at approximately 2.5 Å corresponds to Ni-Ni interactions. The Ni-O peak height of the sample in its initial state is lower than that of the capacity faded samples. This phenomenon is explained by the local Jahn-Teller distortion of the NiO_6 octahedron, due to the low spin Ni^{3+}. The distorted NiO_6 octahedral coordination, such as 4(shorter) + 2(longer) Ni-O bonds, causes the apparent decrease in the Ni-O peak height resulting from interference of the imaginary and real part of the FT [2]. The graph of the heights of the Ni-O peak plotted as a function of the cell voltage (Fig. 5), reveals that, upon charging, the extent of the local distortion is reduced, and the distorted NiO_6 octahedron becomes a regular octahedron.

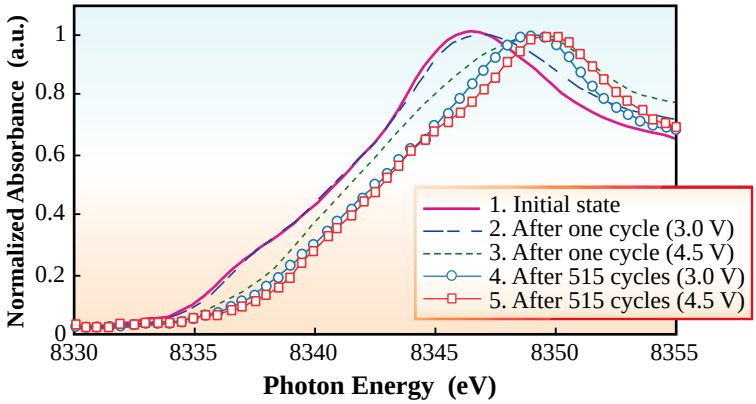

Fig. 2. Ni K-edge XANES spectra of $LiNi_{0.8}Co_{0.2}O_2$

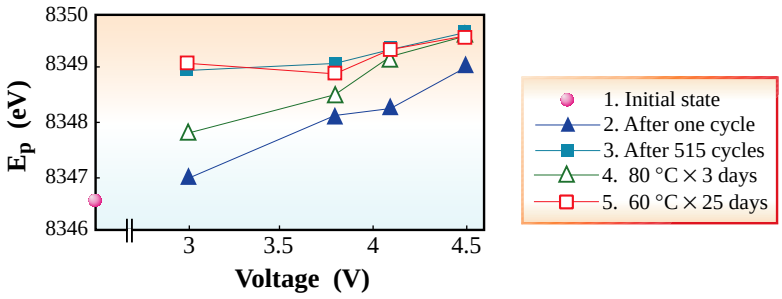

Fig. 3. Graphical comparison of the edge peak energies (E_P) as a function of the voltages.

This phenomenon results from the gradual changes of the average valence of Ni from 3+ to 4+, making the shape of Fig. 5 similar to that of Fig. 3.

The averages of the Ni-O distances deduced from quantitative analysis of EXAFS data are shown in Fig. 6. The curve-fitting were performed with the coordination numbers of oxygen fixed to 6. "After one cycle", the Ni-O distance obviously decreases upon charging, while in "after 515 cycles", the distance changes only slightly. The change of the Ni-O distance originates mainly from the change in the ion-radii accompanied by the change in oxidation from Ni^{3+} to Ni^{4+}.

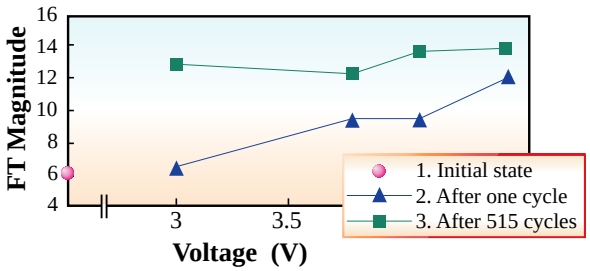

Fig. 5. A comparison of the heights of Ni-O peaks in FT spectra as a function of the voltages.

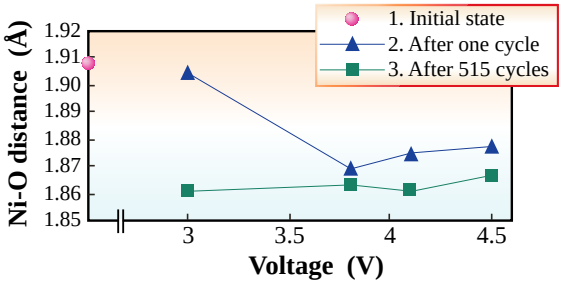

Fig. 6. A comparison of the averages of Ni-O distances as a function of the voltages.

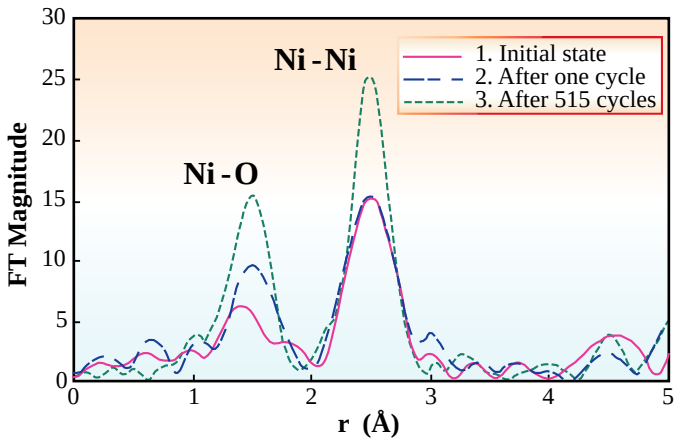

Fig. 4. Fourier transformation of Ni K-EXAFS spectra for $LiNi_{0.8}Co_{0.2}O_2$.

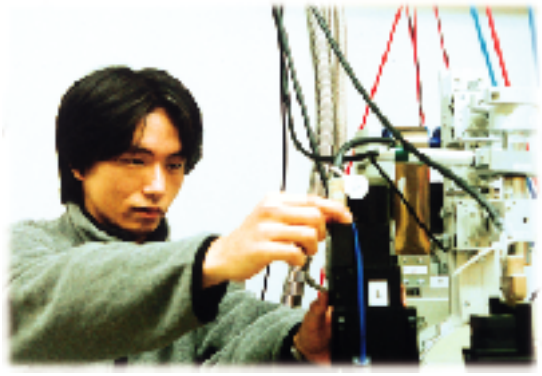

References

[1] A. N. Mansour *et al.*, J. Electrochemical Soc. **146**(8) (1999) 2799.

[2] I. Nakai *et al.*, J. Power Sources **68** (1997) 536.

[3] I. Nakai and T. Nakagome, Electrochemical and Solid-State Lett. **1** (1998) 259.

[4] T. Nonaka, C. Okuda, Y. Ukyo and T. Okamoto, J. Synchrotron Rad. **8** (2001) 869.

Takamasa Nonaka

TOYOTA Central R & D Labs., Inc.

E-mail: nonaka@mosk.tytlabs.co.jp

GRAZING INCIDENCE X-RAY FLUORESCENCE OF MAGNETIC MULTILAYERS

In recent years, much activity has been devoted to the development of giant magnetoresistance (GMR) multilayers used in the MR head for high-density magnetic recording.

X-ray reflectometry has been applied to the analyzes of ultrathin multilayer (approximately 10-layer) structures such as film thickness, density, interfacial roughness, or the existence of mixing layer. However, since this method evaluates the layer profile by examining electron density as manifested by refractive index for each layer, the spin-valve components consisting of CoFeB, Cu and NiFe are difficult to distinguish since their atomic numbers, and densities, which directly relate to their refractive indices are nearly identical. In addition to that, the method cannot provide the direct information regarding isolated elements such as the diffusion of specific atoms at the layer boundary.

To solve this problem, we developed a grazing incidence X-ray fluorescence (GIXF) techniques using wavelength dispersive (WD) equipment [1].

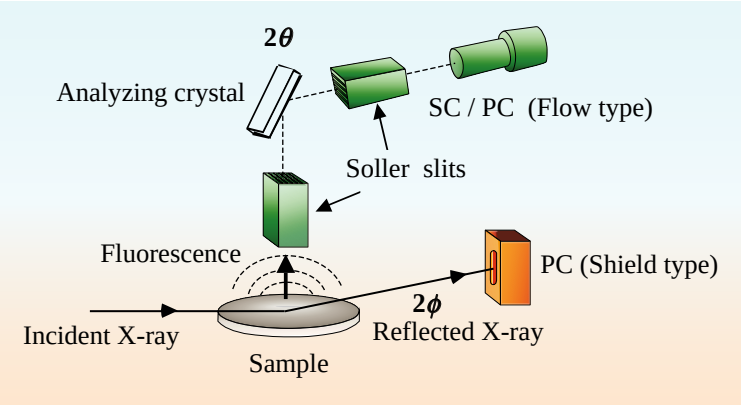

Fig. 1. Schematic drawing of the grazing incidence X-ray fluorescence configuration. Fluorescence emission from the sample were detected by the wavelength dispersive spectrometer using parallel optics.

Figure 1 is a schematic drawing of the measurement configuration. GIXF has been proposed to specify the composition profile for several years [2-5], but has not applied to the evaluation of real samples. This is due to the complexities in the data analysis in addition to the poor quality of the fluorescence data obtained by the energy-dispersive SSD detector, whose maximum count rate is lower than 10 kcps and possesses poor energy resolution. We overcame these difficulties using a WD detector with a high count rate and good energy resolution for measurement and incorporating the reflectivity data into the estimation of X-ray field intensity in the analysis.

The X-ray fluorescence equipment has been constructed at the undulator beamline **BL16XU** by a consortium of 13 industrial companies. This may represent the first device that can measure the fluorescent X-rays from the samples placed under the grazing or the total reflection conditions by a WD spectrometer with high detection sensitivity.

In the experiment, a spin-valve sample with a stratified structure of Ta(6)/PdPtMn(25)/ CoFeB(2)/ Cu(3)/CoFeB(2)/NiFe(4)/Ta(5)/Si-sub was measured. The number in parenthesis indicate the thickness in nm. The X-rays from the undulator were monochromatized to 16 keV. A downstream Rh-coated focusing mirror suppresses the higher harmonics, reducing background fluorescence signals from the samples. In addition, the high-energy resolution of the WD spectrometer resolved many

fluorescent peaks from the elements in the sample, as shown in Fig. 2. These features could not be attained by the energy dispersive measurements or by the conventional WD equipment using continuous X-rays in the laboratory.

In the angle resolved measurements, a non-overlapping peak of fluorescent X-rays for each element was chosen and the Bragg angle of the analyzing crystal was set at the peak. The results of a grazing angle scan for elements corresponding to each layer up to 0.7 degrees are shown in Fig. 3. The reflectivity was also recorded as shown in Fig. 4. The fluorescence intensity shows a clear oscillation that originates from the standing wave of X-rays generated by the interference inside the layers.

In the analysis, we extended the optimization program developed for the X-ray reflectivity, which based on the layered model of Vidal & Vincent [6], to calculate the energy flow of X-rays in the film from which the fluorescence yield can be calculated. The fluorescence profiles from each element and the reflectivity profile were simultaneously optimized to the layered model. In the analysis, layers with a similar density of different elements are resolved from the constraints on fluorescence yield for the elements. The

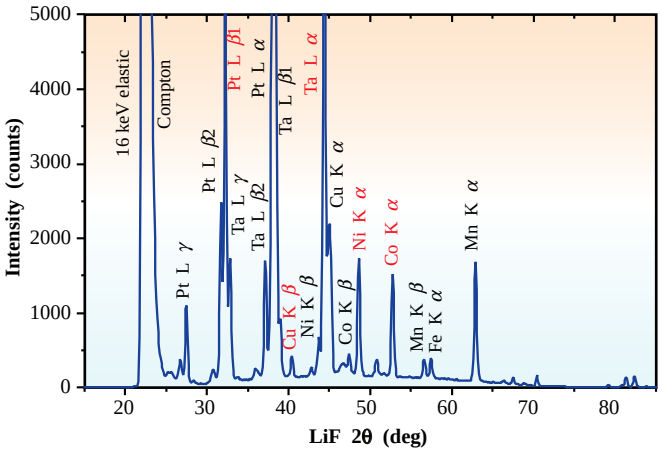

Fig. 2. Fluorescence peaks seen by the energy scan of the GMR multilayer with grazing angle of 1.5 deg.

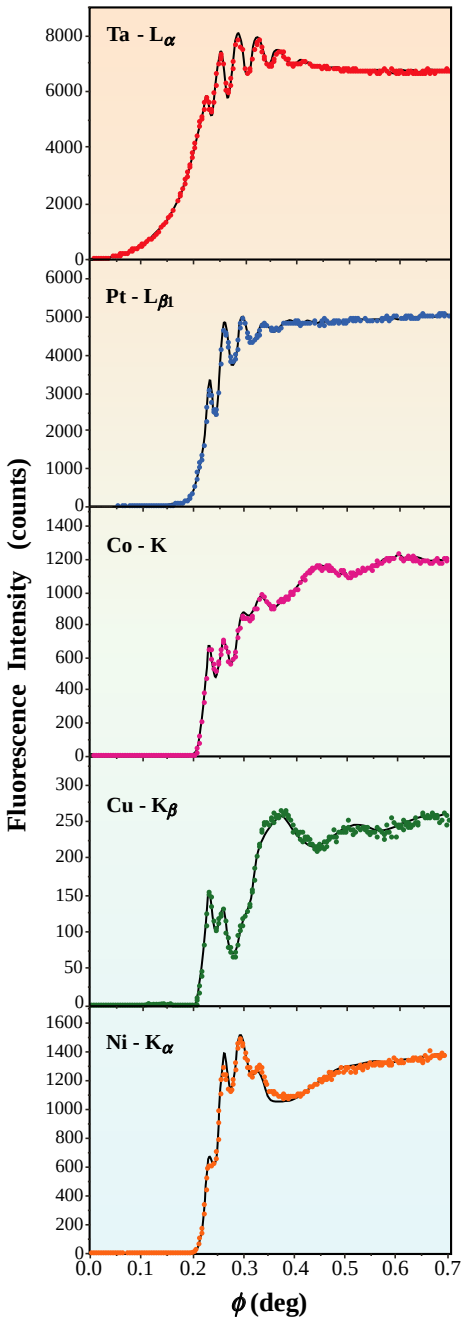

Fig. 3. Grazing angle dependence of fluorescence yields for the element corresponding to each layer. The solid line represents the calculation based on the layered model.

calculated profiles reproduce the complex fluorescence profile very well, as indicated by the solid line in Fig. 3 and Fig. 4. The reconstructed layer profile of the sample from GIXF analysis is shown in Fig. 5.

In summary, a new WD-GIXF method has been developed in which the atomic profiles of samples can be estimated and applied successfully in order to evaluate the complex GMR spin-valve samples. We succeeded in observing the change of a layered structure after thermal annealing by applying this method [7].

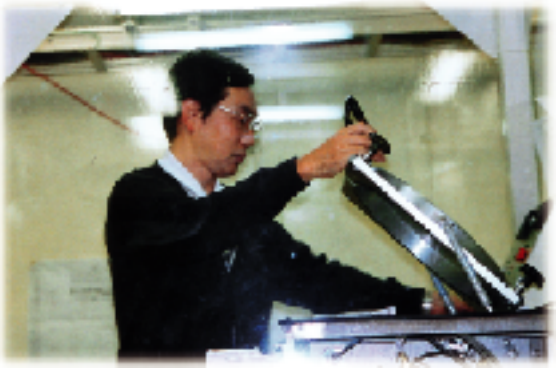

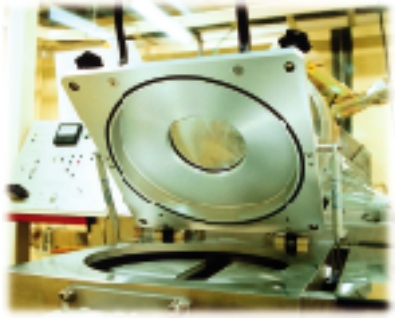

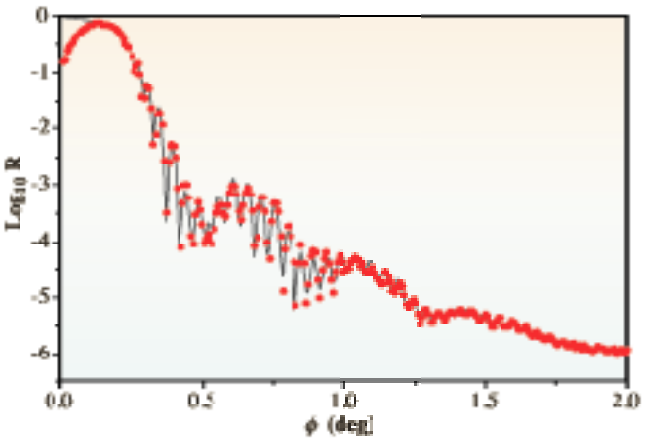

Fig. 4. Reflection profile of the GMR sample. The solid line shows the result of a calculation optimized with the fluorescence yield.

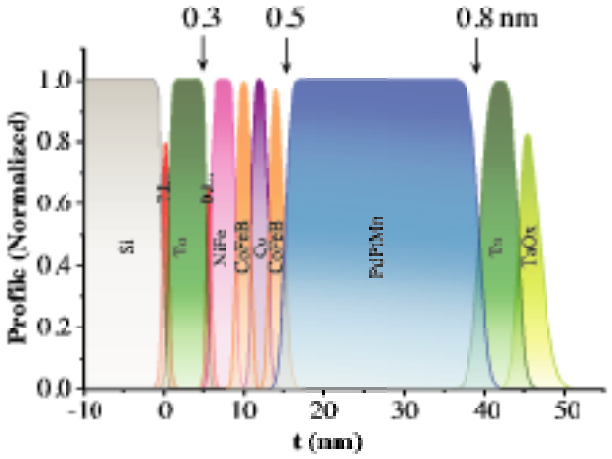

Fig. 5. Layer profile of the sample reconstructed from the results of GIXF analysis, where T.L. is the transition layer and D.L. is the dead layer introduced to reproduce the measured data. Numbers with arrow indicate the interfacial roughness.

Naoki Awaji

Fujitsu Laboratories LTD.

E-mail: awaji@ccg.flab.fujitsu.co.jp

References

[1] N. Awaji *et. al.*, Jpn. J. Appl. Phys. **39** (2000) L1252.

[2] A. Krol *et. al.*, Phys. Rev. B **38**(1988) 8579.

[3] D.K.G. de Boer, Phys. Rev. B **44** (1991) 498.

[4] A. Iida, Adv. in X-ray Anl. **35** (1992) 2.

[5] K. Sakurai, SR Sci. & Technol. Info., JASRI, No.2, **6** (1996) 2. (in Japanese)

[6] B. Vidal and P. Vincent, Appl. Opt. **23** (1984) 1794.

[7] N. Awaji, K. Nomura and S. Komiya, to be submitted in Jpn. J. Appl. Phys.

LARGE-AREA X-RAY TOPOGRAPHY TO OBSERVE 300-MM-DIAMETER SILICON CRYSTALS

The manufacturing of 300-mm-diameter silicon wafers, now used as substrates for the ULSI fabrication, requires development of large-area X-ray diffraction topography with high strain-sensitivity to detect crystal imperfections. Such irregularities, *e.g.* growth striations, and surface damage may adversely affect the electrical characteristics of ULSI. Recently, we have created an experimental apparatus designed to acquire large-area topographs of silicon crystals at the second experimental hutch of beamline **BL20B2**; the set up includes the use of a horizontally-wide and monochromatic X-ray beam made possible by 200 m distance between the hutch and the bending-magnet source point [1].

Using this apparatus, we observed surface damage resulting from slicing and polishing, comparing the topographic images taken using low- (8.7 keV), medium- (21 keV) and high- (60 keV) energies X-rays [2, 3]. The p-type CZ silicon crystals used were 300-mm in diameter and 10 mm-thick with a [100] surface orientation. After slicing with a wire saw, the crystal surface was etched slightly, lapped, and then polished both mechanically and chemically.

A schematic diagram of the experimental arrangement includes a 300-mm-wide X-ray beam, monochromatized by the Si (311) double-crystal monochromator in the optics hutch (Fig. 1). This beam was incident on the sample crystal that was set on the sample stage of the horizontal-axis precision goniometer of a tangential-bar type, at a glancing angle less than 1 degree. The energy of the X-ray beam was tuned to either 8.7, 21, 57 or 60 keV by operating the double-crystal monochromator in order to acquire topographs using asymmetric reflections of 311, 511, 12 2 2 and 911.

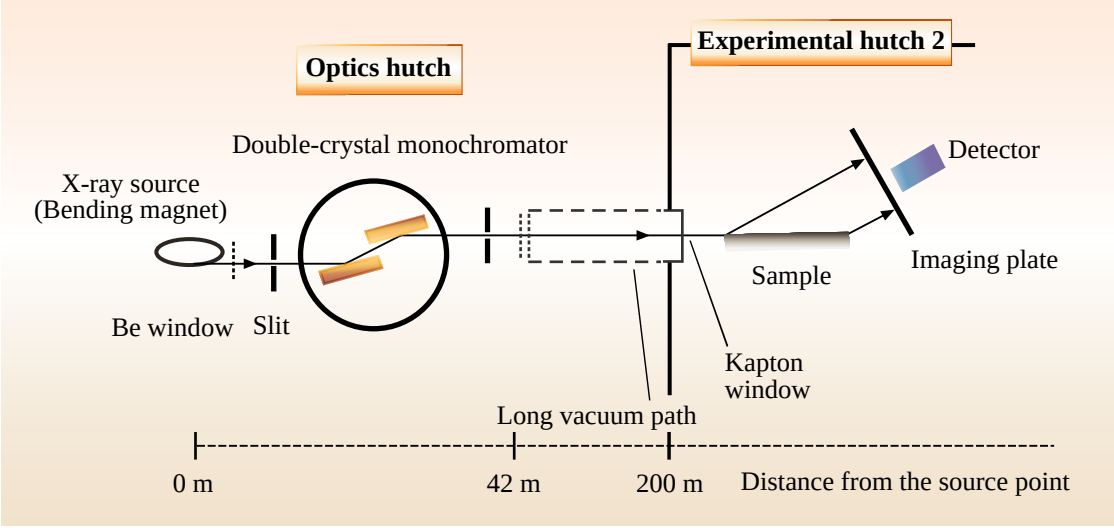

Fig. 1. Schematic diagram of the optical system for large-area X-ray diffraction topography. The 300 mm- wide and monochromatic X-ray beam, obtained at the 200 m point apart from the bending-magnet source, was used to acquire topographs of a 300-mm-diameter silicon crystal sample.

Rocking curves were calculated for the asymmetric 311, 511 and 911 reflections at a fixed glancing angle of 1 degree on the basis of the dynamical theory of X-ray diffraction (Fig. 2). The maximum values of the gradient at the low-angle side of the curves are 0.148, 0.761 and 4.552 arcsec^{-1} for the 311, 511 and 911 reflections, respectively. The curve for the asymmetric 12 2 2 reflection was similar to that for the asymmetric 911 reflection. These results indicate that use of the higher-order asymmetric reflection of higher-energy X-rays improves the strain sensitivity, when the topographs are taken at the angle position of half-peak intensity.

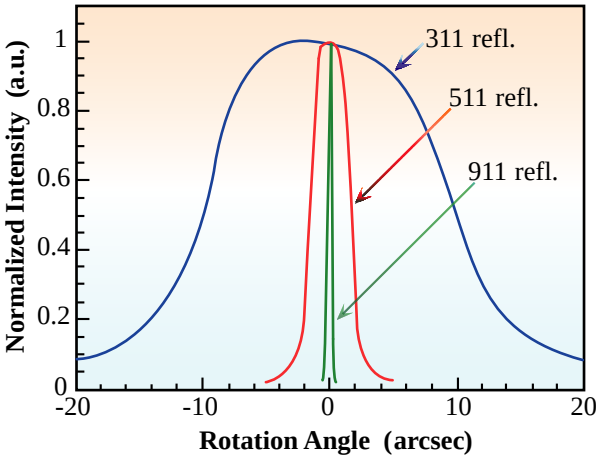

Fig. 2. Calculated rocking curves from (100) silicon. Incident angle was fixed at 1 degree; the asymmetric 311, 511 and 911 reflections used 8.7, 21 and 60 keV X-rays, respectively.

Topographs, recorded on an imaging plate (IP) with a pixel size of 100 μm^2, were reconstructed with an IP reader. The two topographs of a sliced and slightly etched sample (Fig. 3a and b) were taken using the asymmetric 511 reflection of 21 keV X-rays at the lower angle side and at the higher angle side of the rocking curve; modification by image processing then created a circular sample shape. Long line images with equal intervals were identified as saw marks caused by slicing. The reversal of image contrast within the same areas of the two topographs demonstrates the presence of minute and wide strain-fields in the surface region of the sample.

Using the asymmetric 12 2 2 reflection of 60 keV X-rays with higher strain-sensitivity, we examined minute residual damage caused by polishing. Circular defect patterns and microscratch images (Fig. 4) were observed; this detection method allowed the improvement of current polishing procedures.

The use of extremely asymmetric reflections of a

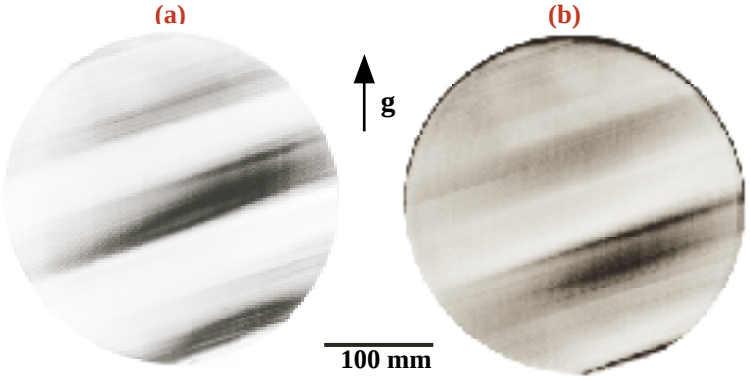

*Fig. 3. X-ray topographs of a 300-mm-diameter CZ silicon crystal after slicing, followed by slight etching. (**a**) and (**b**) were taken using the asymmetric 511 reflection of 21 keV X-rays at the low-angle side and the high-angle side of the rocking curve, respectively. The arrow designates the diffraction vector **g**.*

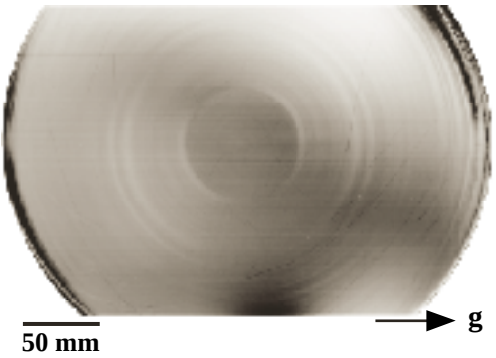

Fig. 4. X-ray topograph taken with the asymmetric 12 2 2 reflection of 60 keV X-rays after a polishing test. Circular patterns were identified as surface damage caused by polishing. The arrow designates the diffraction vector ***g****.*

300-mm-wide and monochromatic X-ray beam enables the acquisition of X-ray topographs all over a 300-mm-diameter silicon crystal, using only a single X-rays exposure. This technique will be useful in clarifying impurity inhomogeneity, dubbed growth striations, within 300-mm-diameter CZ silicon crystals.

References

[1] Y. Chikaura *et al*., to be published in J. Phys. D: Appl. Phys. **34** (2001).
[2] S. Kawado *et al*., Progr. and Abstr. of 5th Biennial Conf. on High Resolution X-ray Diffraction and Topography (X-TOP 2000), Sep. 2000, Poland, p.107.
[3] S. Kawado *et al*., submitted to Jpn J. Appl. Phys.

Seiji Kawado[a], Satoshi Iida[b] and Yoshinori Chikaura[c]

(a) Rigaku Corporation
(b) Toyama University
(c) Kyushu Institute of Technology

E-mail: kawado@rigaku.co.jp

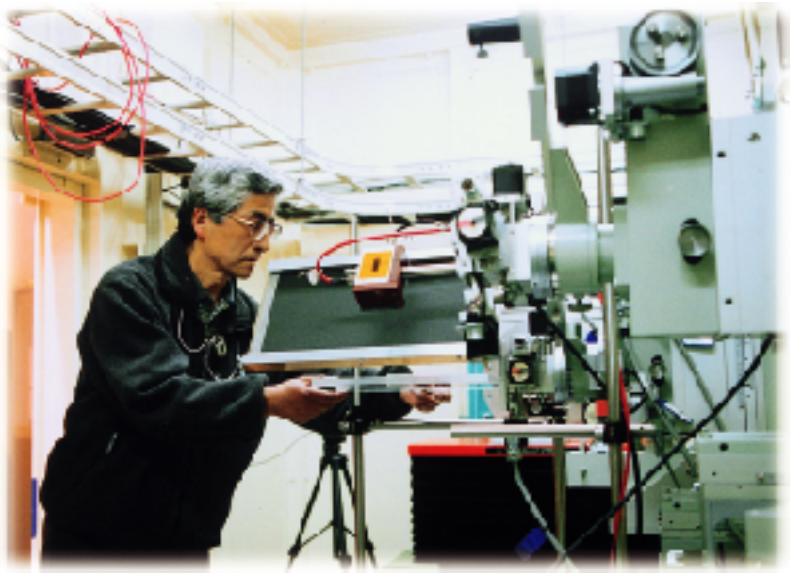

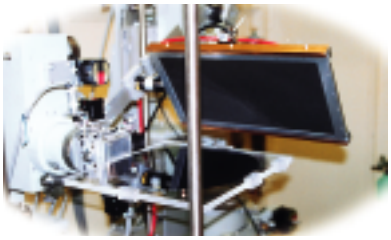

HIGH-RESOLUTION MICROBEAM X-RAY DIFFRACTOMETRY APPLIED TO NARROW-STRIPE SELECTIVE MOVPE GROWN InGaAsP/InP LAYERS

The fabrication of advanced integrated multi-quantum-well (MQW) waveguide devices and high-performance laser diodes requires extremely uniform device characteristics. The selective metal-organic vapor phase epitaxial (MOVPE) growth of InGaAsP layers between a pair of dielectric stripe masks on a narrow stripe region (*e.g.* 0.5 to 2 μm wide) in the [011] direction of an InP(100) substrate (Fig. 1) is an attractive methods to fabricate photonic integrated devices. The multilayer thickness, composition, and lattice strain can be varied between different regions of the same wafer through variation of the dielectric mask width. In addition, an ideal optical waveguide structure surrounded by (100) and (111) crystal planes, can be formed automatically without the necessity of semiconductor etching. Utilizing this growth technique, however, the lattice strain of the selective MOVPE layers is difficult to control. High-resolution X-ray diffraction (HRXRD), possessing a high-angle and/or high-reciprocal space resolution, usually used as a strain characterization tool for epitaxial layers grown onto full wafers, cannot be used here due to insufficient spatial resolution. HRXRD with micrometer-scale spatial resolution is needed.

Recently, we developed an X-ray microbeam, possessing low angular divergence and narrow energy bandwidth, through the use of perfect-crystal X-ray optics in conjunction with undulator radiation X-rays from the synchrotron light source [1]. These features of the X-ray microbeam are suitable for HRXRD measurements. We have applied this X-ray microbeam to the strain analysis of narrow-stripe selective (NS) MOVPE InGaAsP layers, grown on 1.7-μm-wide stripe regions of InP between a pair of SiO_2 mask stripes, varying width from 4 to 40 μm.

MOVPE growth was performed on a patterned substrate. Pairs of 100-nm-thick SiO_2 mask stripes

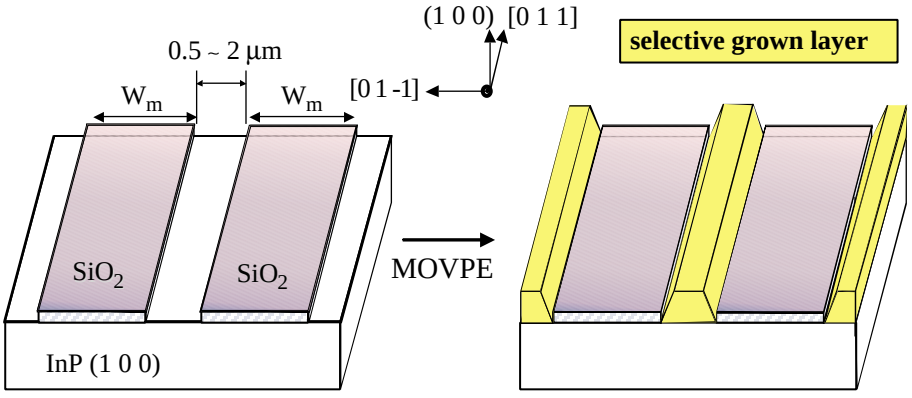

Fig. 1. Schematic figures of the InGaAsP layers grown by NS MOVPE.

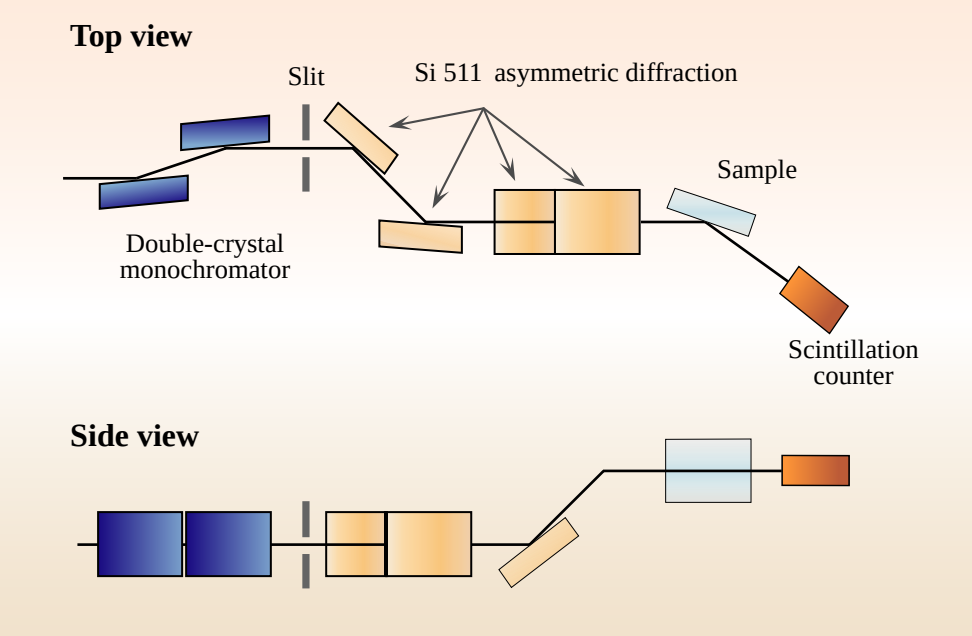

Fig. 2. The experimental arrangement of the optics set up at BL24XU.

were patterned along the [011] directions on an n-type InP(100) substrate. The mask stripe width (Wm) was varied from 4 to 40 μm while maintaining an open stripe width of 1.7 μm. Open stripe regions were separated by 300 μm. InGaAsP layers and InP cap layers were grown on the unmasked regions by atmospheric-pressure MOVPE.

The experimental arrangement (Fig. 2) was set up at the Hyogo beamline **BL24XU**, using a high-precision goniometer system with both horizontal and vertical rotation axes [1]. Producing an X-ray microbeam with low angular divergence and narrow energy bandwidth, we adopted the two-dimensional condensation of undulator radiation 15 keV X-rays, through successive asymmetric diffraction. This method obtained a beam of approximately 7.3 μm and 6.4 μm at the sample position in the horizontal and vertical directions, respectively. The estimated angular divergence was 7.7 μrad in the horizontal and 5.3 μrad in the vertical directions, respectively, with an estimated energy bandwidth of 66 meV. We performed HRXRD measurements using the microbeam in conjunction with a high-precision θ-2θ goniometer with submicron-precision XYZ sample positioning stages. Rocking curves around the InP 400 diffraction peaks were measured using angular steps of 0.004°.

The rocking curves from the NS MOVPE grown regions and the non-selective growth region of the sample revealed clear peak shifts in the InGaAsP layers as the mask width increased from the higher angle side to the lower angle side of the substrate peaks (Fig. 3). Analysis of these rocking curves enables the precise determination of strain (Δd/d) (Fig. 4), important for creating a well-controlled waveguide structure with excellent crystal quality.

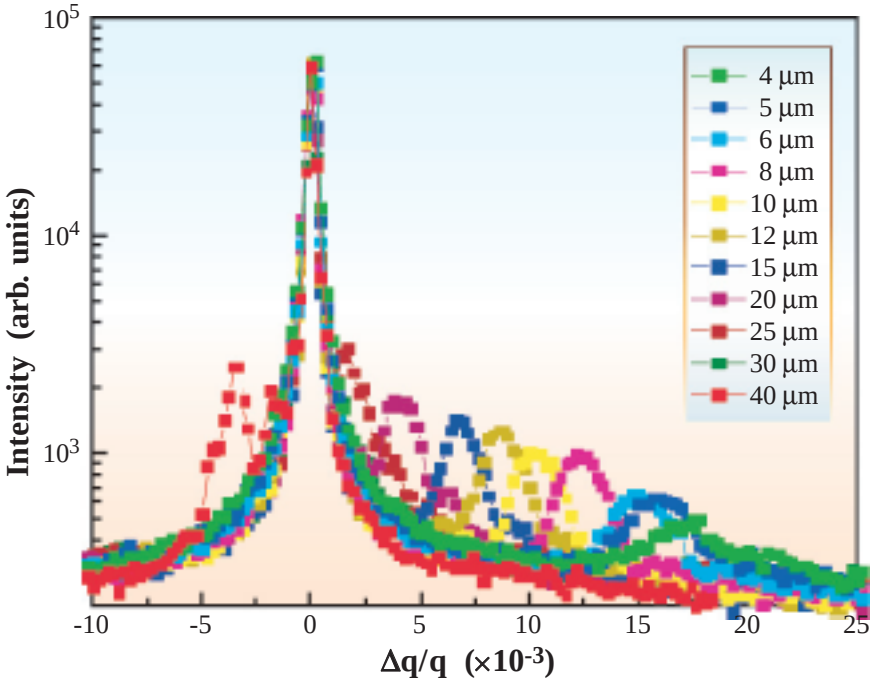

Fig. 3. A series of the rocking curves from the NS MOVPE growth regions.

Shigeru Kimura

Fundamental Research Laboratories,
NEC Corporation

E-mail: s-kimura@bl.jp.nec.com

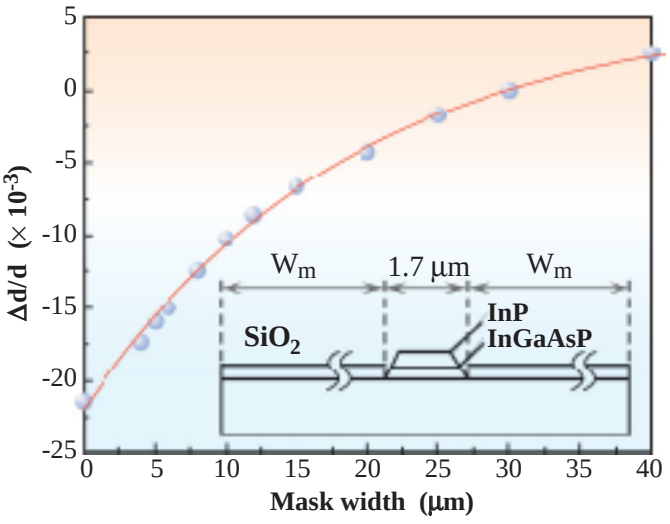

Fig. 4. Mask width dependence of the perpendicular strain Δ/Δd.

References

[1] Y. Tsusaka *et al.*, Jpn. J. Appl. Phys. **39** (2000) L635.

[2] Shigeru Kimura, Hidekazu Kimura, Kenji Kobayashi, Tomoaki Oohira, Koich Izumi, Yusataka Sakata, Yoshiyuki Tsusaka, Kazushi Yokoyama, Shingo Takeda, Masafumi Urakawa, Yasushi Kagoshima and Junji Matsui, Appl. Phys. Lett. **77** (2000) 1286.

Accelerators & Beamlines Frontiers

Beam Performance and Upgrades of the Storage Ring

Installation of Long Magnet-free Straight Sections

The initial lattice structure (Phase-I optics) of the SPring-8 storage ring was composed of 48 unit cells (DBA lattice). The ring has four long straight cells with missing bending magnets at intervals of eleven cells. In the summer of 2000, the long straight cells were changed into the long magnet-free straight section of approximately 29 m long by re-arrangement of the quadrupole and sextupole magnets. The new lattice structure and its optics (Phase-II optics) are shown in Fig. 1 together with the Phase-I lattice.

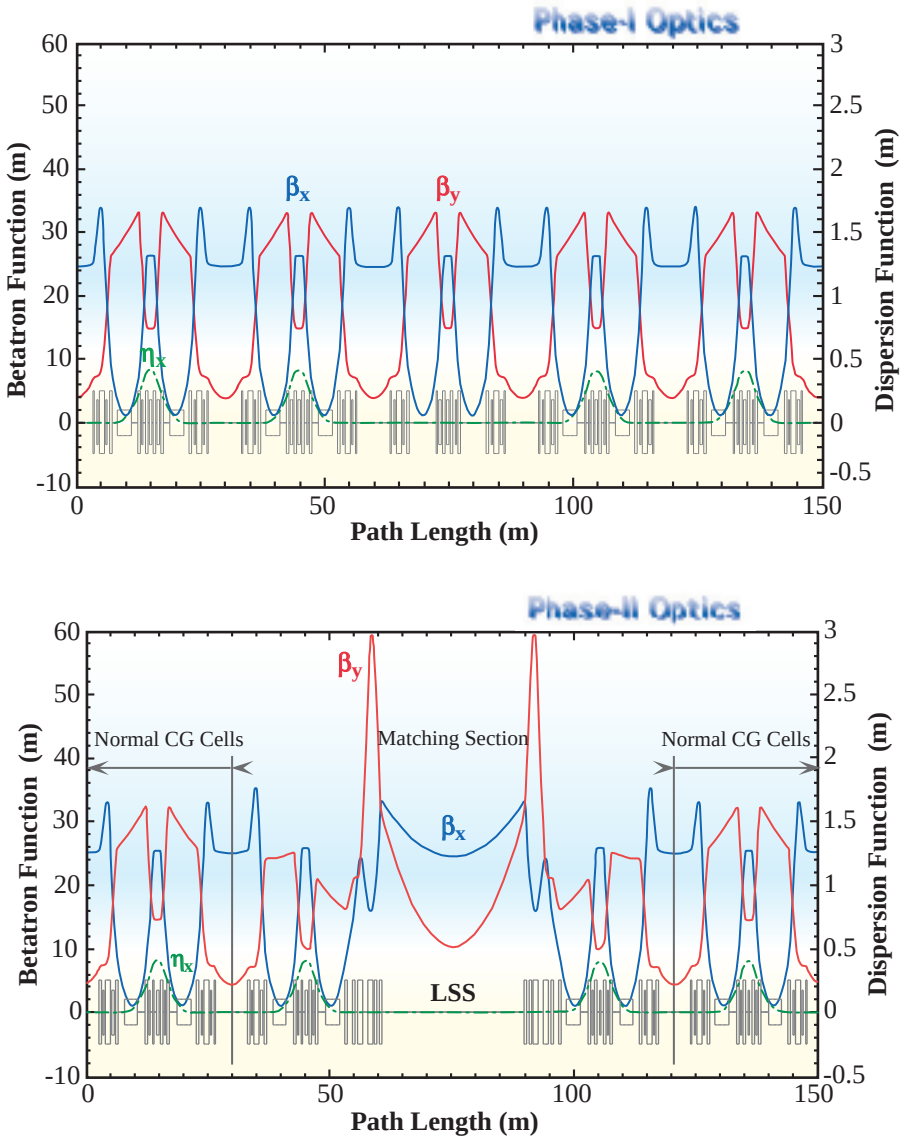

Fig. 1. Lattice structure and typical optical functions for Phase-I and Phase-II optics.

The beam commissioning of this Phase-II optics was started on August 28th, 2000 and within the same day, the first beam storage of 0.22 mA was achieved by on-axis-like injection. The commissioning was successfully completed in about three weeks, and user service operation commenced in the beginning of October.

The beam performance achieved in the Phase-II optics is similar to that of the Phase-I except for the beam lifetime. The over-all beam performances (Table 1) demonstrates that the beam lifetime is still improving, resulting from the beam self-cleaning effects of the photon absorbers installed in the new vacuum chambers. In December 2000, the beam lifetime achieved more than 100 hours for a total beam current of 100 mA in multi-bunch mode.

Other Research and Development

The following research and developments were performed:

- Improvement of the orbit stability.
  Orbit oscillation due to current fluctuations (1 Hz) in the main quadrupole magnets power supplies, and synchrotron oscillation (2 kHz), resulting from RF noise in the synthesizer, were eliminated.
- Analysis of the error field in the storage ring and the fine tuning of optical functions.
- Analysis of beam instability, such as fast ion trapping.
- Beam loss analysis in the injection process to realize a top-up operation.
- Emittance measurement.
  The beam size of the SPring-8 storage ring has been measured utilizing a newly developed, two dimensional interferometer, employing the visible part of synchrotron radiation emanating from a bending magnet. The optical system is shown in Fig. 2 and the typical two-dimensional interference pattern in Fig. 3. The measured horizontal and vertical beam size is typically 150 μm and less than 20 μm, respectively.

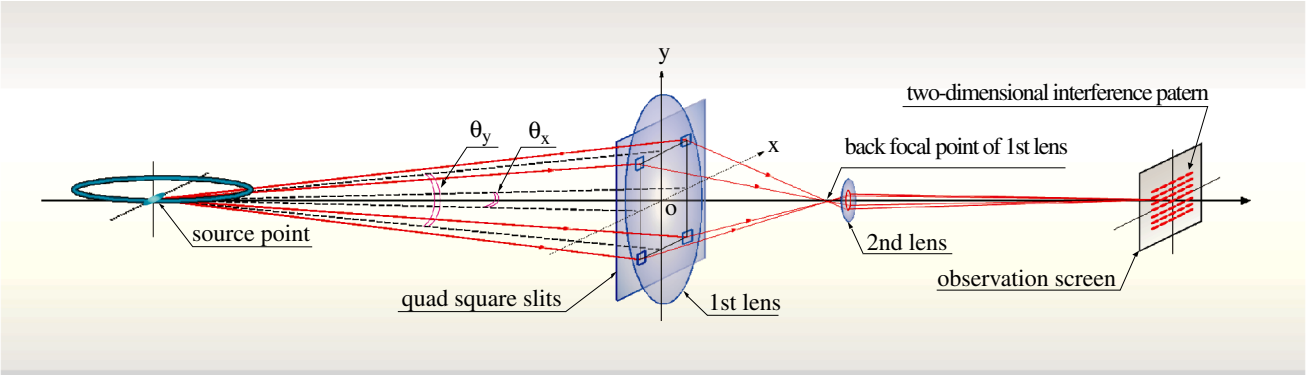

Fig. 2. Optical system of the two-dimensional interferometer.

Table 1: *Beam Performance*

	Designed values	Achieved values		
		Phase-I ring		Phase-II ring
	Hybrid / HHLV / 30m-LSS	Hybrid	HHLV	New Optics
Energy	8 GeV	8 GeV	8 GeV	8 GeV
Circumference	1436 m	-	-	-
Number of bucket	2436	-	-	-
Revolution time	4.79 ms	-	-	-
Symmetry	24 / 48 / 4	24	48	4
(β_x / β_y) at ID section		(24 / 10), (1 / 8)	25 / 4	(24.35 /5.77) / (23.42 /14.44)
Current: single bunch	5 mA	16 mA	16 mA	-
multi bunch	100 mA	100 mA	100 mA	100 mA
Bunch length (FWHM)	36 ps	36 ps [1]	32 ps [2]	-
Emittance	6.99 / 6.3 / 6.6 nm·rad	6.8±0.5 nm·rad [3]	6 nm·rad [3]	5.9 nm·rad [3]
Tunes (ν_x / ν_y)		51.16 / 16.36	43.16 / 21.36	40.15 / 18.35
Chromaticities (ξ_x / ξ_y):				
natural	(-115.9/-40.0)/(-105.9/-51.2)/(-90.3/-40.7)			
operation		3.2 / 3.9	7.0 / 4.0	7.0 / 6.0
Momentum acceptance	~ 2% [1]	1.3% [1]	1.9% [1] (2.8% [2])	2.0% [2]
Energy spread ($\Delta E/E$)	0.0011	0.0012	0.0011	0.0011
Coupling	less than 10%	≤ 0.06% [4]	≤ 0.04% [4]	~ 0.06% [4]
Lifetime: 100 mA (multi bunch)	24 hr	~ 70 hr [5]	~ 140 hr [6]	~ 110 hr [6]
1 mA (single bunch)	-	~ 5 hr [1]	~ 11 hr [1] (~25 hr [2])	~ 22 hr [2]
COD: horizontal (rms)	-	< 0.1 mm	< 0.1 mm	< 0.1 mm
vertical (rms)	-	< 0.1 mm	< 0.1 mm	< 0.1 mm
Beam size at ID section:				
horizontal (rms)	-	400 μm / 86 μm	390 μm	380 μm
vertical (rms)	-	6.7 μm / 6 μm	3 μm	4.5 μm
Residual dispersion at non-dispersive section:				
horizontal (rms)	0	9.8 mm	7.0 mm	4.4 mm
vertical (rms)	0	2.7 mm	4.5 mm (1.1 mm [7])	1.3 mm [7]
Orbit stability (tune harmonics)				
horizontal (standard deviation)	-	1.1 μm	0.7 μm	1.3 μm
vertical (standard deviation)	-	0.7 μm	0.35 μm	0.35 μm

[1] Vrf=12 MV [2] Vrf=16 MV [3] calculated by using designed β-function [4] single resonace approximation
[5] 2/3-filling, Vrf=12 MV [6] 24/29-filling, Vrf=16 MV [7] with correction by 24 skew Q's

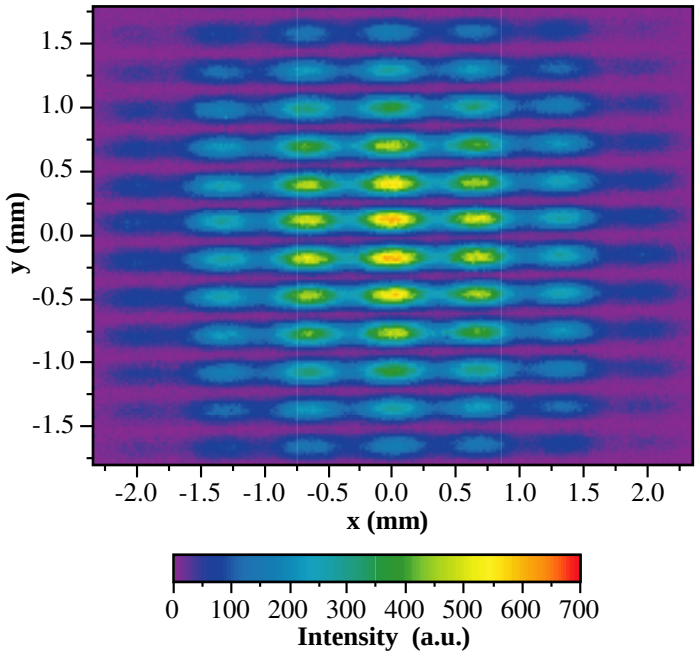

Fig. 3. Two-dimensional interference pattern.

Developments and Upgrades of Linac

Installation of ECS and Single Pass BPM

An energy compressor system (ECS) was installed at the end of the linac to reduce the beam energy spread resulting from beam loading and the energy fluctuation. As a preliminary result, a reduction rate of 50% was achieved in the energy spread.

To improve the orbit stability, 12 single pass BPM's with a position resolution of a few tenth micron (2σ) were installed in the Linac. Operation of this new BPM system will begin in the autumn of 2001.

Development of RF-gun

To realize high quality electron beam of 1 nC, 1 π mm·mrad with bunch length of sub-psec, a development of an RF-gun was carried out in the test bench and high-power RF, up to 27 MW, was fed into the cavity. The maximum electric-field gradient of 140 MV/m is reached on the cathode and the electron beam of 2 nC per bunch was accelerated up to 3.2 MeV. The minimum normalized emittance of 17 πmm·mrad was obtained at 90 MV/m and 0.8 nC/bunch. Also, a three-dimensional beam simulation code has been developed to understand the formation of beam emittance in the RF-gun.

Noritaka Kumagai
SPring-8 / JASRI

27 m Long In-vacuum Undulator

Among third-generation light sources, SPring-8 is distinguished by the presence of four long straight sections allowing the achievement of super brilliant synchrotron radiation. During summer shutdown of 2000, a lattice of the storage ring was modified to create magnet free 30 m straight sections [1]. At the same time, the first long insertion device was installed at the X-ray beamline BL19LXU. The first device is an in-vacuum undulator with a 32 mm magnetic period similar to the SPring-8 standard type in-vacuum undulator. Main parameters of the undulator are detailed in Table 1. The net length of the undulator magnet is 25 m and all magnet blocks are arranged continuously. This is one of the advantages of in-vacuum devices. In the construction of long insertion devices, the magnets of the out of vacuum insertion device are separated by flanges at the vacuum chamber connection points as shown in Fig. 1 (b). On the other hand, for in-vacuum devices, the vacuum chambers are connected externally using bellows, therefore, there is no gap between magnet arrays (Fig. 1 (a)). As a result, all radiations emanating from each magnet array are superposed in phase; therefore, no complicated phase matching techniques are necessary.

The 27 m undulator consists of 5 segments (Fig. 2), each possessing a similar mechanical structure to a 4.5 m long in-vacuum undulator, which has been successfully operated for years at SPring-8 [2]. Each segment has an individual undulator gap driving system, controlled simultaneously by one signal since magnet arrays are mechanically connected between segments. The segment is also an unit to carry out magnetic field measurements [3] and transportation. The five segments were transported independently to the storage ring, then assembled together inside the ring tunnel. Figure 3 is a photograph of the installed undulator in the SPring-8 storage ring.

Table 1. Parameters of the 27 m long in-vacuum X-ray undulator for BL19LXU

Type	Pure permanent magnet (halbach)
Periodic length	32 mm
Number of periods	780
Gap range	12 ~ 50 mm
Maximum K	1.76 at 12 mm gap
E_{1st}	7.4 ~ 18 keV

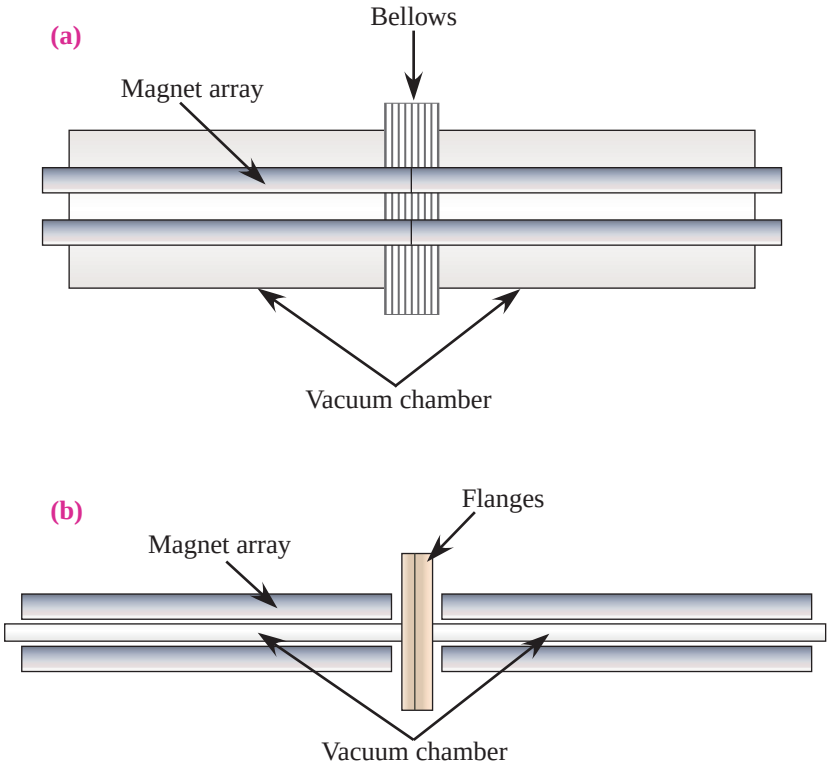

Fig. 1. Schematics of the magnet array connections utilized for the long undulator construction, ***(a)*** *in-vacuum device,* ***(b)*** *out of vacuum device.*

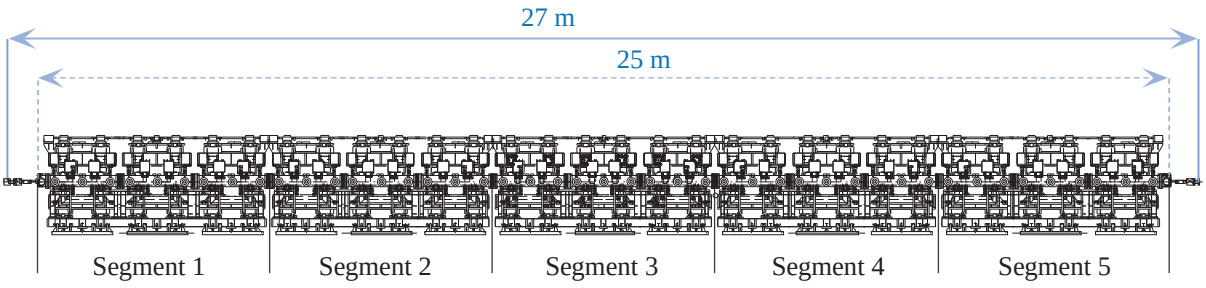

Fig. 2. Schematic of the 27 m undulator consisting of 5 segments.

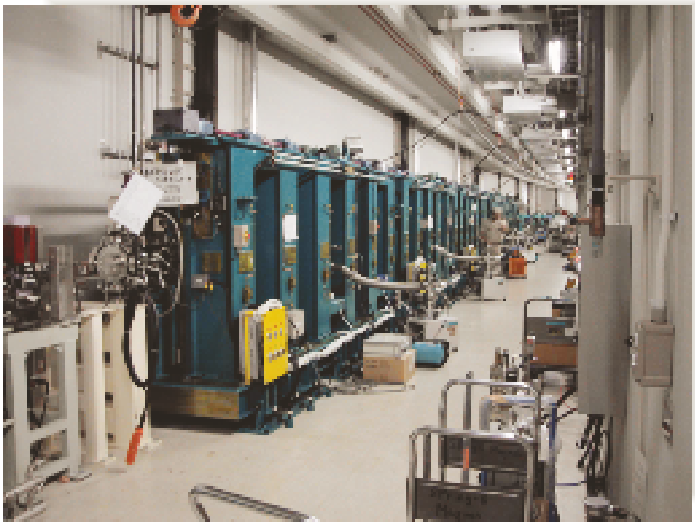

Fig. 3. 27 m in-vacuum undulator installed in the SPring-8 storage ring.

The beamline was commissioned in October 2000, and the first undulator radiation was observed on October 25th (Fig. 4). The brilliance of the 27 m undulator was increased approximately 4~5 times from that of 4.5 m undulators. The measured spectrum at 12 mm undulator gap utilizing a front-end (FE) slit aperture of 0.2 mm $\times$ 0.2 mm [4] demonstrated that 50% of the calculated flux was obtained under these conditions (Fig. 5). The undulator radiation Bose degeneracy surpasses one during high peak current operation mode of the ring. Experiments using high photon flux and spatial coherency of the undulator radiation will dominate the use of the beamline.

The success of the 27 m undulator will be the basis of the upcoming self-amplified spontaneous emission (SASE) based FEL project, which requires the precise control of the electron beam inside the undulator. For example due to its long length, we have observed the effect of a weak uniform field of 0.1 G, such as the earth field, on the undulator spectrum. Together with the techniques of the field alignment and construction, the experience in using the 27 m in-vacuum undulator forms the next step in pursuit of innovative light sources.

Fig. 4. First observation of the undulator radiation at BL19LXU.

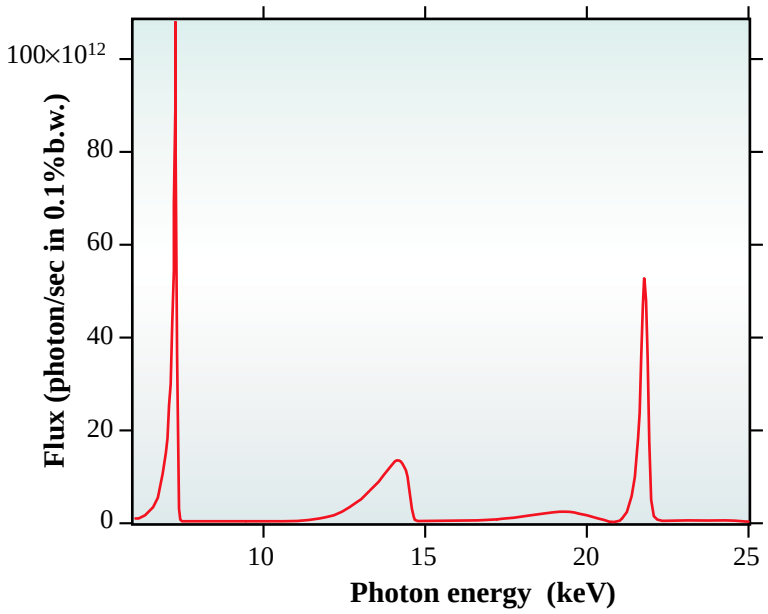

Fig. 5. Undulator spectrum measured at 12 mm gap with a 0.2 mm × 0.2 mm FE slit.

References

[1] N. Kumagai, SPring-8 Information, No.1, **6** (2001) 5.

[2] H. Kitamura, J. Synchrotron Rad. **7** (2000) 121.

[3] T. Tanaka *et al.*, SRI2000, to be published in Nucl. Instrum. Meth.

[4] T. Ishikawa *et al.*, to be published in J. Jpn. Soc. for Synchrotron Rad. Res.

Toru Hara and Hideo Kitamura
SPring-8/RIKEN•JASRI

New Detectors in SPring-8

The notable new detectors at SPring-8, added in 1999/2000, are follows.

Fast CCD Camera

A fast CCD detector was introduced at the high flux beamline (BL40XU). The detector utilizes a fast camera, consisting of three interline CCD cameras arranged on the three sides of a prism to receive the same image, just as in the case of 3-CCD color video camera. Each camera operates in an exposure-readout cycle. By shifting this cycle, it is possible to achieve a frame rate three times higher than is possible with a single CCD. Using a full frame size of 640 (horizontal) × 480 (vertical) pixels, the frame rate is 290 per second. This rate can be further increased by reducing the number of vertical pixels. The image is then read and digitized into 10 bits. A large frame memory can store the images continuously up to more than 20 sec.

To demonstrate the high frame acquisition rate, a drop of milk falling into milk was recorded (by courtesy of Hamamatsu Photonics, K.K.). It is possible to see how milk is splashed in small drops (Fig. 1).

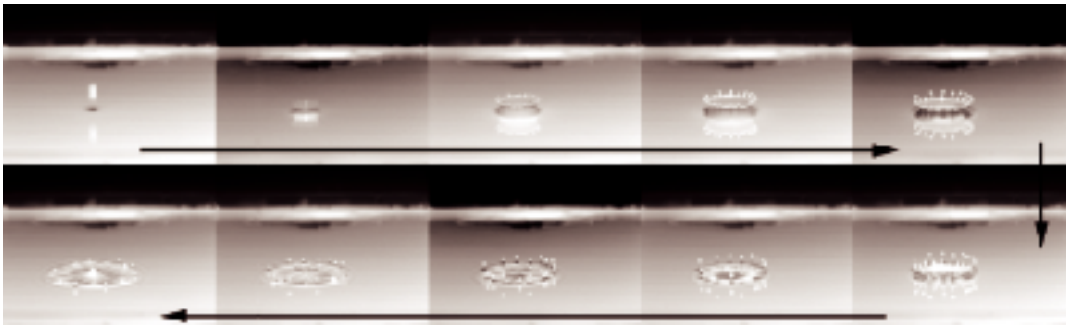

Fig. 1. The small drops created by the splash of the milk droplet are easily discernible by this high frame rate.

The detector is used with a Be-windowed X-ray image intensifier which uses a short-decay phosphor (P46) in the output window. The persistence is negligible, even in experiments with a time resolution greater than 1 msec. The 15 cm diameter of the X-ray image intensifier provides a spatial resolution of 0.22 mm. The detector system is currently used in X-ray diffraction experiments on skeletal muscle at a time resolution of 530 μsec. Frame timing signal is used to synchronize the detector with the other equipments.

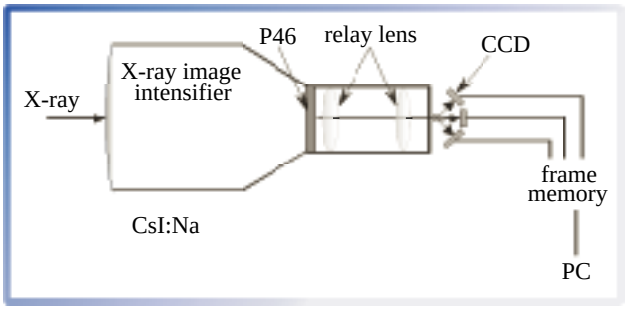

High-speed Imaging Plate Detector

At the protein crystallography station of RIKEN beamline I (BL45XU), a high-speed imaging plate detector (RAXIS V) was developed and installed in collaboration between RIKEN and RIGAKU Co. This detector was designed to reduce the readout time, in order to match to the short-exposure. The detector, containing three-IPs, performs the exposure, reading and erasing of the three-IPs at the same time, to allow quick repetition of the continuous readout. The stored image is read from the IP using a new double-beam helical-scanner, capable of reading out a 400 mm $\times$ 400 mm, 100 μm pixel image in less than 50 seconds. The turn-around time is, therefore, shortened to only 65 sec, in comparison to the ~4 min necessary for the previous model (RAXIS IV++). The large detection area and wide dynamic range of an image plate is especially advantageous over CCD-based detectors when collecting high resolution crystallographic data and accurate measurements of diffraction intensities. The detector will be also utilized in other protein crystallography beamlines in the future.

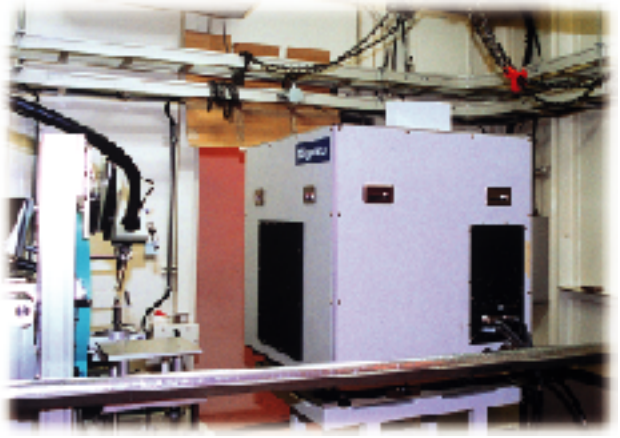

Detector Development Projects

A one-dimensional microstrip germanium detector [1] with 128 strips is now in trial operation at BL08W. A new readout electronics using VLSI technology is employed. The detector is being developed in a collaboration between the detector group of JASRI and the users of the beamline. The final goal of this development project is a detector with 512 strips, which will be a powerful tool to measure Compton scattering with high efficiency.

References

[1] SPring-8 Research Frontiers 1998/1999, p. 98.

Naoto Yagi
SPring-8 / JASRI

Facility Status

Machine Operation

The beam commissioning of the SPring-8 storage ring begun on March 13, 1997. The operation statistics for the last four years are shown in Fig. 1. In 2000, the SPring-8 storage ring was operated on three- or four-week period for one cycle. The total operation time was approximately 5000 hours. About 67% of the operation time was available to the users and the remaining 33% was dedicated for: (i) the machine study, (ii) the machine and beamline tuning, (iii) the commissioning of the new optics (Phase-II optics), and (iv) the commissioning of new photon beamlines.

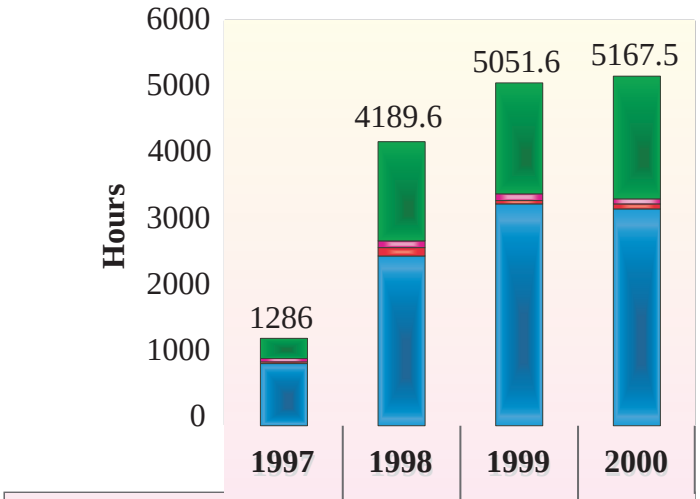

	1997	1998	1999	2000
Tuning (Accel.&BL)	304	1457.6	1624.2	1815
Injection	50	110	95.2	70.4
Failure	26	110	57.2	88.7
User time	906	2512	3275	3193.4

Fig. 1. Operational statistics since 1997.

Three different filling patterns were delivered to the user time; 53.5% in the multi-bunch mode operation, 30.7% in the several bunch mode such as 29 equally spaced 9-, 11- or 15-bunch trains, and the remaining 15.7% in the hybrid filling mode such as a 2/29-partially filled multi-bunch with 26-isolated bunches. For the hybrid filling mode, 1 or 1.5 mA is stored in each isolated bunch, with impurity level of 10^{-7} being routinely kept in the user time.

BEAMLINES

At SPring-8, several new beamlines are currently under construction and additional beamlines are also being considered for construction.

The beamlines at the SPring-8 Facility are categorized into three types:

- Public beamlines, constructed by SPring-8, open for public use. This category includes the R&D beamlines.
- JAERI/RIKEN beamlines, constructed by JAERI/RIKEN for their exclusive use.
- Contract beamlines, constructed by universities, institutions or industries for their exclusive use.

By the end of 2000, twenty-one public beamlines were operational and available for public use:

BL01B1	XAFS
BL02B1	Crystal Structure Analysis
BL02B2	Powder Diffraction
BL04B1	High-Temperature Research
BL04B2	High Energy Monochromatic X-ray Studies
BL08W	High Energy Inelastic Scattering
BL09XU	Nuclear Resonant Scattering
BL10XU	Extremely Dense State Research
BL20B2	Medical and Imaging Application I
BL25SU	Soft X-ray Spectroscopy of Solids
BL27SU	Soft X-ray Photochemistry
BL28B2	White Beam Topography
BL35XU	High-Energy Resolution Inelastic Scattering
BL38B1	R&D(3) (bending magnet beamline)
BL39XU	Magnetic Materials
BL40XU	High Flux
BL40B2	Structural Biology II
BL41XU	Structural Biology I
BL43IR	Infrared Materials Science
BL46XU	R&D (2) (short period in-vacuum type undulator)
BL47XU	R&D (1) (standard in-vacuum type undulator)

As of 2000, the following beamlines are nearly completed and will soon be ready for public use:

BL13XU	Surface and Interface Structures
BL19B2	Engineering Science Research
BL20XU	Medical and Imaging Application II
BL37XU	Trace Element Analysis

Of these, BL13XU, BL19B2 and BL20XU will be commissioned in April, 2001, including some public use trial. The BL37XU beamline will follow shortly after the commission of these three beamlines.

Ten beamlines have been constructed/are under construction by JAERI and RIKEN for the exclusive use of JAERI and RIKEN scientists:

BL11XU	Materials Science II (JAERI)
BL14B1	Materials Science I (JAERI)
BL19LXU	Synchrotron Radiation Physics Studies (RIKEN)
BL22XU	Materials Science III (JAERI)
BL23SU	Actinide Studies by Soft X-rays (JAERI)
BL26B1	Structural Genomics I (RIKEN)
BL26B2	Structural Genomics II(RIKEN)
BL29XU	Coherent X-ray Optics (RIKEN)
BL44B2	Structural Biology II(RIKEN)
BL45XU	Structural Biology I (RIKEN)

BL19LXU is a 30 m-long straight section beamline and the long undulator was installed after the rearrangement of the magnets in the storage ring during the summer of 2000. BL22XU is a beamline for actinide studies utilizing hard X-rays. BL26B1 and BL26B2 are beamlines that will be used for “high throughput” protein crystallography following the human genome project in 2001. BL29XU has two experimental stations, one at the standard length of 80 m, and the other located at 1,000 m from the undulator source.

Eight contract beamlines at SPring-8 are either in operation or under construction.

BL12IN	APCST ID beamline (Taiwan)
BL12B2	APCST BM beamline (Taiwan)
BL15IN	Materials Science (National Institute for Research in Inorganic Materials)
BL16XU	Materials Science (Industrial Consortium)
BL16B2	Materials Science (Industrial Consortium)
BL24XU	Multi-purpose (Hyogo Prefecture)
BL33LEP	Laser Electron Photon Studies (Osaka University)
BL44XU	Macromolecular Assemblies (Osaka University)

All beamlines are shown in the Beamline Map. We have two beamlines, a contract beamline (BL32B2) for Pharmaceutical Consortium, to be completed by the end of 2001, and a RIKEN beamline (BL17SU) for soft X-ray spectroscopy, the construction of which will begin in FY2001. The latter is positioned as an R&D beamline for ultra-high brilliance soft X-ray spectroscopy. These two beamlines are not included in the Map. Including the two accelerator diagnosis beamlines, we have forty seven beamlines, *i.e.*, more than 3/4 beamlines of sixty-two beamlines possible at SPring-8.

Tatzuo Ueki
SPring-8 / JASRI

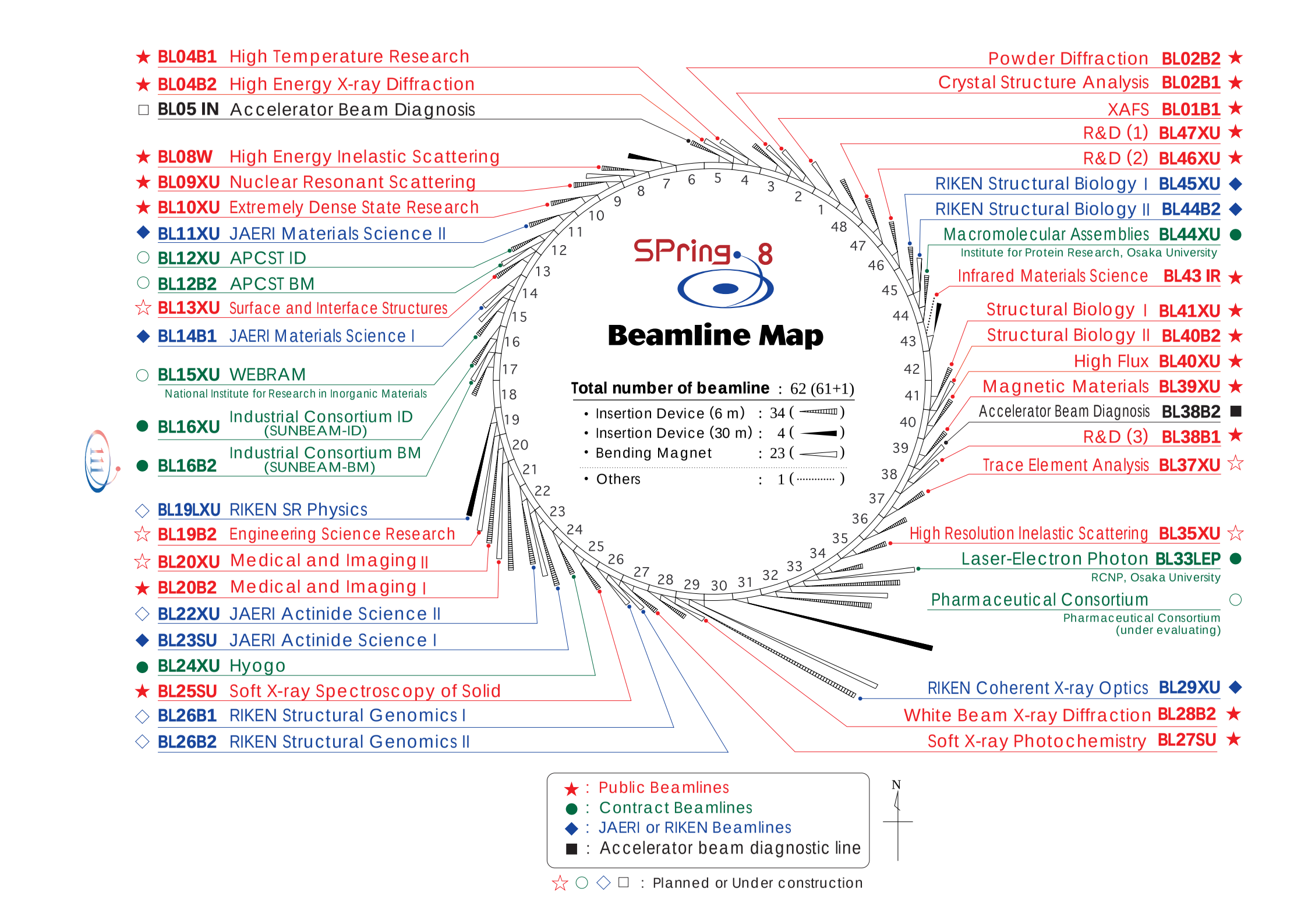
★ BL04B1 High Temperature Research
★ BL04B2 High Energy X-ray Diffraction
□ BL05 IN Accelerator Beam Diagnosis
★ BL08W High Energy Inelastic Scattering
★ BL09XU Nuclear Resonant Scattering
★ BL10XU Extremely Dense State Research
◆ BL11XU JAERI Materials Science II
○ BL12XU APCST ID
○ BL12B2 APCST BM
☆ BL13XU Surface and Interface Structures
◆ BL14B1 JAERI Materials Science I
○ BL15XU WEBRAM
National Institute for Research in Inorganic Materials
● BL16XU Industrial Consortium ID (SUNBEAM-ID)
● BL16B2 Industrial Consortium BM (SUNBEAM-BM)
◇ BL19LXU RIKEN SR Physics
☆ BL19B2 Engineering Science Research
☆ BL20XU Medical and Imaging II
★ BL20B2 Medical and Imaging I
◇ BL22XU JAERI Actinide Science II
◆ BL23SU JAERI Actinide Science I
● BL24XU Hyogo
★ BL25SU Soft X-ray Spectroscopy of Solid
◇ BL26B1 RIKEN Structural Genomics I
◇ BL26B2 RIKEN Structural Genomics II
Powder Diffraction BL02B2 ★
Crystal Structure Analysis BL02B1 ★
XAFS BL01B1 ★
R&D (1) BL47XU ★
R&D (2) BL46XU ★
RIKEN Structural Biology I BL45XU ◆
RIKEN Structural Biology II BL44B2 ◆
Macromolecular Assemblies BL44XU ●
Institute for Protein Research, Osaka University
Infrared Materials Science BL43 IR ★
Structural Biology I BL41XU ★
Structural Biology II BL40B2 ★
High Flux BL40XU ★
Magnetic Materials BL39XU ★
Accelerator Beam Diagnosis BL38B2 ■
R&D (3) BL38B1 ★
Trace Element Analysis BL37XU ☆
High Resolution Inelastic Scattering BL35XU ☆
Laser-Electron Photon BL33LEP ●
RCNP, Osaka University
Pharmaceutical Consortium ○
Pharmaceutical Consortium (under evaluating)
RIKEN Coherent X-ray Optics BL29XU ◆
White Beam X-ray Diffraction BL28B2 ★
Soft X-ray Photochemistry BL27SU ★
SPring-8
Beamline Map
Total number of beamline : 62 (61+1)
• Insertion Device (6 m) : 34
• Insertion Device (30 m) : 4
• Bending Magnet : 23
• Others : 1
★ : Public Beamlines
● : Contract Beamlines
◆ : JAERI or RIKEN Beamlines
■ : Accelerator beam diagnostic line
☆ ○ ◇ □ : Planned or Under construction
N

SPring-8

Japan Synchrotron Radiation Research Institute

Kouto 1-1-1, Mikazuki, Sayo
Hyogo 679-5198
JAPAN